



Influences of Forward and Backward Facing Steps in the Contour of a Turbine

Master thesis

Submitted at the Faculty of Mechanical Engineering at Graz University of Technology

by

Maximilian Comploj, BSc

Graz, September 2019

Head of Institute of Thermal Turbomachinery and Machine Dynamics:

Univ.-Prof. Dipl.-Ing. Dr.-Ing. Franz Heitmeir

Advisor and Supervisor:

Ao.Univ.-Prof Dipl.-Ing. Dr. techn. Wolfgang Sanz

Eidesstattliche Erklärung

Ich erkläre an Eides statt, dass ich die vorliegende Arbeit selbstständig verfasst, andere als die angegebenen Quellen/Hilfsmittel nicht benutzt, und die den benutzten Quellen wörtlich und inhaltlich entnommenen Stellen als solche kenntlich gemacht habe. Das in TUGRAZonline hochgeladene Textdokument ist mit der vorliegenden Masterarbeit identisch.

Statutory Declaration

I declare that I have authored this thesis independently, that I have not used other than the declared sources/resources, and that I have explicitly marked all material which has been quoted either literally or by content from the used sources. The text document uploaded to TUGRAZonline is identical to the master's thesis submitted.

Datum/Date

Unterschrift/Signature

Preface and acknowledgements

I would like to take this opportunity to express my gratitude to Ao.Univ.-Prof. Dipl.-Ing. Dr. techn. Wolfgang Sanz for giving me this chance to execute a real simulation and for the guidance I received throughout this journey.

I would also like to show my appreciation to the entire team of Institute of Thermal Turbomachinery and Machine Dynamics (ITTM) for the support and advices received.

I would like to acknowledge the use of HPC resources provided by the ZID of Graz University of Technology.

Lastly, I would like to thank my family and friends who stood at my side this entire time. Especially to my “partner in crime”, I would not be able to accomplish this today without you.

Abstract

Flow path imperfections in aeroengines at the contours can occur during engine-relevant conditions where engine parts heat up unequally especially during run up. A holistic investigation of the so-called reality effects was previously carried out by shifting a section of a test rig laterally causing steps in the inner and outer casing. 5-hole probe measurements were taken over an angular sector and Fast-Response-Air-Probes measurements were made over 360 degrees. It was discovered that the steps and therefore a restriction of the flow path caused a change in yaw angles which affected the incidence on blade rows downstream. This had a negative effect on the total efficiency. In order to better understand the effect of steps in the casing, in this work several numerical simulations, with different heights of contour steps were carried out. This work concluded that the yaw angles indeed changed after a step in the flow path and that they could be partly responsible for further losses downstream due to improper incidence angles on blade rows downstream.

Kurzfassung

Während des Betriebs von Triebwerken kann es zu Versetzungen im Gehäuse kommen, die meistens durch Aufwärm- und Abkühlvorgänge verursacht werden. Leichte Unsymmetrien im Gehäuse können bei Temperaturveränderungen Stufen und Übergänge in den inneren und äußeren Gehäusewänden auftreten. In vorangegangenen Experimenten wurde ein quasi ähnlicher Zustand erreicht, indem eine Kanalsektion seitlich verschoben worden ist. Es wurden 5-Lochsondenmessungen über einen Sektor und Fast-Response-Air-Probes Messungen auf 360 Grad vorgenommen. Es hat sich herausgestellt, dass durch die Kanalquerschnittsveränderung die Umfangswinkel der Strömung verändert haben. Durch diese veränderten Winkel ändert sich womöglich die Anströmung der darauffolgenden Schaufelreihen. Dies wurde auch in der Dissertation von S. Bauinger angeführt. Dies führt zu verminderten Effizienzen. Um die Einflüsse von Stufen im Gehäuse besser zu verstehen, wurde in dieser Arbeit versucht, mit numerischer Strömungssimulation das experimentelle Setup mit verschiedenen Stufenhöhen zu Rekonstruieren. Es stellte sich heraus, dass es tatsächlich zu veränderten Umfangswinkeln kommt und dies die Anströmung auf darauffolgende Schaufelreihen zum Teil verändert hat.

Contents

Preface and acknowledgements	II
Abstract	III
Kurzfassung	IV
Contents	V
1. Introduction	1
2. Basics of Fluid Dynamics	2
2.1 Navier-Stokes Equations	2
2.1.1 Continuity equation:	2
2.1.2 Momentum equation:	2
2.1.3 Energy equation:	3
2.1.4 Partial differential equation	3
3. Turbulent flows and ways to address turbulent problems	5
3.1 Direct numerical solution (DNS)	5
3.2 Reynolds Averaged Navier Stokes Equations (RANS)	5
3.3 Turbulence modelling	6
4. Basics of grids for CFD	9
4.1 Types of grids	9
4.1.1 Structured grids	9
4.1.2 Body fitted structured grids	10
4.1.3 Unstructured grids	11
4.2 Quality indicators for grids	11
5. Secondary flows in rotor	13
5.1 Secondary flows in the hub region	13
5.2 Tip leakage flows	16
6. State of the art research on flows over steps	17
6.1 Forward facing step	17
6.2 Backward facing step	18
7. Experimental investigation	19
7.1 Test Facility	19
7.1.1 Compressor setup	19
7.1.2 Transonic Test Turbine Facility (TTTF)	20
7.2 Different setups	21
7.2.1 Basic setup	21

7.2.2	<i>Shifted setup</i>	21
7.3	Measurement planes	23
8.	Simulation Setup	24
8.1	AiGrid	24
8.2	AiGridLinars	25
8.3	Linars	25
8.4	Convergence evaluation	33
8.5	Computational hardware infrastructure	34
8.6	Geometry	35
8.7	Boundary conditions	37
8.8	Evaluation planes	37
9.	Results	40
9.1	Approach	40
9.2	Influence of step on total pressure and isentropic efficiency	41
9.3	Evaluation of Plane C	45
9.3.1	<i>Comparison of the maximum step heights with the measurement data in Plane C</i>	45
9.3.2	<i>Comparison of the backward-facing step simulations in Plane C</i>	48
9.3.3	<i>Comparison of the forward-facing step simulations in plane C</i>	50
9.4	Evaluation of plane E	52
9.4.1	<i>Comparison of the maximum step heights with the measurement data in Plane E</i>	52
9.4.2	<i>Comparison of the backward-facing step simulations in Plane E</i>	55
9.4.3	<i>Comparison of the forward-facing step simulations in plane E</i>	57
9.5	Separation zones	59
9.5.1	<i>Shape and secondary vortices</i>	59
9.5.2	<i>Length of separation zone</i>	60
9.5.3	<i>Axial contour plots of separation bubble</i>	65
9.6	Further examination of plane C	70
9.7	Further examinations	74
10.	Conclusions	76
11.	Appendix	77
11.1	Prospect	77
11.2	Abbreviations and acronyms	79
11.3	Nomenclature	80
11.4	List of figures	81
11.5	List of tables	82
11.6	Figures	83

1. Introduction

Gas turbines have established themselves in certain applications due to their unique characteristics. They can be found in power plants generating electricity and on airplanes or helicopters creating thrust needed for flying. They distinguish themselves from other combustion engines by their high reliability and their astonishing power to weight ratio, which makes them indispensable to aero applications and as a stationary power source with high yield and long maintenance intervals.

Gas turbines consist of several expansion stages – each stage is made up by a stator which is succeeded by a rotor. Rotors and stators are basically blade rows which are oriented in opposite directions and the rotor allows the energy to be extracted from the gas.

Multistage turbines are made of segments of various lengths separated along their longitudinal axes. Each segment has its own geometry, weight and size, resulting in different responsiveness to temperature changes, which as a consequence implies relative changes in size between the different components during in-stationary operation. This mainly manifests itself between the relatively heavy blades and the thin casing resulting in different tip clearances, which heavily affects efficiency. Therefore engine manufacturers implement active tip leakage control for aeronautical turbines. A difference in temperature for the subsequent segments can result in a difference in casing diameter even during steady operation.

This thesis will focus on disturbances created by the different potential thermal expansions of the casing resulting in a step within the flow path, which can be a forward-facing step (FFD), or a backward-facing step (BFS).

2. Basics of Fluid Dynamics

Fluid dynamics describes the movement of liquid or gaseous fluids. It is based on the conservation laws, which are made up by the continuity equation, momentum equation, and energy equation. They are basis for the Navier Stokes Equations. The most important quantities in these equations are ρ which represents density, \vec{v} represents the absolute velocity, p static pressure, T temperature and e total internal energy. This chapter is based on [1]

2.1 Navier-Stokes Equations

2.1.1 Continuity equation:

$$\frac{\partial \rho}{\partial t} + \nabla \cdot (\rho \vec{v}) = 0 \quad (2-1)$$

In this equation, the first term $(\frac{\partial \rho}{\partial t})$ represents the temporal change of density in the control volume, whereas the second term $(\nabla \cdot (\rho \vec{v}))$ represents the density change due to mass flux across the volume surfaces.

2.1.2 Momentum equation:

$$\frac{\partial(\rho \vec{v})}{\partial t} + \nabla \cdot (\vec{v} \vec{v} \rho) + \nabla p = \rho \vec{f} + \nabla \cdot \tau \quad (2-2)$$

In the momentum equation, the first term $(\frac{\partial(\rho \vec{v})}{\partial t})$ represents the temporal change of momentum, the second term $(\nabla \cdot (\vec{v} \vec{v} \rho))$ represents the momentum flux over the boundaries and the third term (∇p) represents the surface forces known as pressure force. The first term on the right side $(\rho \vec{f})$ represents the body forces of which the most important one is gravity. This term is negligible for thermal turbo-machines due to the low density of the air. The second term $(\nabla \cdot \tau)$ represents the viscous normal and shear stresses.

2.1.3 Energy equation:

$$\frac{\partial e}{\partial t} + \nabla[\vec{v}(e + p)] = \frac{\partial Q}{\partial t} + \rho \vec{f} \cdot \vec{v} - \nabla \cdot \vec{q} + \nabla \cdot (\boldsymbol{\tau} \cdot \vec{v}) \quad (2-3)$$

The first term ($\frac{\partial e}{\partial t}$) of the energy equation represents the temporal change of energy in the control volume, the second term ($\nabla[\vec{v}(e + p)]$) is the energy flux over the control volume boundaries and the power of pressure forces. The first term on the right-hand side ($\frac{\partial Q}{\partial t}$) represents the influence of heat sources, the second term ($\rho \vec{f} \cdot \vec{v}$) represents the influence of body forces on the power balance. Both terms can be neglected in turbomachinery flows. The third term ($\nabla \cdot \vec{q}$) describes the energy exchange by heat conduction. Heat conduction in its differential form of Fourier's law can be seen in equation (2-4). q is the local heat flux density; k the material's heat conductivity and ∇T is the temperature gradient. The heat conductivity seen in equation (2-5) is in direct relation to the dynamic viscosity and the specific heat capacity coefficient. And indirect to the Prandtl number which is mostly constant for most gases with a value of 0.72. The last term ($\nabla \cdot (\boldsymbol{\tau} \cdot \vec{v})$) is the dissipation function and describes the power required for the deformation of a fluid particle due to the viscous forces.

$$\boldsymbol{q} = -k \nabla T \quad (2-4)$$

$$k = \frac{c_p}{Pr} \mu \quad (2-5)$$

2.1.4 Partial differential equation

The partial differential equation system consists of three differential equations for the five unknowns ρ , v , T , e and p . This system can be closed with two additional equations: equation (2-6) and equation (2-7) can be obtained by the thermodynamic equation of state of an ideal gas with constant specific heats, characterized by the gas constant R and the ratio of specific heats γ .

$$e = \frac{p}{\kappa - 1} + \rho \frac{\bar{v}^2}{2} \quad (2-6)$$

$$T = \frac{(\kappa - 1)}{R} \left(\frac{e}{\rho} - \frac{\bar{v}^2}{2} \right) \quad (2-7)$$

For turbulent flows the computational costs are very high in order to resolve all turbulent fluctuations in time and space. Therefore, turbulence modelling is often introduced based on the time-averaged Navier-Stokes equations (RANS).

3. Turbulent flows and ways to address turbulent problems

This chapter explains how turbulent flows are addressed in computational simulations. This chapter was written with the help of following sources: [1] [2] [3]

3.1 Direct numerical solution (DNS)

If the entire domain is computed with the Navier Stokes equations entirely, it is called direct numerical solution. This is the simplest approach from a conceptual point of view, but this method is far from feasible since the computational power needed is excessively high. Furthermore, it must be kept in mind that even the DNS is just an approximation of the real flow. It is necessary for the computational domain to be of the same size or bigger than the largest turbulent eddy. In order to effectively make use of DNS, a fine grid is necessary. This implies a very small time-step to comply with the Courant Friedrich Lewy (CFL) condition, which leads to huge computational power requirement. In order to deal with this issue, in industrial applications RANS is used.

3.2 Reynolds Averaged Navier Stokes Equations (RANS)

The RANS equations avoid the huge computational requirements of DNS by averaging the fluctuations and splitting the flow quantities into a time-mean value a fluctuation term as seen in equation (3-1).

$$\phi(x_i, t) = \bar{\phi}(x_i) + \phi'(x_i, t) \tag{3-1}$$

Where

$$\bar{\phi}(x_i) = \lim_{T \rightarrow \infty} \frac{1}{T} \int_0^T \phi(x_i, t) dt \tag{3-2}$$

T is the averaging interval and t is the time. The interval must be larger than the fluctuation time scale and if the time interval goes towards infinity, $\bar{\phi}$ does not depend on the averaging interval. If the flow is unsteady, ensemble averaging must be used instead of time averaging. There are

two basic methods of averaging: the first one is the direct average called RANS, and the second is weighting the values with the density. This 2nd method leads to the Favre Averaged-Navier-Stokes-Equations and is used for compressible flows. Usually the thermal quantities and the velocities are mass-weighted averaged, and the other quantities are RANS averaged.

3.3 Turbulence modelling

A flow is characterized by its Reynolds number which is the ratio between the inertia forces and the viscous forces. As Reynolds numbers increase, the flow becomes increasingly unstable and therefore more turbulent. These turbulent flows cannot be neglected as they have a major effect on heat dissipation and other phenomena. To effectively simulate turbulent flows, statistical models are being used in simulations - most of them based on the creation and dissipation of turbulent energy. This is a common practice even though it is known that the Navier-Stokes-Equations completely describe turbulent flow, and therefore DNS would solve the flow correctly. The computational power required would be unreasonably high for high Reynolds numbers. Grid density must be increased with increasing Reynolds number and the required time step decreases with the increasing grid density which leads to huge calculation times for high Reynolds number flows.

A way to go around this is by using empirical turbulence models. None of them have a general validity and each one has its strengths and weaknesses; most of them add an artificial viscosity to the RANS equations which considers the effect of the fluctuating component of the variables.

The first group are the eddy viscosity models. These models are based on the Boussineq approximation (see equation (3-3)). These different models vary in their way to define the turbulent viscosity.

$$\overline{-\rho u'_i v'_j} = \mu_t \left(\frac{\partial \bar{u}_i}{\partial x_j} + \frac{\partial \bar{u}_j}{\partial x_i} \right) - \frac{2}{3} \rho \delta_{ij} k \quad (3-3)$$

k is the turbulent kinetic energy defined by:

$$k = \frac{1}{2} \overline{u'_i u'_i} = \frac{1}{2} (\overline{u'_x u'_x} + \overline{u'_y u'_y} + \overline{u'_z u'_z}) \quad (3-4)$$

Turbulent viscosity is often found with two parameters, a characteristic velocity and a measure for the turbulent length scale L . The characteristic velocity can be obtained from the mean velocity field, but the length scale can only be described for simple flows. These mixing length models are also called zero equation models or algebraic models and they can only be used for simple flows attached to surfaces. These models fail for flows with high curvature or free stream turbulence.

One-equation models improve accuracy by considering the transport effects by adding one further differential equation. A popular one-equation model is by Spalart and Allmaras.

Two-equation models have in addition to a transport equation for the turbulent kinetic energy a further differential equation for a quantity representing the dissipation process. The two most common models are the k - ε and the k - ω models. The k - ε is the most popular one. The eddy viscosity for the k - ε model is defined with k and the turbulent dissipation ε as in (3-5).

$$\mu_t = \frac{k^2}{\varepsilon} \rho C_\mu \quad (3-5)$$

The k - ω turbulence model is more suited for flows in near-wall regions. It should be noted that the k - ω model is prone to over-predict shear stresses and therefore reach separation earlier than other models. The model variable ω stands for specific dissipation and is needed for the calculation of the kinematic viscosity in Wilcox's k - ω -model (see (3-6))

$$\nu_t = \frac{k}{\omega} \quad (3-6)$$

To create a link between the k - ε and the k - ω model, the Shear Stress Transport model (SST) was introduced in 1994. It basically blends the k - ε and the k - ω turbulence models and tries to exploit the advantages of each model. It weights the dissipation and the specific dissipation depending on the cell distance to the wall. This further intensifies the need for computational capacity, but which is easily handled by today's computers.

For flows, which are highly anisotropic, the eddy viscosity models are not accurate, and Reynolds stress models should be used instead. Reynolds stress models try to solve the closure problem of turbulence modelling through transport equations for the individual turbulent stresses. Reynolds stresses which are reduced for flows around convex surfaces and are amplified for flows on concave surfaces influence significantly the dissipation and production of vortices with high isentropic behaviour. Reynolds stress models consist of additional 7 equations, leading to an increased CPU time of 50-60% compared to two-equation models.

Another bridge can be drawn by linking statistical models and the direct numerical simulation. This bridge is called Large Eddy Simulations (LES) in which the big eddies are solved directly, and a low pass filter is applied to the Navier-Stokes-equations in order to ignore the smallest length scales. Furthermore, the smaller eddies tend to have a more isentropic behaviour, therefore it is easier to model them accurately. This approach is still computationally expensive, but with increasing computational power this approach becomes more and more interesting.

4. Basics of grids for CFD

Setting up a proper grid is essential for a CFD simulation. A good grid setup takes a couple of days and a couple of iterative steps, but the user is rewarded with a simulation which will be more stable and converge faster. In this chapter different grid types will be compared with their advantages and downsides. The grid should be as coarse as possible and as fine as necessary in order to minimize needed resources. This chapter gives an insight into the different types of grids used for CFD. It explains weaknesses and strengths of each grid type. This chapter was written with the help of [4]

4.1 Types of grids

4.1.1 Structured grids

Structured grids operate on a more efficient level than unstructured grids in terms of memory requirements, accuracy and CPU time, but they cannot be generated easily by automated software and structured grids are difficult to adopt for complex geometries. Changing a point in the grid can forcefully affect the entire block. To ease this influence, multi block domains can be created. This can be further enhanced by allowing nonmatching lines at inter-block boundaries.

Cartesian grids

They represent the ideal option in terms of accuracy and should be applied whenever possible, mostly in regions free of objects or walls. This type of grid is especially used for simulations of sound propagation since higher order schemes can be applied. For straight surfaces they present a good solution but for curved surfaces the accuracy is worsened because the grid is cut, and the mesh density cannot be adopted close to walls.

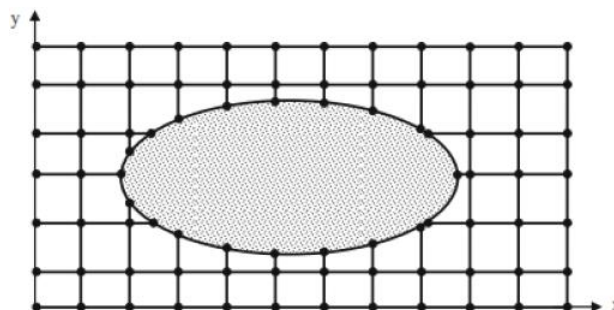


Figure 4.1: Cartesian grid around an elliptic object [5]

Non-uniform cartesian grids

Non-uniform Cartesian grids are composed of variable mesh sizes and can be of Quadtree-Octree grid type. Quadtree-Octree grids can be obtained by subdividing cells. They are called quadtree in the two-dimensional and Octree in the three-dimensional domain. This grid type is better for curved surfaces compared to Cartesian grids because walls can be approximated with a staircase shape or with so called cut-cells.

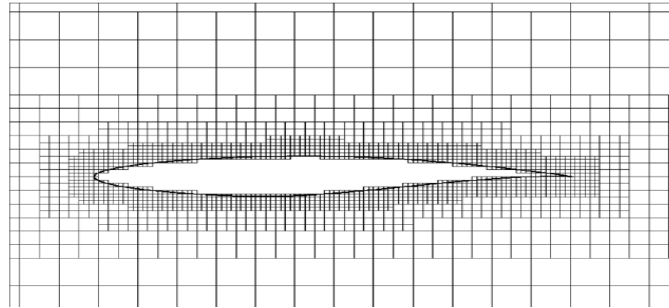


Figure 4.2: Quadtree Octree grid around an air foil [5]

4.1.2 Body fitted structured grids

This type of grid was used for this simulation and consists of different block types put together. Blocks can be of H/C/O/I-type. In Figure 4.3 the grid surrounding the stator for the simulation can be seen. The block boundaries are highlighted in pink and give information on the block type. The blade surface is surrounded by an O-type grid. All other blocks are of H type

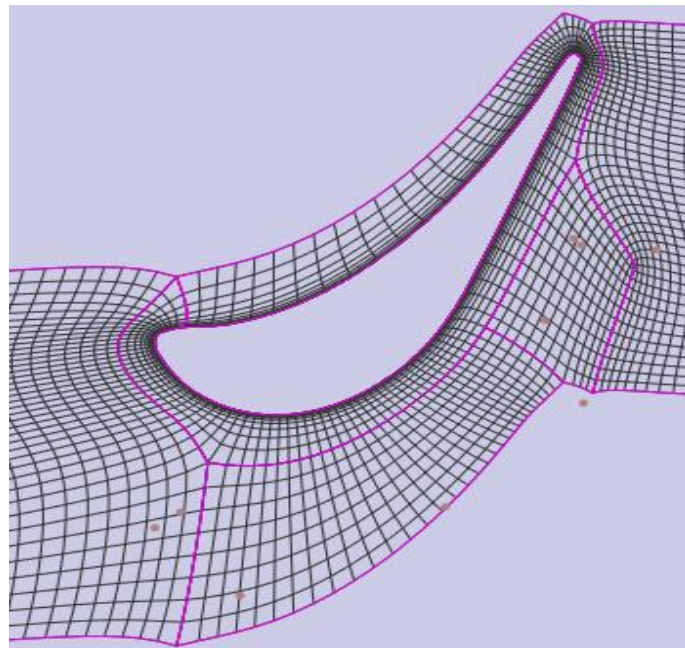


Figure 4.3: Body fitted grid around the first stator in the simulation

4.1.3 Unstructured grids

Unstructured grids have gained huge popularity recently due to automated grid generation in industrial applications. The major drawback from unstructured grids is their lower accuracy but they allow the user to refine certain regions without heavily affecting the region outside the refinement. Unstructured grids use Triangle/Tetrahedra cells, which are the most basic ones. Hybrid grids further consist of hexahedrons close to surfaces, which satisfy resolution requirements in the boundary layer of flows with high Reynolds numbers better than tetrahedrons. Tetrahedrons at boundary faces have high skewness and therefore are less suited. An unstructured grid can be seen in Figure 4.4.

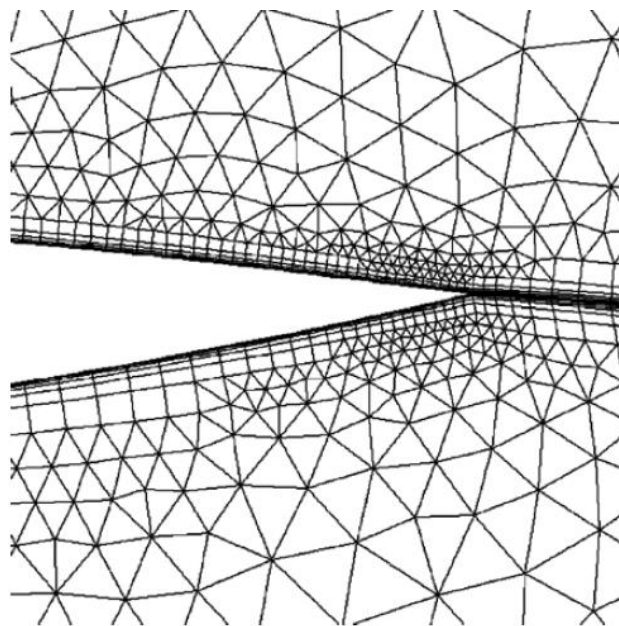


Figure 4.4: Unstructured Grid around an air foil [5]

4.2 Quality indicators for grids

The quality of grids can be evaluated using parameters analysed with post processing software like Tecplot.

One of the most important parameters is the volume ratio, which describes the volume ratio between two neighbouring cells, this value shouldn't exceed 3.

Another parameter is the aspect ratio (AR) which is essentially the ratio of the longest distance between a face point of a cell to the cells centre compared to the shortest distance from a face point of a cell to the cells centre. The aspect ratio of a grid should never exceed 35, but it is difficult to say what the optimal aspect ratio is since cells with large aspect ratios can yield

higher accuracy if the flow is highly directional dependent. Furthermore, high aspect ratios increase the interpolation error. Sudden change in aspect ratio should be avoided.

Skewness gives information on the magnitude of the distortion of a cell. A skewness of 0 indicates that a cell is perfectly orthogonal and doesn't contain any skewness. The worst cells shouldn't exceed a skewness of 0.85 and the average should be below 0.5. An average skewness below 0.5 is considered good. In Figure 4.5 a representation of ideal and non-ideal "skewed" cells can be seen.

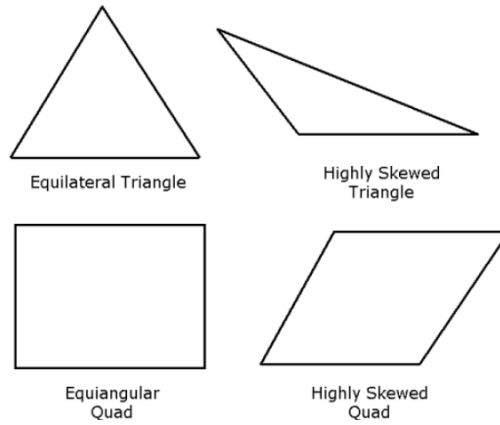


Figure 4.5: Representation of skewness factor [6]

Skewness is broken up in EquiAngle Skew (Q_{EAS}) and EquiSize Skew (Q_{EVS}). EquiAngle Skew is defined in equation (4-1).

$$Q_{EAS} = \max\left\{\frac{\Theta_{max} - \Theta_{eq}}{180 - \Theta_{eq}}, \frac{\Theta_{eq} - \Theta_{min}}{\Theta_{eq}}\right\} \quad (4-1)$$

Θ_{max} and Θ_{min} represent the maximum and the minimum angle of a cell. Θ_{eq} is the characteristic angle which is 90° for squares or rectangular cells. The last parameter which is going to be discussed in this thesis is the cell's refinement towards surfaces. This parameter can just be evaluated after a simulation has been carried out. This parameter is called y^+ and is defined by equation (4-2).

$$y^+ = \frac{u_\tau \cdot y}{\nu} \quad (4-2)$$

u_τ stands for friction velocity and is defined with $\sqrt{\frac{\tau_w}{\rho}}$, y is the absolute distance to the wall and ν is the kinematic viscosity. For optimal results, the parameter should be about 1.

5. Secondary flows in rotor

In this chapter secondary flows which generally occur in turbines are explained in order to provide knowledge for following chapters discussing the flow. This chapter was written according to [7]

5.1 Secondary flows in the hub region

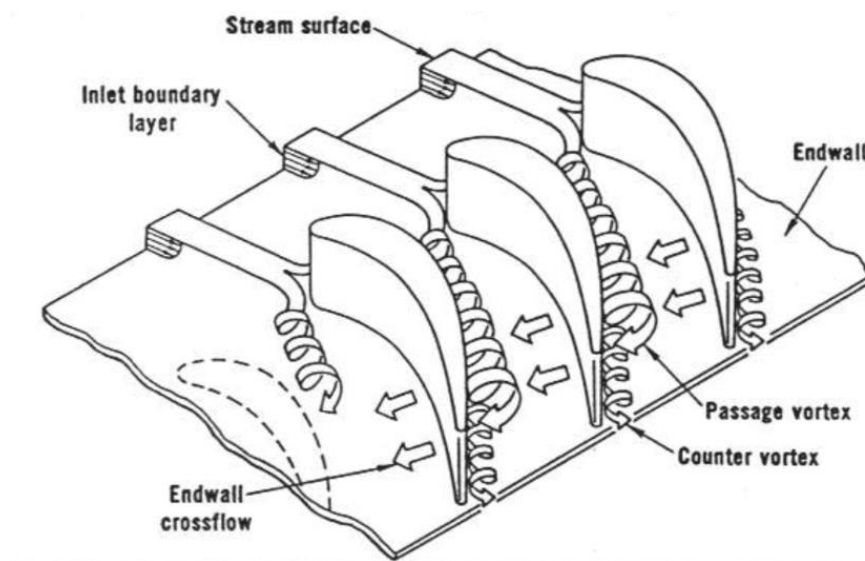


Figure 5.1: Simple model of secondary flows in blade row [7]

Secondary flows in turbine cascades have been studied for a long time and there are different perceptions of what occurs in a blade row. The effects can vary from blade row to blade row dependent on geometry and boundary conditions, but there are basic phenomena which can be found in almost all blade rows. Probably the most important one is the horseshoe vortex. Since the flow further away from the wall is faster than in the boundary layer there will be a pressure increase at the leading edge with increasing distance. This pressure increase will cause the flow to roll up and separate in two counter rotating vortices called leading edge horseshoe vortex which can be seen in Figure 5.1. The vortex following the pressure side of the blade will be drawn to the suction side and combines with the passage vortex. The other leg of the horseshoe vortex remains attached to the suction side and forms the counter vortex to the passage vortex. A different and a bit more complex version of end-wall secondary flows was proposed by Sharma and Butler [8]. This version includes that the counter vortex

will wrap itself around the bigger passage vortex and swirl around it while rotating in the opposite direction. An illustration of this can be seen in Figure 5.2.

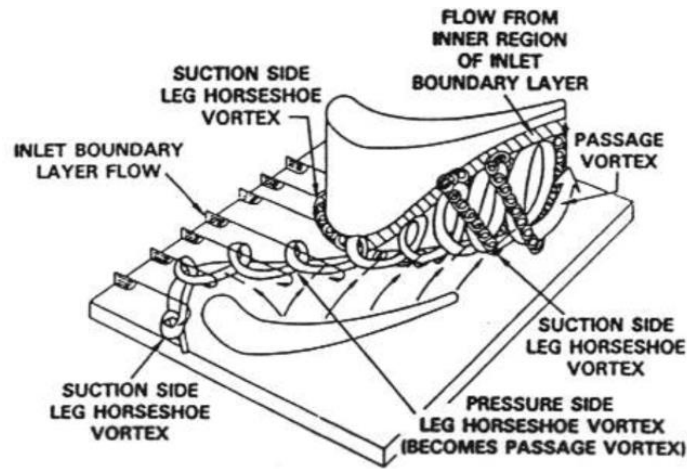


Figure 5.2: Secondary flows according to Sharma and Butler [8]

Another vortex pattern revision was proposed by Goldstein and Spores of the University of Minnesota [7]. They carried out experiments at low Reynolds number (for flow visualization with smoke) and used laser light. As shown in Figure 5.3 several new vortices were added to the model seen in Figure 5.1. Approximately at the same axial position at which the horse shoe vortex would reach the suction side, the counter vortex starts to wrap itself around the bigger passage vortex, and there are two other vortices created. One of them is the wall vortex which resides above the passage vortex and rotates in its opposite direction and is drawn towards the mid span of the blade. The other one is the suction side corner vortex which shares the same origin as the wall vortex but remains closer to the hub. Furthermore, a vortex will be generated at the pressure side which is called pressure side corner vortex. Cross sections of the vortices at different axial positions are visible in the top right corner of Figure 5.3. The presence of these smaller vortices is highly dependent on the corner radius and can vary significantly throughout different setups.

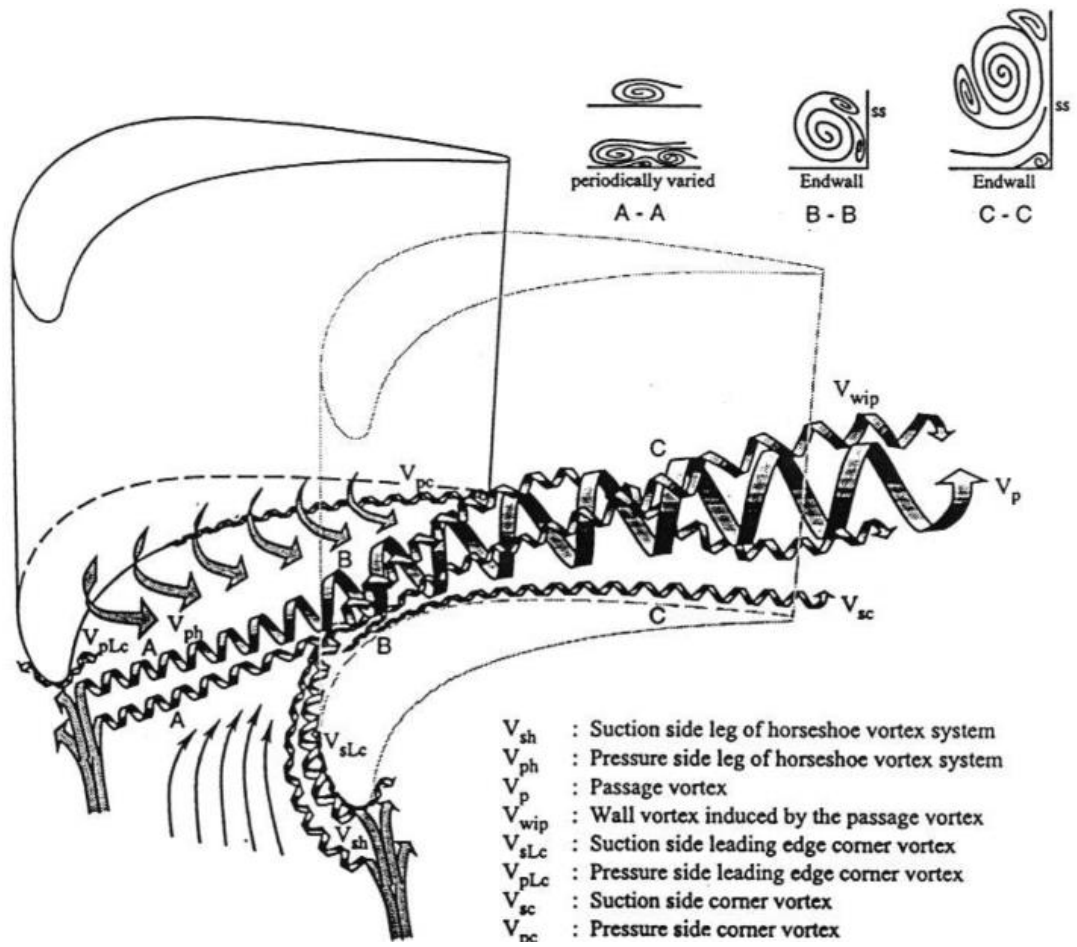


Figure 5.3: Secondary flows according to Olson, Goldstein and Eckert [7]

5.2 Tip leakage flows

Predominant secondary flows in the tip region of a rotor are shown in Figure 5.4. They are made up by the tip leakage vortex and the passage secondary vortex. The tip leakage vortex comes from the pressure side of the blade and is sucked, due to the decrease in pressure, towards the suction side of the blade where it starts swirling. The passage secondary vortex enhanced by the relative motion between the casing and the rotor and the pressure difference is drawn to the tip leakage vortex and rotates in opposite direction to the tip leakage vortex. Secondary flows in the rotor are mostly driven by pressure forces and less by viscous forces. The losses caused by tip leakage are substantial in turbomachinery and therefore the tip clearance is kept as small as possible.

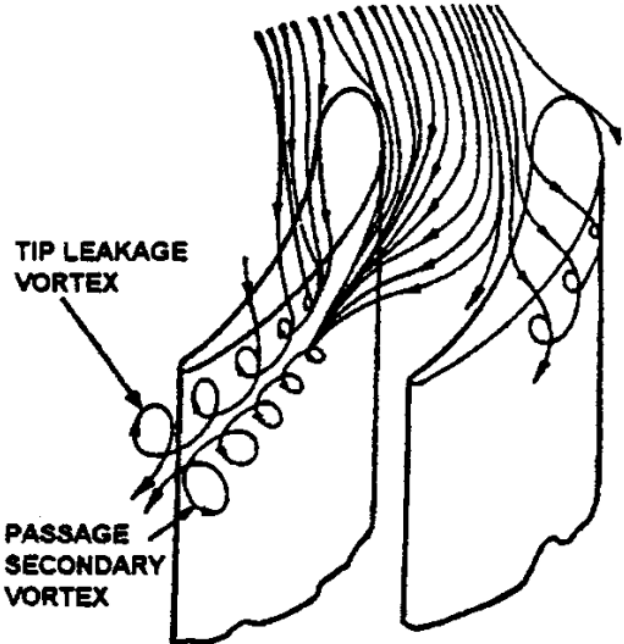


Figure 5.4: Secondary flows at rotor tip [9]

6. State of the art research on flows over steps

This chapter will discuss experiment data regarding forward and backward-facing steps. It will focus on characteristic lengths and determining factors.

6.1 Forward facing step

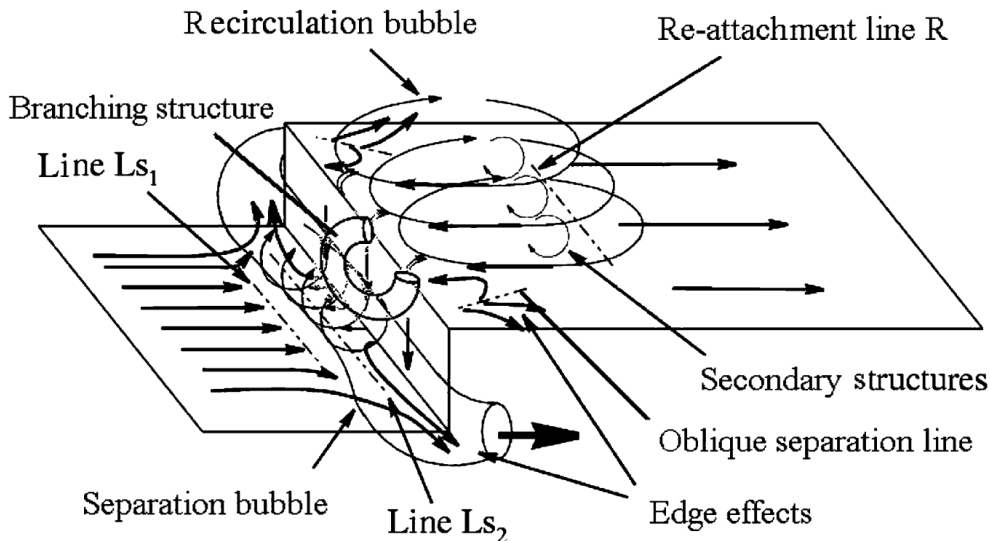


Figure 6.1: Flow phenomena at forward-facing step [10]

The flow around a forward-facing step has already been studied by Largeau and Moriniere [10]. Experiments were conducted on forward-facing steps of heights of 30, 40 and 50 mm and with speeds of 15-40 m/s. The ratio of length of reattachment to step height was around 4 for the highest speeds. As for the separation zone in front of the step the centre of the vortex is placed at around 0.5 step height in front of the step according to [11]. It was also stated that at higher Reynolds numbers the dimensionless separation length becomes a constant, and that the most important parameter determining the flow characteristic is the ratio between boundary layer thickness to step height. This parameter seems not to be of such a big influence for the backward facing step. A scheme of the flow in the vicinity of a forward-facing step according to Largeau and Moriniere can be seen in Figure 6.1.

6.2 Backward facing step

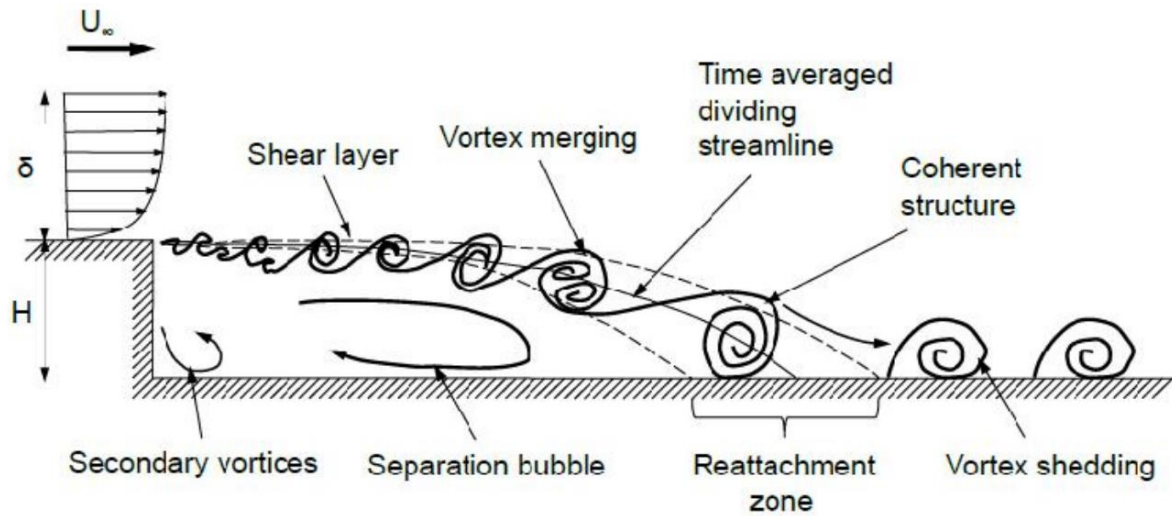


Figure 6.2: Flow at backward-facing step [12]

Steven Darmawan analysed different experiments which were carried out on backward facing steps [12]. These experiments were done with larger step heights, ranging from 10 mm to 40 mm, and higher expansion ratios, defined by cross area after the step divided by the cross area before the step, than in the simulation which was carried out in this thesis. Darmawan states that with an increase in expansion ratio the reattachment length will also increase. Previous simulations on backward facing steps concluded that the dimensionless reattachment length (ratio of reattachment length to step height) is about 6 for a $k-\epsilon$ model for an expansion ratio of 3; with an RNG $k-\epsilon$ turbulence model a reattachment length of 4 was achieved. Experiments resulted in a reattachment length of 7. Lin Chen [13] also summarized in his article several simulations of backward facing steps. It was stated that the flow behind a backward facing step will become three dimensional when the Reynolds number exceeds 100 but this value is lower in experiments due to low-amplitude disturbances in real experiments. When Reynolds numbers exceed 20,000, the reattachment length is not affected anymore by Reynolds number and expansion ratio. For these Reynolds numbers above 20,000 the dimensionless reattachment length converges to around 6. Driver & Seegmiller (1984) [14] had a similar setup with a diverging channel, fairly high Reynolds number of 37,000 and a low expansion ratio of 1.11 and their reattachment length was 6.2. A scheme of secondary flows near a backward facing step can be seen in Figure 6.2.

7. Experimental investigation

7.1 Test Facility

7.1.1 Compressor setup

The Transonic Test Turbine Facility (TTTF) was first put into operation up in November 1999 at the Institute for Thermal Turbomachinery and Machine Dynamics at Graz University of Technology. The facility is fed by a compressor station, which consists of two centrifugal, and two screw compressors located within the same housing. These three compressors, powered by three-phase asynchronous motors, can operate in parallel or in serial mode, which results in twelve different configurations having their own pressure ratios and mass flows. The combined maximum theoretical power of this station is 3 MW. In order to enhance efficiency and operate at higher mass flows the test turbine drives a brake compressor which feeds additional air to the turbine. The two flows are merged in the mixing chamber which is visible in Figure 7.1. The feed and exhaust scheme can be seen in Figure 7.2. Due to the high-power demand and the more constant air conditions during night hours the test runs are mostly carried out during the night. Another reason to operate at night is the lower air temperature which allows for a more stable operation and a better cooling efficiency, especially in summer.

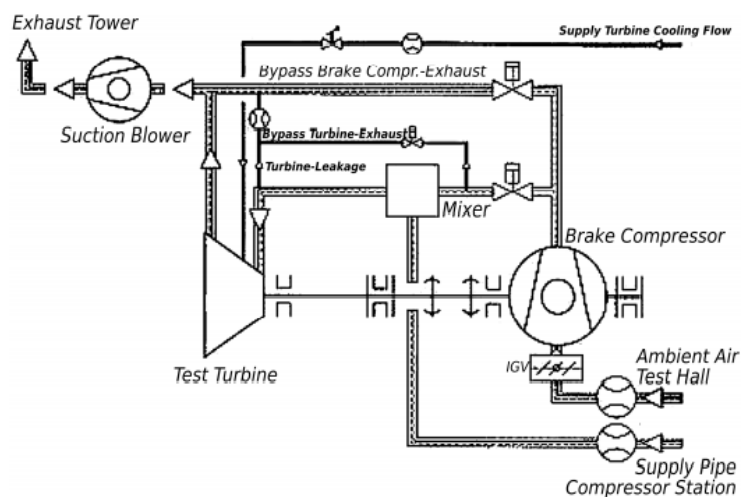


Figure 7.1: Compressor Setup [15]

7.1.2 Transonic Test Turbine Facility (TTTF)

The Transonic Test Turbine Facility at the Institute for Thermal Turbomachinery and Machine Dynamics at Graz University of Technology consists of two stages: a high-pressure and a low-pressure stage. Each Stage is mounted on its separate shaft. The low-pressure stage is axially and radially movable. The Turning Mid Turbine Frame or TMTF connects the two stages. The Turning Mid Turbine Frame is a S-shaped transition duct whose goal is to guide the flow to the LP stage of higher diameter. Without a transition duct to higher diameters the low-pressure turbine would have to run faster for a similar enthalpy drop, which is not possible by the speed limits of the fan driven by the LP turbine. Usually the duct is equipped with struts. These are necessary for the casing structural support and they provide the necessary space for oil pipes in order to lubricate the bearings. The intention of the Turning Mid Turbine Frame is to eliminate the need for the LP stator behind the strut, so that, the entire engine is shorter and therefore lighter. Due to the highly varying yaw angles before the Turning Mid Turbine Frame the blades of the MTF have a carefully designed 3D geometry to avoid wrong incidence angles and strong secondary flows or separation. A scheme of the TTTF can be seen in Figure 7.2.

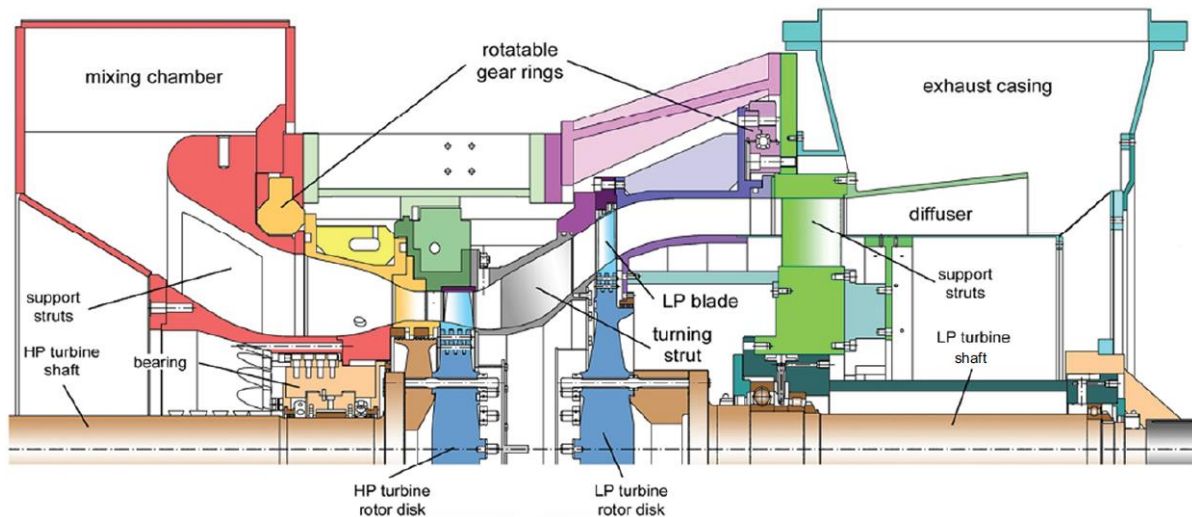


Figure 7.2: Axial cross section of test rig [16]

7.2 Different setups

7.2.1 Basic setup

The basic setup consists of 24 stator blades, 36 rotor blades, a TMTF with 16 turning struts and a LP rotor with 76 blades. The HP rotor had a tip gap of approx. 1,8% blade height resulting in a top clearance of 1,3 mm. The most important design parameters are given in Table 7.1 Test rig blade parameters. Effort was put in a proper setup with no imperfections in the contour.

	HP van	HP blade	TMTF	LP blade
Blade no	24	36	16	76
Thickn./chord ratio	0.31	0.19	0.24	0.12
Aspect ratio H/c_{ax}	1.15	1.37	0.46	2.94
Re number ($*10^{-6}$)	2.38	1.1	1.86	0.46

Table 7.1 Test rig blade parameters [16]

7.2.2 Shifted setup

A scheme of the lateral shift can be seen in Figure 7.3 where the back end of the test rig was shifted laterally to the left about 2.5% channel height in plane C between HP rotor and TMTF creating a step of 1.3 mm at both extremes. The shift was achieved with thermoelastic centring devices. With this setup a forward-facing step was created at the right channel side at the hub when looking in the flow direction and a backward facing step at the left side also at the hub. At the outer casing it is the opposite.

The 5-hole probe measurements were taken in the first quadrant of Figure 7.3 and therefor the results at the hub are best comparable with a medium to small backward facing step.

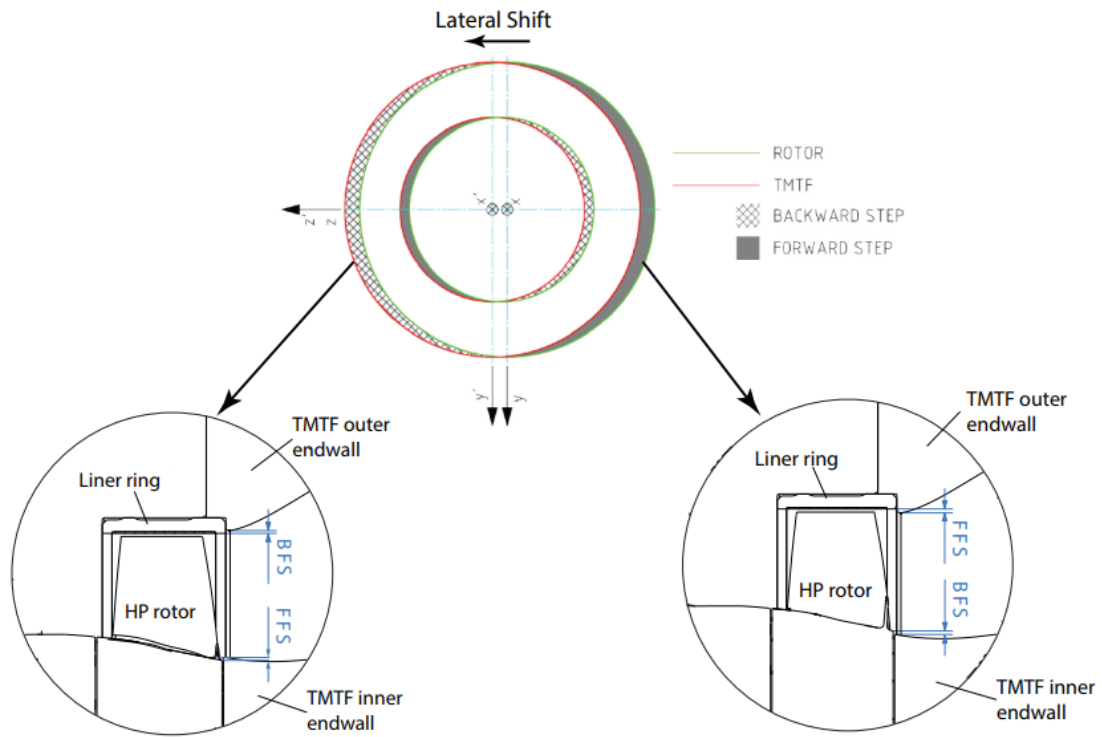


Figure 7.3: Scheme of lateral shift [16]

7.3 Measurement planes

In Figure 7.4 a cross section of the Transonic Test Turbine Facility with all the measurement planes can be seen. In plane A (inlet) mainly rakes were installed to measure total pressures and total temperatures. All planes visible in Figure 7.4 are 360 degree traversable. For planes E and F this is possible due to a traversable outer casing. Rake traverses were performed for 360 degrees and 5-hole probes over an angular sector.

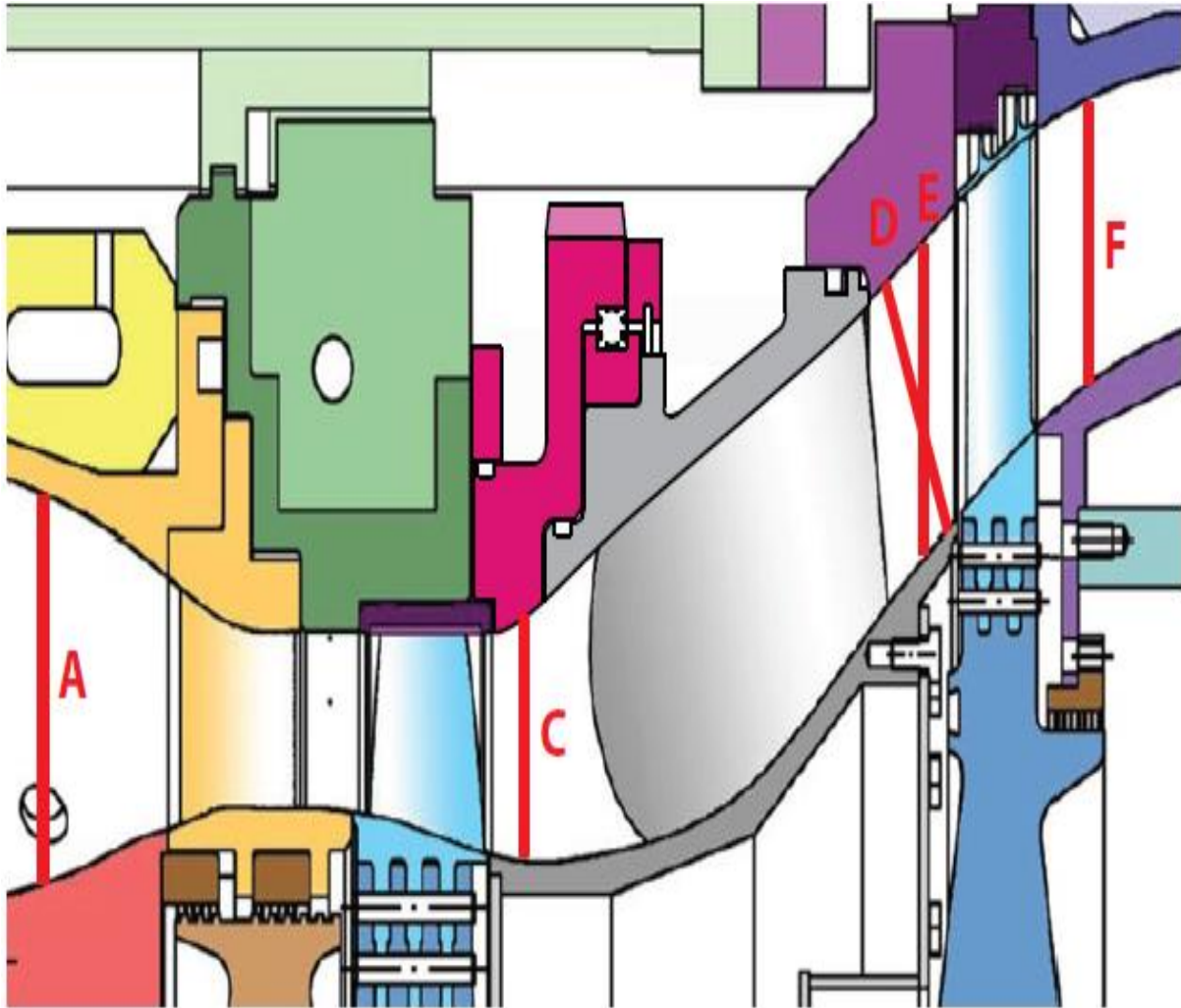


Figure 7.4: Axial cross section of measurement planes [16]

8. Simulation Setup

8.1 AiGrid

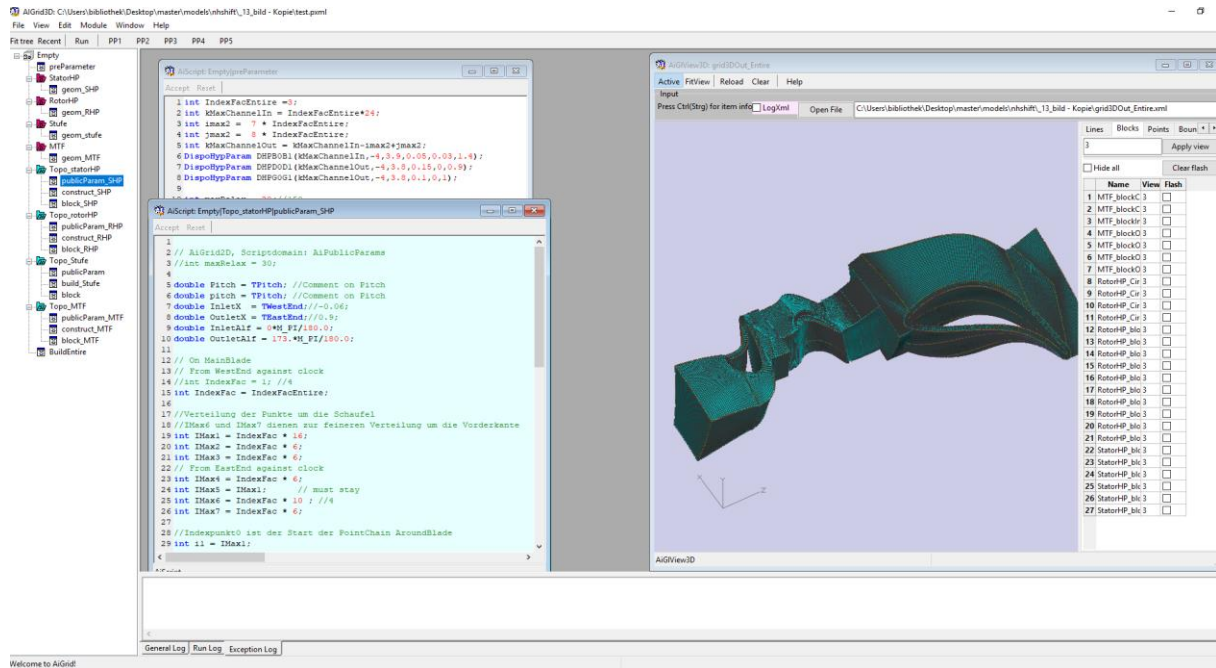


Figure 8.1: AiGrids GUI

For this simulation the mesh was created with an in-house program called AiGrid by Pieringer. It basically requires the hub and shroud contours from each domain with several sections of the blades in xml format. It then creates with a couple of scripts a body fitted structured grid which can easily be adjusted in resolution. It also has the capability to give the user insight in the grid he just created with a user-friendly GUI which can be seen in Figure 8.1. Output files, which will be required later on, are the geometry files geom.bin or geom.txt (upon user setting) and the faces.xml file which contains all block boundaries and interfaces between the blocks.

8.2 AiGridLinars

Faces.xml is further required for AiGridLinars which provides an excellent GUI. AiGridLinars allows the user to bundle faces, which are listed in the faces.xml file, and apply boundary conditions to these faces as shown in Figure 8.2

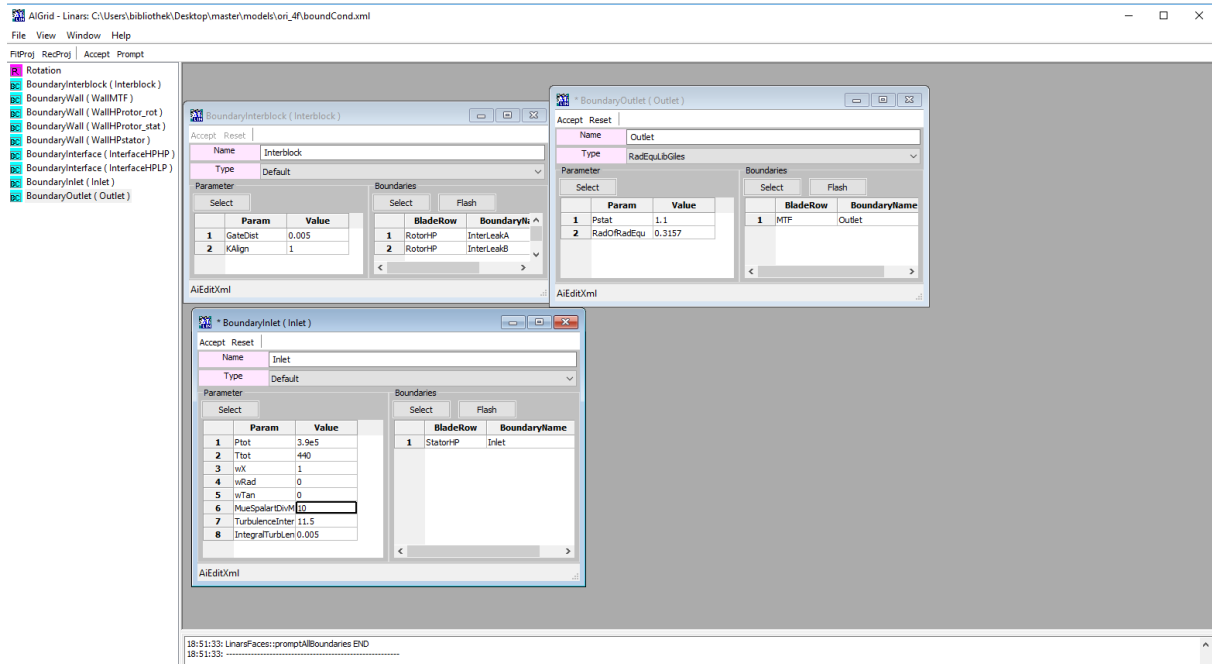


Figure 8.2: AiGridLinars

This program simplifies the assignment of boundary conditions for stationary simulations. For transient simulations with a lot of repetitive boundaries a script in Python was created which multiplies the faces to facilitate an otherwise repetitive work. It is also possible to view the selected faces to ensure the work is done properly. AiGridLinars creates a file called bound-Cond.xml containing all the information regarding the boundaries. This file will be used by the solver Linars.

8.3 Linars

With the output files from AiGrid and AiGridLinars the simulation can be performed. Further the Control.xml file is needed, which basically contains the solver settings, as the turbulence model applied, how many iterative steps should be made or what output files should be generated. The most important output files are the Tecplot files and the boundary files. A deeper explanation on the possible settings is visible in Table 8.1

General	Description	Chosen parameters
kap Double	Isentropic coefficient	1.4
Time interations Int	Time iterations	Couple of thousands
UnsteadyCalc Int	0: steady 1: transient	0
RelaxMethod Int	0: implicit ADI 1: first order Runge-Kutta 2: fourth order Runge-Kutta	0
ConstTimeStep Int	Time step for transient simulations approx. $1/10^\circ$ rotation	0
CflOnCoarse Double	CFL number for coarser grid (depends on grid quality)	40
CflOnFinest Double	CFL number for finest grid (depends on grid quality)	60
TVDOnCoarser Int	0: first order 1: minmod limiter 2: von Albada limiter 3: Quick scheme 4: Central first order 5: Central second order	Starting with 0 subsequently with 1
TVDOnFinest Int	0: first order 1: minmod limiter 2: von Albada limiter 3: Quick scheme 4: Central first order 5: Central second order	Starting with 0 subsequently with 1
ComprForm Int	0: compressible code 1: incompressible code with pseudo compressibility	0
FreezeMainVa Int	0: main variables not frozen 1: main variables frozen	0 only if diverging 1

Matrix-MemShared Int	0: memory for coefficient matrices for all points reserved 1: memory for coefficient matrices is shared	0, for high mem require-ment 1
LogLevel Int	-1: no data to log 0: only the most important data are written to the log file(no residuum only timestep and CPU time) 1: residuum log for all blocks summarized 2: residuum of each block logged separately 2-8: stepwise more information logged	1
ResidiumType Int	0: Residii given for each equation 1: components are summarized for each block	0

Initialization	Description	Chosen pa-rameters
Ptot Double	Total pressure with which simulation is initialized	3.0e5
Ttot Double	Total temperature with which simulation is initialized	250
InVel X="100" Y="0" Z="0"	Velocity components for initialization	100 m/s in x
IsQuasi3D Int	0: Full 3D 1: Quasi-3D	0
PrimVarReload Int	0: don't reload prim. Variables 1: check ijkmax in file 2: old format (use primVarInterpolK.bin to start LES)	1
ModuloReadControl Int	Read control.xml file every x steps	10
ReadBinGrid Int	0: read geom.bin if geom.bin not existent read geom.txt and write geom.bin 1: read geom.txt	1

Solver	Description	Chosen parameters
NPreiterationsCoarse Int	Number of pre-iterations on coarse grid	Couple of hundred when ramping up simulations
UnderRelaxParam Double	The % of change used to update the flow variables 0.6-0.9 for unsteady 0.5 for steady. 4 Newton iterations with underrelax 0.6 $\rightarrow (1-(1-0.6)^4) = 97\%$ timestep	0.5
NewtonsIterations Int	Number of Newton iterations 1 for steady, 2-3 for unsteady simulation	1
GausSeideliterations Int	Number of Gauß-Seidel iterations	1
ModuloGaussSeidel Int	Gauss-Seidel sweep every nth line	1
ImproveDiagonalDominance Int	0: don't improve 1: improve	1

PhaseLagInterface	Description	Chosen parameters
PLIFAType Int	0: no phase-lagged BCs 1: not defined 2: read information from controllPhaseLag.xml	0

Transition	Description	Chosen parameters
UseTransition Int	0: no transition model 1: gamma-Reth with Kelterer correlation 2: gamma-Reth with Menter correlation 3: gamma-Reth with Malan/Trace correlation	0
TransReload Int	Reading and initialization of transition variables from primVarGARE.bin	0

Turbulence	Description	Chosen parameters
UseViscous Int	0: Euler 1: laminar 2: Spalart Allmaras 3: SSTMenter 4: Wilcox k- ω 5: V2FModell 6: LKE Modell 7: Smagorinsky model	2 for initiation later 3
TurbReload Int	0: no reload 1: check ijkmax in file 2: old format	1
FreezeTurbVar Int	0: no freeze 1: freeze variables	0
ConstViscosity Int	0: use Sutherland law 1: use value given by dyn.viscosity	0
DynViscosity Double	Value of DynViscosity	1.876e-5
MaxDistToWall Double	If wall distance algorithm doesn't find a solution value is set for wall distance if calculated value is larger than MaxDistToWall then MaxDistToWall which is given is used	1e+20
SA_ProductionLimiter Int	0: original model 1: production term limiter according to Oliver, PhD thesis MIT, 2008	0
KOProductionTerm Int	0: S*S 1: S* Ω 2: Ω * Ω	1
SSTMenter 2003 Int	0: Original Menter SST model 1: Menter SST model of 2003	0
KOWilcox2006 Int	0: Original Wilcox model 1: Wilcox model of 2003 is used	0

Output	Description	Chosen parameters
ModuloWriteVar Int	Write primVar.bin every nth time step	500
ModWriteGr2 Int	Write gr2files every nth time step	0 (needed for inhouse viewer or Ansys CFD-Post)
ModWriteGrf Int	Write grf-files every nth time step (needs special control file)	0
ModWriteTec Int	Write binary Tecplot file every nth time step	500
ModWriteBody Int	Write txt file for all boundaries	500
WriteUnstWall Int	0: for steady 1: for unsteady write txt file every nth time step	0
ModOutputResid Int	Append residuum every nth time step at res_log.txt	10
ModWritePos Int	Write grf-Files every nth time step for a given number of points (given in posOutputAll.xml)	0

AlertLimit	Description	Chosen pa- rametes
AlertLimitMax_Rho Double	Alerts the user in the log.out file about exceeded values	10
AlertLimitMin_Rho Double		0.01
AlertLimitMax_P Double		1e+8
AlertLimitMin_P Double		1000
AlertLimitMin_Omega Double		1000
CorrectLimitMax_Rho Double	If given values are exceeded, values will be replaced with given values	20
CorrectLimitMin_Rho Double		0.001
CorrectLimitMax_P Double		1e+10
CorrectLimitMin_P Double		100
CorrectLimitMin_Omega Double		500
PromptLimitVolRatio Double	Alerts user if volume ratio from first to second cell from wall is exceeded	3
AbortLimitVolRatio Double	Aborts simulation if volume ratio from first to second cell from wall is exceeded	5

Special		
BetaIncompRefVel Double	Value needed to calculate mBetaIncomp for incompressible Code	20
BetaIncompNondim Double	Value needed to calculate mBetaIncomp for incompressible Code	0.5
CentralEps2 Double	Parameter of the additional damping function for central algorithm	0.001
AddToPrimMean Int	1: The results of the k planes are summarized over all time steps so that a time/space average is written for kmax01 (intended for LES of a "2D" configuration)	

Table 8.1: Linars settings

8.4 Convergence evaluation

Linars will provide several output files, for initial convergence analysis `res_log.txt` can be evaluated. It contains the residuals for each block and each equation separately or all residuals summed depending on the settings chosen in `control.xml`. For this simulation the residuals of every block were given separately but all equations were summed to give a faster overview of all blocks. A sample convergence can be seen in Figure 8.3 which has been evaluated with python.

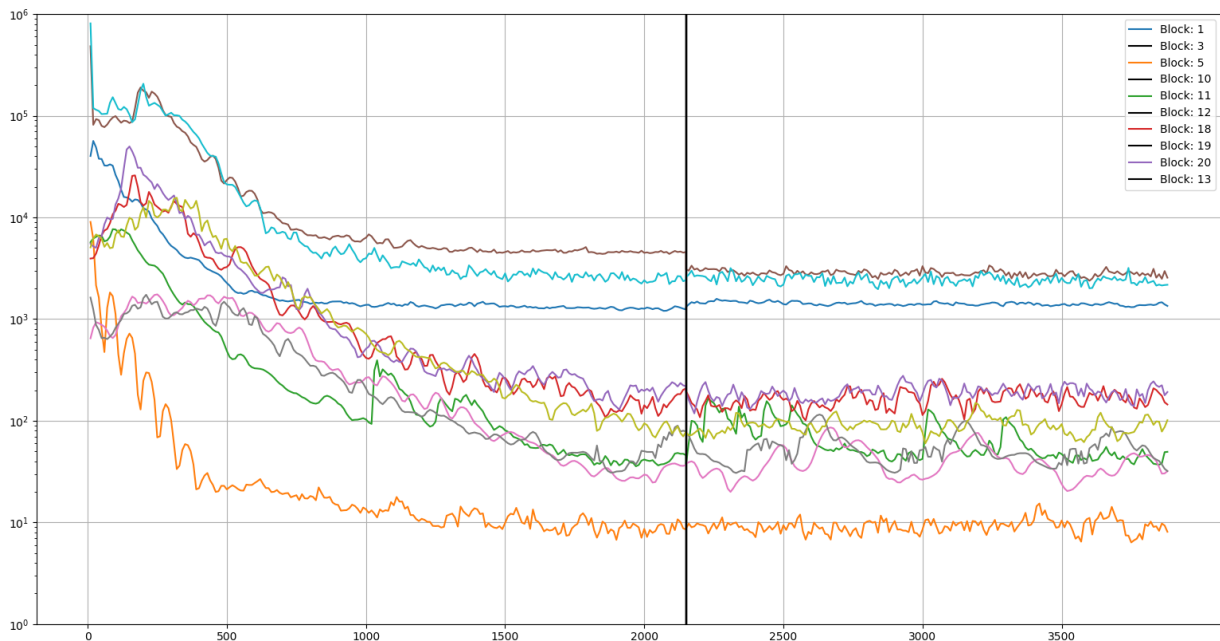


Figure 8.3 Convergence example

The abscissa in Figure 8.3 shows the amount of iterations and the ordinate shows the size of the residuals. The black vertical line at 2200 iterations signalizes that a pre-iteration ended as planned and a continuation was performed. Fluctuations show the convergence behaviour of the blocks and they are noticeably stronger for certain blocks. They are partly from the unsteady behaviour of the flow. To assure convergence the shear stresses in the wall boundary files were analysed. The boundary files were saved in 500 iteration step intervals and the shear stresses for each wall-boundary were summarized and then compared with values 500 steps down the line until a threshold of 0.2 % shear stress variation was achieved. The shear stresses are the best indicator for a simulation to have reached full convergence. This evaluation was also carried out with python. In

Table 8.2 the change of the shear stresses of the basic model's simulation summarized for each block in % after 500 additional iterations can be seen. Face of block describes the cells face: 2 stands for -k; 4 for +j and 5 for +k

Table 8.2: Variation of shear stresses summarized for each block after 500 iterations for the basic simulation

	Block Nr.		Face of block	Variation [%]
Block	10	Out	5	0.49
Block	0	Out	2	0.02
Block	1	Out	2	0.03
Block	2	Out	2	0.01
Block	3	Out	2	0.04
Block	4	Out	5	0.05
Block	5	Out	5	-0.03
Block	1	Out	5	-0.05
Block	2	Out	5	0
Block	3	Out	5	0.07
Block	4	Out	5	0.04
Block	0	Out	4	0.02
Block	5	Out	4	0.0

8.5 Computational hardware infrastructure

All simulations were carried out on the iCluster of the Graz University of Technology. This cluster uses Debian GNU/Linux as an operating system. The cluster is equipped with 2,8TB in memory, 10TB in storage and 704 CPUs split up in 8 nodes of 32 CPUs and 7 nodes of 64 CPUs equipped with 128GB and 256GB of memory each, respectively. For the steady simulations thirteen to eighteen CPUs were used with approximately 40GB of RAM.

8.6 Geometry

For the simulations 7 different setups were created: three forward-facing steps with 0.4, 0.8, 1.3 mm in step height at the hub, three backward-facing steps with 0.4, 0.8, 1.3 mm in step height and a basic setup with no steps. In succeeding chapters, the 1.3mm, 0.8mm and 0.4mm steps will be labelled 13, 8, 4 respectively with the addition of “+” for the forward-facing step and “-” for the backward facing step. A cut-out of the grid at the step of the 1.3mm backward-facing step is visible in Figure 8.4. The hub contour up to the step was considered as rotating for all simulations. The vertical face at the step was modelled as non-rotating for the forward-facing step and rotating for the backward facing step.

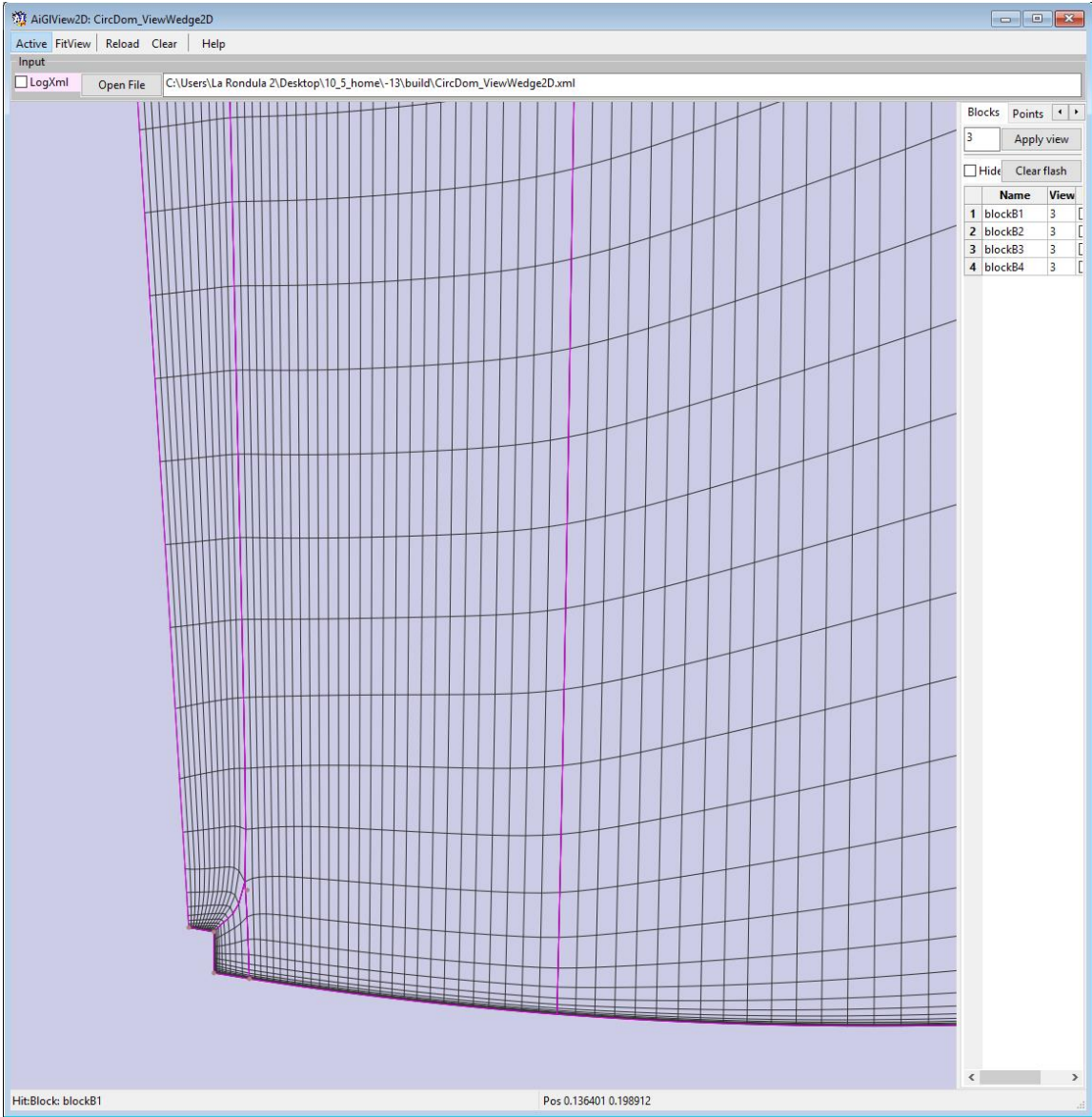


Figure 8.4: Mesh of the backward-facing step

The entire calculation domain can be seen in Figure 8.5. The LP rotor was not modelled since no relevant changes were expected there. The step at the shroud was removed after a simulation revealed that the forward-facing step there resulted in a far-reaching separation zone at the shroud. This separation didn't terminate within the HP rotor domain even after shifting the domain interface more downstream. For the mixing-plane interface Linars sets negative velocities to 0 there, which falsifies the results. In order to avoid this problem, the shroud was modelled without steps in the flow path. All models consisted of roughly 10 million cells. Iterative measures were taken in order to assure a good mesh quality.

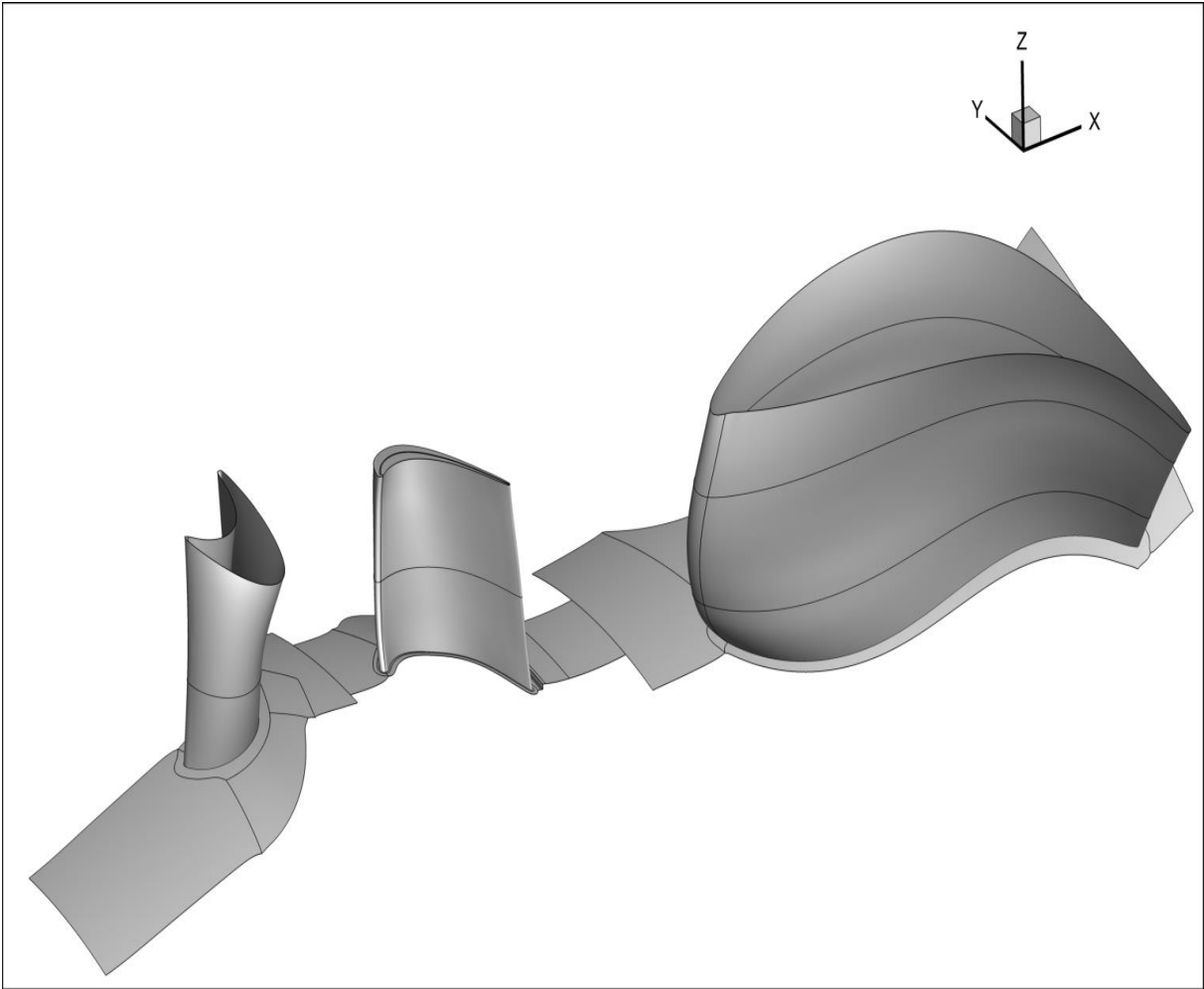


Figure 8.5: Entire calculation domain

8.7 Boundary conditions

The basic setup boundary conditions were chosen according to the measured boundary conditions for the basic setup. The shifted model's static outlet pressure was corrected which will be mentioned in chapter 9.1 The boundaries can be seen in

Table 8.3

Table 8.3: Boundary conditions for the basic setup

	Value	Unit
Rotational speed HP rotor	-1157.607	Rad/sec
Inlet total pressure	3,97707157e5	Pascal
Outlet static pressure	1,117909e5	Pascal
Inlet total temperature	436,629	Kelvin

8.8 Evaluation planes

To evaluate the simulations and fully capture the effect of the different step heights on the efficiency and on secondary flows, additional evaluation planes were set up which are visible in Figure 8.6 and more detailed in Figure 8.7. Plane C1 was placed just behind the HP rotor and before the step. Plane C2 was placed just behind the step. C2 will be of less interest, since for the bigger step heights the reattachment hasn't fully occurred. Plane D1 was placed just behind the mixing plane and plane D2 was placed within the MTF. Another Plane was placed just before the mixing plane in order to capture potential losses but won't be mentioned in the results.

The focus will be on the comparison of the losses between plane C1 and plane C since the reattachment of all separation zones has occurred at this point. Further downstream it will be of interest to see the losses between plane D1 and exit plane E not directly affected by the separation at the step. Losses in this region can be expected mainly due to changes in yaw angle which could result in a wrong incidence onto the MTF resulting in possible separations or stronger secondary flows in the MTF like mentioned in Bauinger's work [16].

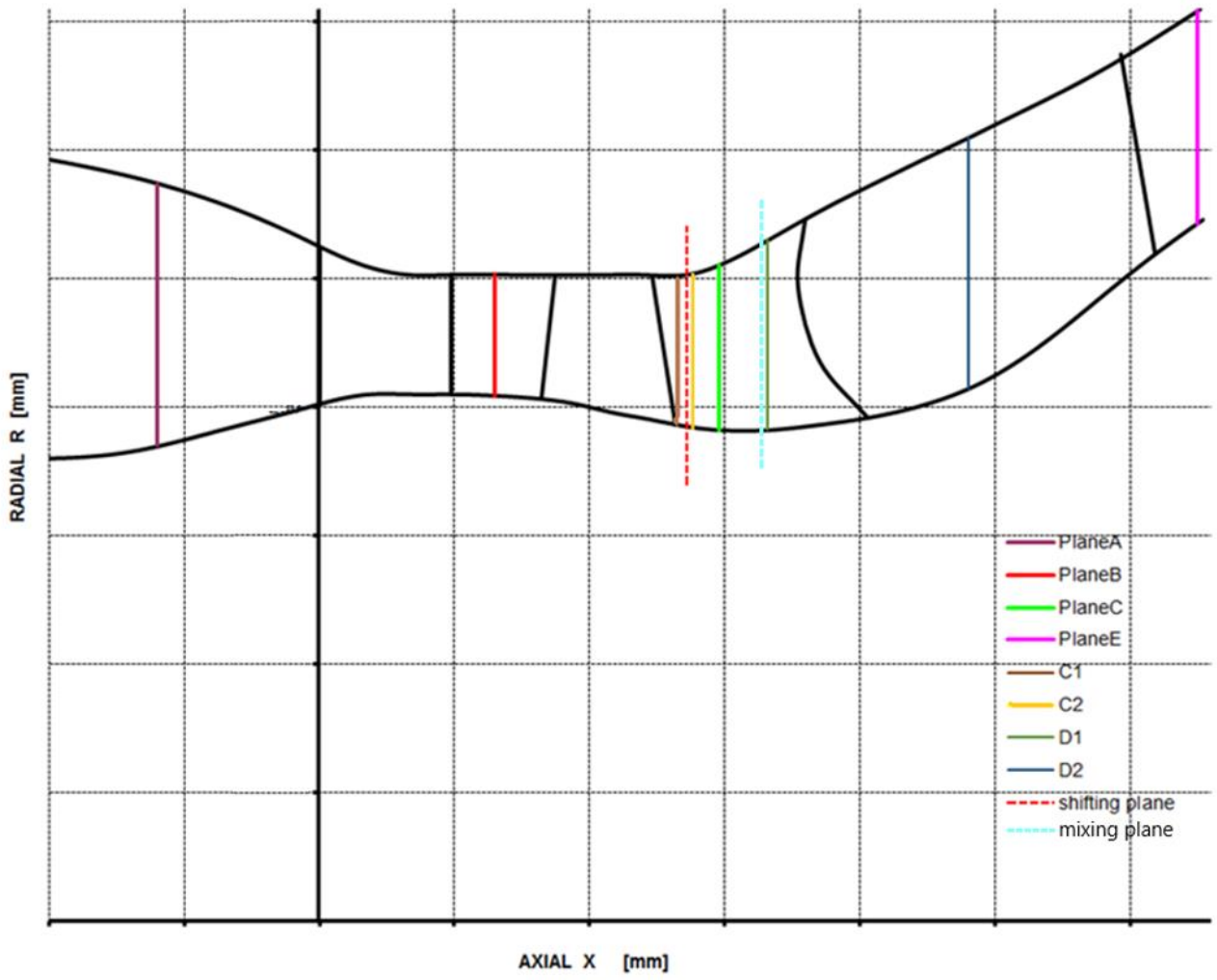


Figure 8.6: Axial cross section of measurement planes

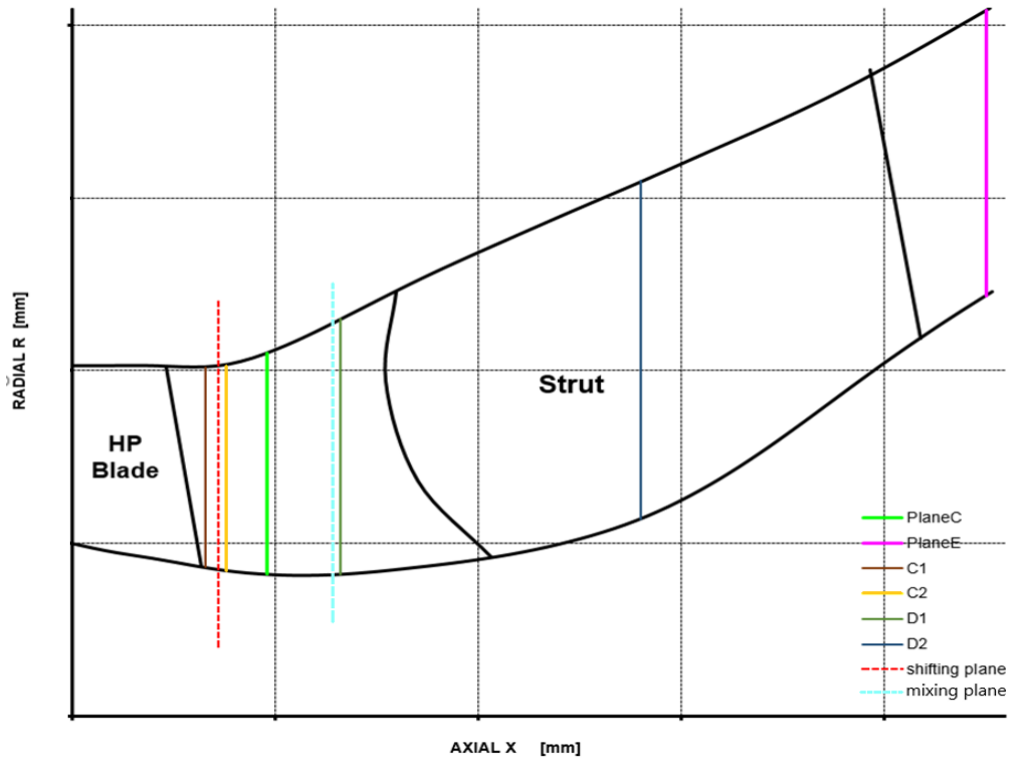


Figure 8.7: Detailed axial cross section of measurement planes

Additionally, four equally spaced axial cross sections were made at the step. In order to capture the separation zones and secondary effects at the step. These four planes are visible in Figure 8.8. Labelled from 1 to 4 and are placed at 0%, 25%, 50% and 75%, circumferential position of the rotor spacing. When these cross sections will be referred to in succeeding chapters they will be listed as in Figure 8.8.

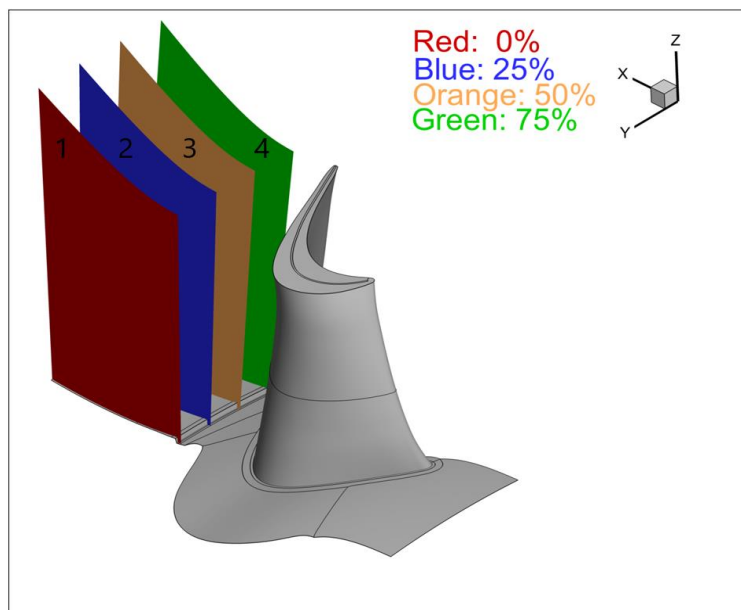


Figure 8.8: Axial evaluation planes behind the rotor

9. Results

In this chapter the data gathered from the simulation will be evaluated and compared to the measurement data. All absolute values have been made dimensionless due to disclosure reasons. Pressures, Mach numbers and temperatures were referenced to the mass averaged pressure, Mach number and temperature of the observed plane. Yaw and pitch angle figures are represented without absolute values. Furthermore, the temperatures from the simulations will not be compared with the measurements because the temperatures of the measurements resulted in an unrealistic low isentropic efficiency. The total pressure coefficient was calculated with equation (9-1)

$$c_{pt} = \frac{p_t - \overline{p_{ref}}}{\overline{p_{t,ref}} - \overline{p_{ref}}} \quad (9-1)$$

$\overline{p_{ref}}$ stands for the area averaged pressure of the reference plane and $\overline{p_{t,ref}}$ is the mass averaged total pressure in the reference plane. All contour plots showing the channel viewed against the flow direction.

9.1 Approach

To ensure a reliable comparison with the measurements, a similar approach was used as in the PhD thesis of Bauinger [16]. First the basic simulation without step was carried out by fitting the same boundary conditions in the basic measurement setup. The following shifted simulations were fitted with the identical inflow boundary conditions of the basic setup. Lastly with an iterative process the outlet static pressure was adjusted in order to achieve the same pressure ratio of the HP stage as in the basic setup. The pressure ratio between a plane located 2mm behind the inlet and plane C1 just behind the high-pressure rotor was chosen. A plane 2 mm downstream of plane A was chosen. The difference in pressure ratio between the simulations was kept below 0.15%. The difference of mass flow at the inlet was also kept below 0.0114%. In Table 9.1 a recapitulation of the pressure ratios, variations of pressure ratios, mass flow and variation of mass flow for the simulations is listed.

Table 9.1: Differences in pressure ratio and mass flows for the simulations

Model	Inlet total pressure [bar]	Static pressure C1[bar]	Pressure ratio [-]	Variation to basic in pressure [%]	Mass flow [kg/s]	Variation of Mass flow [%]
Basic	3,97643	1,11479	3,56698	0	15,4391	
+13	3,97643	1,11471	3,56723	0,007	15,4398	0,0045
+8	3,97643	1,11643	3,56173	-0,147	15,4393	0,0010
+4	3,97643	1,11531	3,56533	-0,046	15,4409	0,0114
-13	3,97643	1,11307	3,57846	0,155	15,4383	-0,0052
-8	3,97643	1,11550	3,56472	-0,063	15,4395	0,0022
-4	3,97643	1,11394	3,56969	0,076	15,4395	0,0025

9.2 Influence of step on total pressure and isentropic efficiency

The influence of the step on the total pressure is small but still observable. A detailed recapitulation of the total pressure losses is listed in Table 9.2. The total pressure losses in % in Table 9.2 are the total pressure losses between plane C1 and the respective plane divided by the total pressure of plane C1 times hundred. For disclosure reasons the values were all made relative to the basic setup. The stepwise total pressure loss in % shows in which segments the total pressure losses occur. Column D1 represents the increase in total pressure losses in %-points compared to C. Column D2 represents the increase in total pressure losses in %-points compared to D1. Column E represents the losses also compared to D1. This facilitates to distinguish losses occurring in the MTF. Further correction has been made by excluding the total pressure losses occurring due to the mixing plane. As mentioned in Chapter 8.6 the total pressure losses up to plane C are interesting ones since the reattachment has already occurred and the disturbance created by the steps should have increased the total pressure losses. It was observed that small backward-facing steps show relatively high losses. The forward-facing step of 1.3mm generates significant higher losses than the 0.8mm or the 0.4mm step. Further it is observed that the backward-facing steps are partly responsible for higher losses in the MTF compared to the forward-facing steps. A possible explanation for this phenomenon will be discussed in chapter 9.7.

Table 9.2: Total pressure losses compared to plane C1

Total pressure loss		C	D1	D2	E
Basic	Stepwise total pressure loss [%-points]	0,0	0,99	0,69	1,75
1.3mm	Total pressure loss compared to basic [%]	+4,84	+3,51	+2,54	+2,61
	Stepwise total pressure loss [%-points]	0,0	1,00	0,69	1,77
0.8mm	Total pressure loss compared to basic [%]	+1,61	+1,40	+1,69	+0,65
	Stepwise total pressure loss [%-points]	0,0	1,00	0,71	1,74
0.4mm	Total pressure loss compared to basic [%]	+9,14	+0,35	+0,85	+0,22
	Stepwise total pressure loss [%-points]	0,0	0,83	0,71	1,75
-1.3mm	Total pressure loss compared to basic [%]	+3,23	+0,70	+1,98	+2,39
	Stepwise total pressure loss [%-points]	0,0	0,95	0,74	1,85
-0.8mm	Total pressure loss compared to basic [%]	+5,91	+4,56	+4,80	+4,35
	Stepwise total pressure loss [%-points]	0,0	1,01	0,73	1,82
-0.4mm	Total pressure loss compared to basic [%]	+2,69	+0,70	0	+1.30
	Stepwise total pressure loss [%-points]	0,0	0,96	0,67	1,79

Cumulative losses for the 1.3mm forward facing step and the 1.3mm backward facing step can be seen in Figure 9.1 and Figure 9.2. The figures reveal that forward-facing steps tendentially cause higher losses immediately after the disturbance and backward-facing steps are prone to generate higher losses in the MTF. Interestingly, most losses in total pressure occur up to plane D1 over a short axial distance with little differences between the different setups. It is interesting that the simulations show results for the 0.8 mm backward/facing step which do not follow the expected tendency of increased losses with increased step height.

Isentropic efficiencies can be seen in Table 9.3 and are defined as $\eta_i = \frac{T_{t2} - T_{t1}}{T_{t2'} - T_{t1}}$ with T_{t1} as the total temperature in plane A, T_{t2} as the total temperature in the respective plane and $T_{t2'}$ as the total isentropic temperature. No real conclusion can be drawn from the isentropic efficiencies. All shifted setups present approximately a 0,1%-point decrease in efficiency in plane E. The isentropic efficiencies for the shifted setup in plane E are on average 0.1%-points above the basic setup. Interesting is the low isentropic efficiency of the 0.4 mm forward-facing step in

plane C which doesn't correlate with the efficiencies from the other models. Further it should be noted that the isentropic efficiencies from Plane D2 to plane E increase for all models except the 1.3 mm backward facing step.

Table 9.3: Isentropic efficiency in relation to plane A relative to basic setup in[%].

	C	D1	D2	E
+13	-0,38	-0,06	+0,39	+0,15
+8	-0,26	-0,03	+0,35	+0,15
+4	-1,39	+0,09	+0,39	+0,19
-13	-0,31	+0,12	+0,21	-0,45
-8	-0,37	+0,14	+0,32	+0,06
-4	-0,43	+0,10	+0,39	0,08

When Table 9.1, Table 9.2 and Table 9.3 are compared to each other a relation can be seen between the total pressure losses and the mass flow. A higher mass flow resulted in higher total pressure losses. The mass flow difference for the -13 simulation compared to the basic simulation is very small with -0,0052% but it would explain why the -13 is not following the trend of the backward-facing steps in terms of total pressure loss. Perhaps if the -13 model had the exact same mass flow as the other backward-facing step models, the total pressure losses of the 1.3 mm backward-facing step would be above the 0.8 mm backward-facing step. The +0.4 mm forward-facing step shows high losses up to plane C combined with lower isentropic efficiencies compared to the bigger 0.8 mm forward facing step. This could also be explained with the higher mass flow, which is 0.0114% above the basic simulation mass flow.

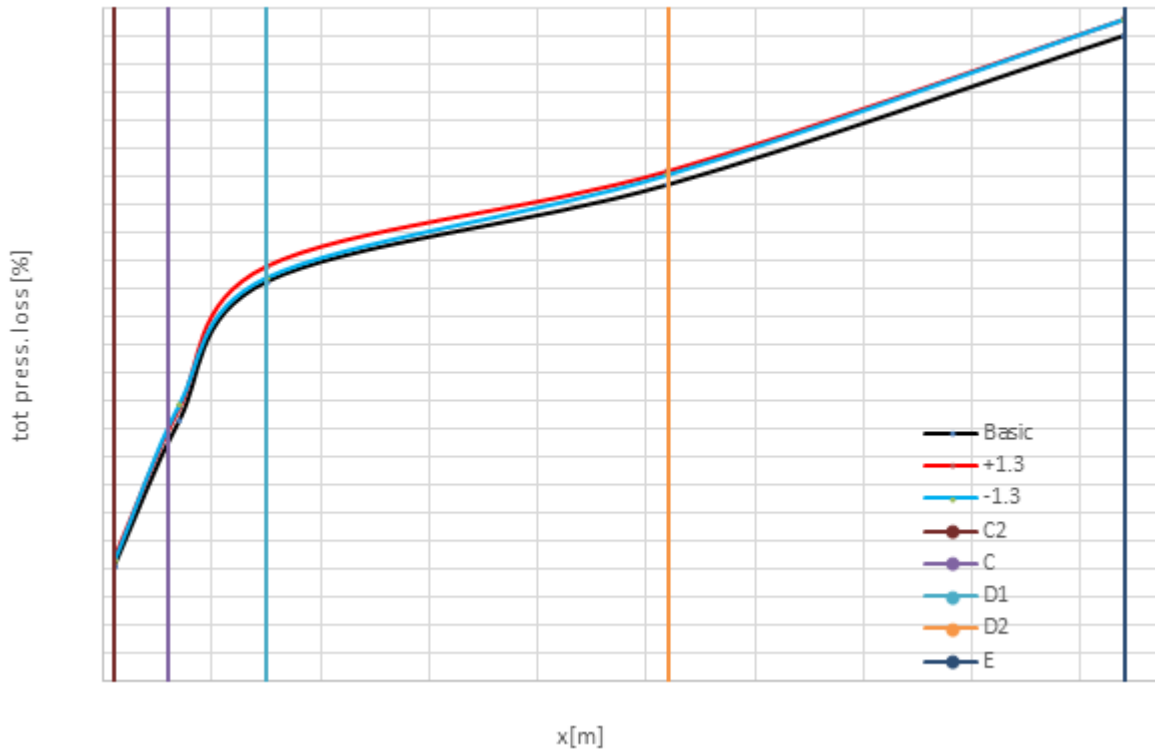


Figure 9.1: Total pressure loss in [%] compared to plane C1

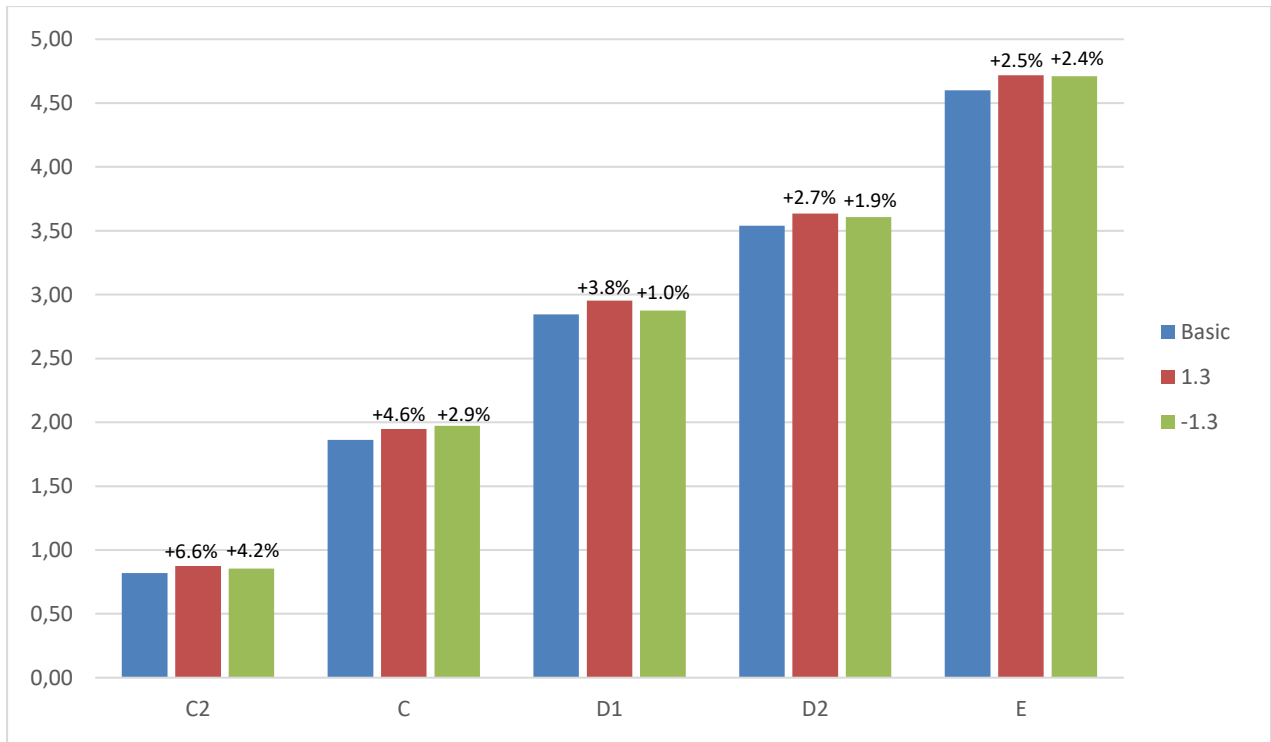


Figure 9.2: Total pressure loss in [%] compared to Plane C1 and relative to basic setup

9.3 Evaluation of Plane C

9.3.1 Comparison of the maximum step heights with the measurement data in Plane C

The simulations for a step at the hub with a height of 1.3 mm are compared with radial measurements performed in a plane where the radial shift is about 0.4 mm at the hub. The step at the outer casing is not simulated. The simulations agree qualitatively well with the measurements. The total pressure coefficient visible in Figure 9.3a shows differences between the measurements and the simulations at 90% channel height with higher values in the simulations. At 80% channel height the simulations show a decreased total pressure coefficient. The +13 simulation and the shifted measurement show a relative increase in pressure coefficient at this relative channel height. In the near-hub region, the simulations differ from the measurements. The simulations themselves also show differences in this region with a decrease of the shifted-setup values below 5% channel height.

Similarities with the measurements of the Mach number visible in Figure 9.3g can be found. The +13 simulation shows an increased Mach number at around 10% channel height and the -13 simulation a decreased Mach number compared to the basic setup. Below 5% channel height both shifted simulations have lower Mach numbers compared to the basic setup.

In Figure 9.3c the -13 simulation shows a permanent increased temperature throughout the entire channel with its largest deviation in the lower channel part whereas the +13 simulation shows a slight decrease in static temperature. The agreement of the total temperature indicates very little differences in power conversion.

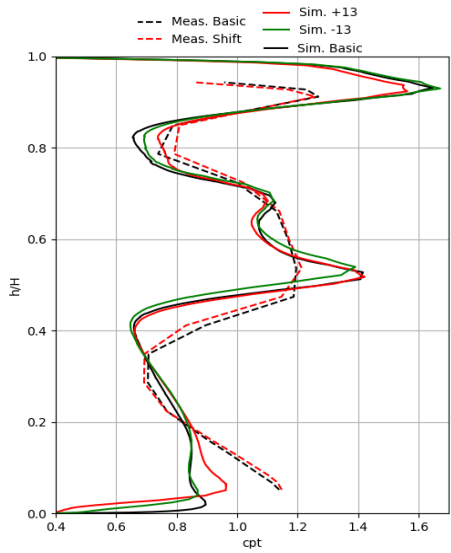
The yaw angle distributions visible in Figure 9.3f present similarities with the Mach number. The simulations have bigger yaw angles at 90% channel height compared to the measurements. The measured shifted setup presents increased yaw angles at 10 and 60% channel height, which cannot be found for the simulations except the increase at 10% channel height for the +13 simulation. The most noticeable difference can be seen in the near-hub region where the yaw angles for the shifted simulated setups decrease. The +13 simulation shows the sharpest decrease.

The measured pitch angles visible in Figure 9.3e are mostly lower than the ones obtained from the simulation. At 90% channel height the measurement and the simulations clearly deviate, with a possible measurement error in the near-shroud region. The shifted measurement shows a decrease compared to the basic setup throughout the channel of around 1-2 degrees. The -13

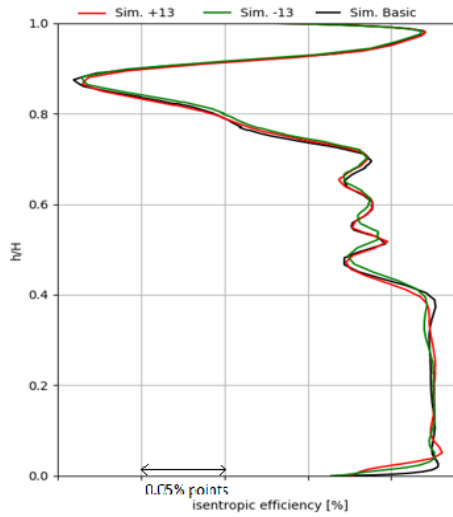
simulation shows a constant lower angle than the +13 simulation from 5-80% channel height. A spike can be seen in the near-hub region for the measured and simulated +13 setup.

Isentropic efficiency, visible in Figure 9.3b, hints that both shifted setups have lower efficiencies up to approximately 5% channel height of which the forward-facing step efficiency is lower.

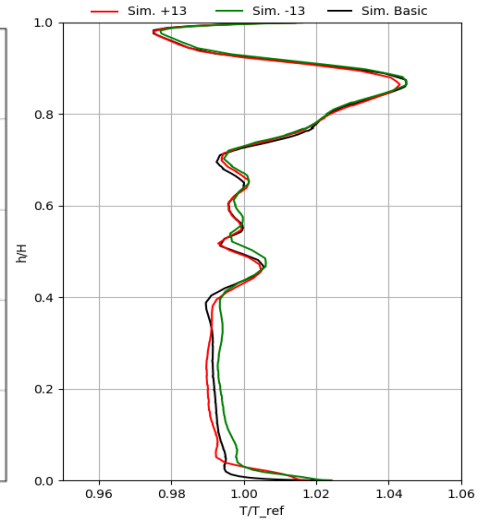
Vortices can be identified by the high Mach number at 90% channel height which is caused by the tip leakage vortex. The second peak is probably caused by the upper passage vortex, whereas the peak at about 7% channel height stems from the lower passage vortex.



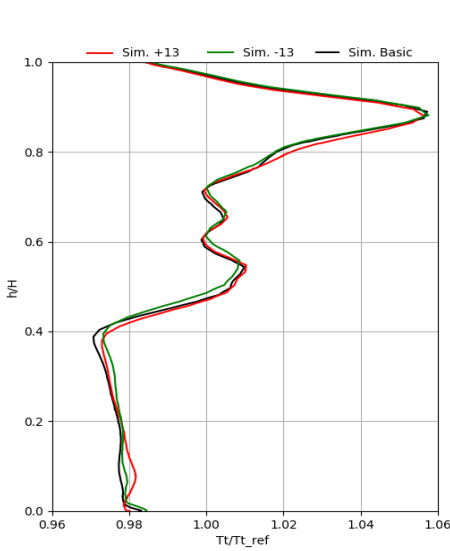
(a) Total pressure coefficient [1]



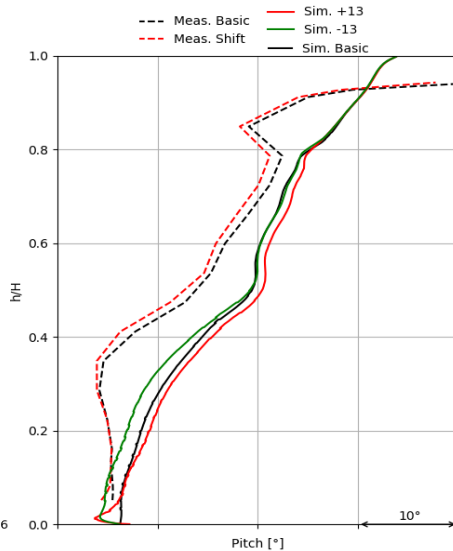
(b) Isentropic efficiency [1]



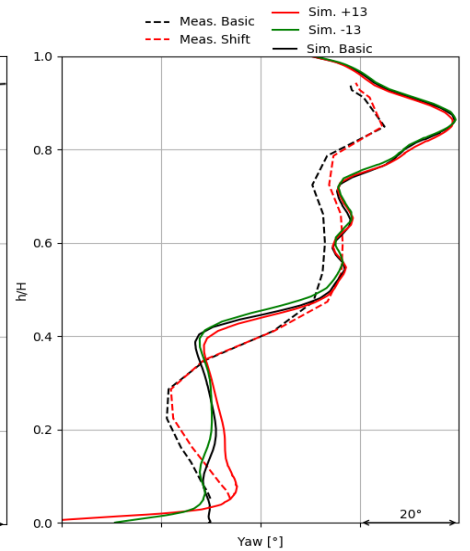
(c) Temperature [1]



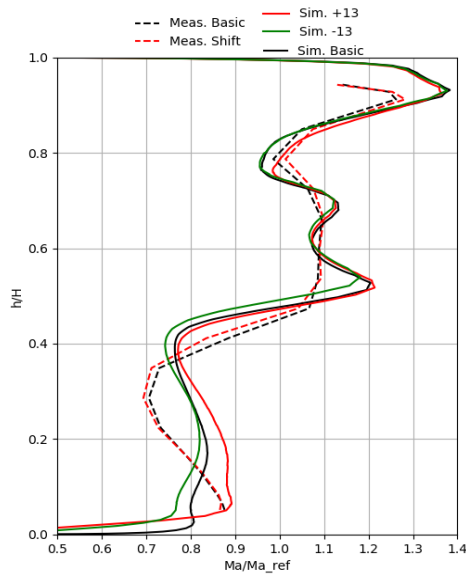
(d) Total temperature [1]



(e) Pitch angle [°]



(f) Yaw angle [°]



(g) Mach number [1]

Figure 9.3: Mass and area averaged plots for maximum step heights in plane C

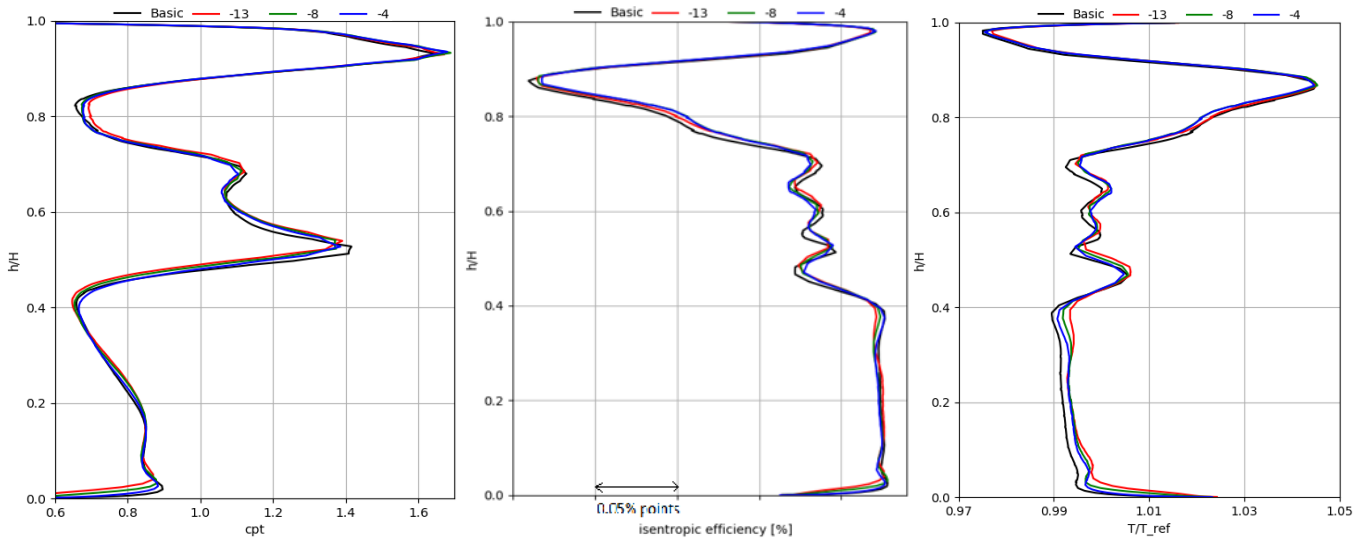
9.3.2 Comparison of the backward-facing step simulations in Plane C

In this chapter the different results for the backward-facing steps are evaluated in order to see trends.

For most plots in Figure 9.4 trends are visible. The most noticeable trends can be seen for the Mach number, yaw angle and pitch angles. With increasing step height, the Mach number is reduced. This trend disappears above 50% channel height, and there is an overlapping region at 25% channel height with unchanged Mach numbers. This coincides with a decreased total pressure coefficient in the near-hub region. The differences there show that the step influences the lower passage vortex.

All backward facing steps show a slightly increased temperature in Figure 9.4c with overlapping at 10 and 35% channel height like the Mach numbers. The total temperatures visible in Figure 9.4d show little variations.

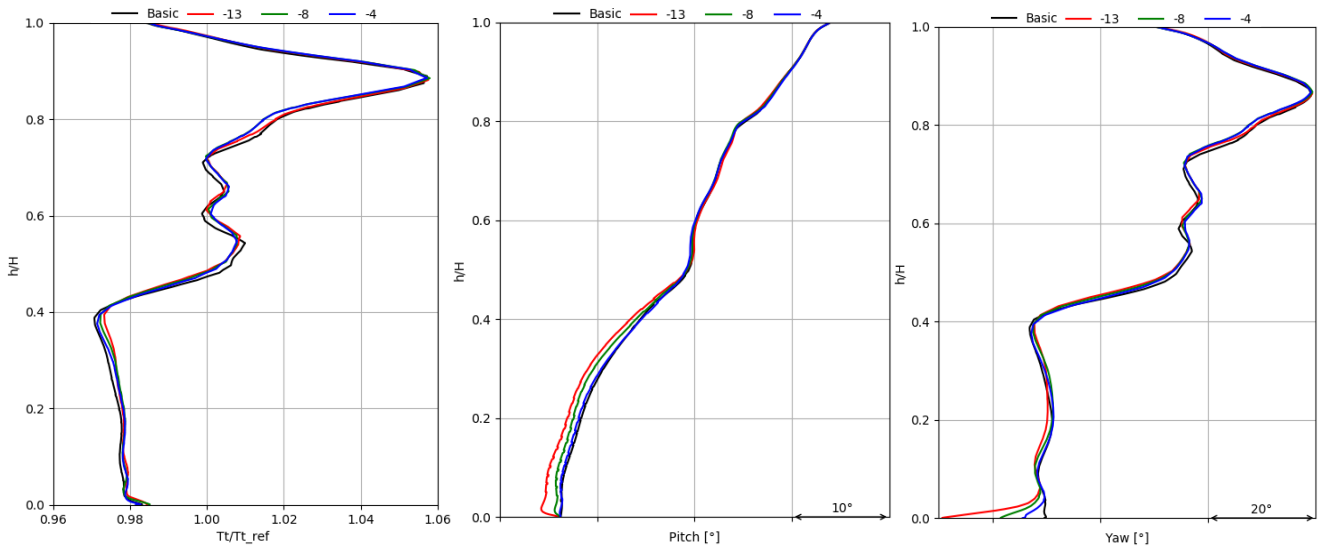
Pitch and yaw angles visible in Figure 9.4e and Figure 9.4f show trends in the lower channel half and agreement in the upper channel height. The pitch angle has a steady decrease with an increase in step height up to 50% channel height. Yaw angles show a steady decrease at the hub with an increase in step height. At 10 % channel height the yaw angles agree.



(a) Total pressure coefficient [1]

(b) Isentropic efficiency [1]

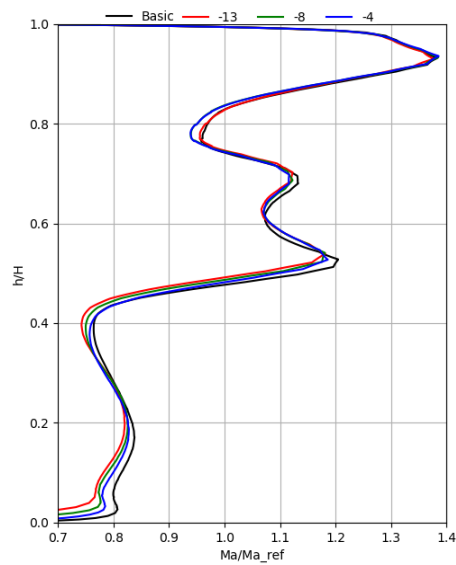
(c) Temperature [1]



(d) Total temperature [1]

(e) Pitch angle [°]

(f) Yaw angle [°]



(g) Mach number [1]

Figure 9.4: Mass and area averaged plots for the backward facing step in plane C

9.3.3 Comparison of the forward-facing step simulations in plane C

The radial plots in plane C for the forward-facing steps, visible in Figure 9.5, show tendencies which increase with an increase in step height. Mach numbers visible in Figure 9.5g show an increase in Mach number at 10% channel height and a decrease in Mach number at 5% channel height. This increase in speed vanishes at 40% channel height. Furthermore, the shifted setups present an increase in Mach number at 80% channel height. A visible increase in Mach number can be observed for the shifted setups. The total pressure coefficient reflects the same behaviour found for the Mach number.

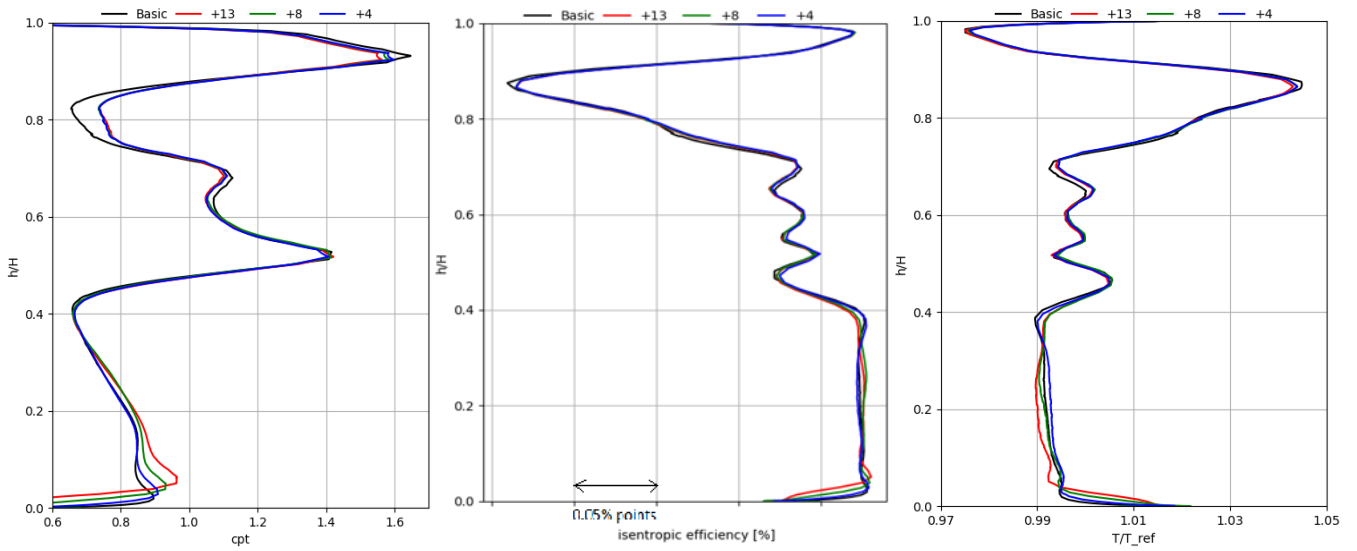
The temperatures visible in Figure 9.5c show a trend up to 5% channel height and agree for the remaining channel height. Up to 5% channel height the static temperature increases with an increase in step height.

The total temperatures visible in Figure 9.5d show strong overlapping. A visible trend can be seen at 10% channel height where there is an increase in total temperature with an increase in step height.

Isentropic efficiency decreases with an increase in step height from the hub to 7% channel height; for the remaining channel the isentropic efficiency differs little.

Pitch angles, visible in Figure 9.5e, show little deviations throughout the channel with an increase for the shifted setups from 10% to 80% channel height of 1 to 2 degrees. Near the hub a decrease of pitch angle of around 3 degrees can be observed.

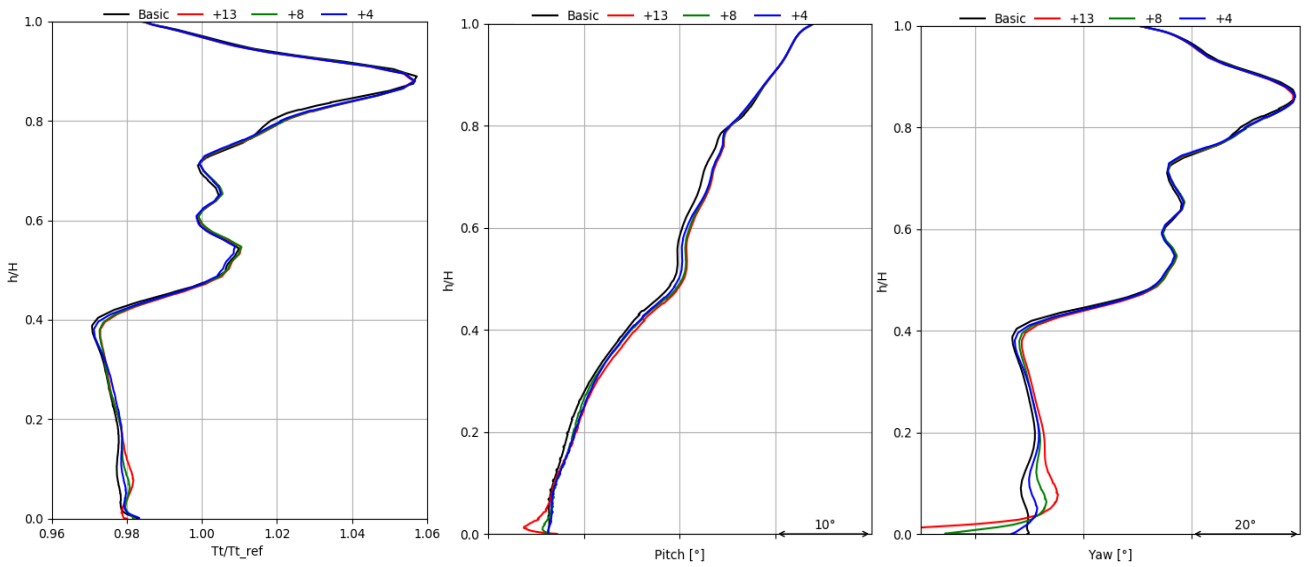
Yaw angles visible in Figure 9.5f show strong trends throughout the channel. Near the hub the yaw angle decreases with an increase in step height. Above 5% relative channel height, the yaw angle increases with an increase in step height. This indicates a strong influence of the step flow on the lower passage vortex. This effect diminishes with an increase in relative channel height and disappears at 40%.



(a) Total pressure coefficient [1]

(b) Isentropic efficiency [1]

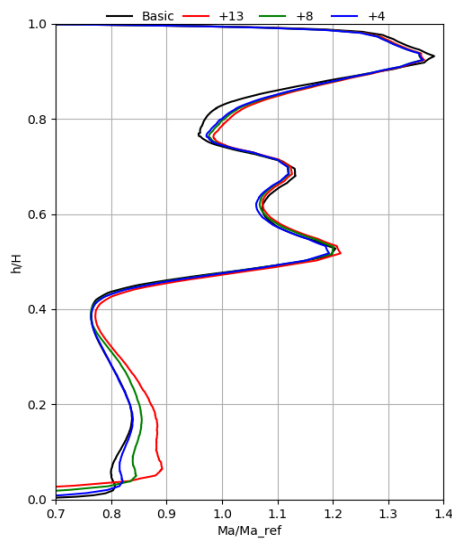
(c) Temperature [1]



(d) Total temperature [1]

(e) Pitch angle [°]

(f) Yaw angle [°]



(g) Mach number [1]

Figure 9.5: Mass and area averaged plots for forward-facing step in plane C

9.4 Evaluation of plane E

9.4.1 Comparison of the maximum step heights with the measurement data in Plane E

The total pressure coefficient, visible in Figure 9.6a, shows very little differences between the measurement setups. The simulations show an increase compared to the measurement above 90% channel height and a decrease below 10%. All simulations differ from each other in the lower channel part, but they show similarities presenting two maxima and one minimum. The difference between maxima and minimum is more pronounced for the shifted setup and there is a radial shift of these maxima and minima. The +13 simulation has its maxima closer to the hub.

The Mach numbers, visible in Figure 9.6g, increase in the measured shifted setup; an explanation to this phenomenon can be found in Bauinger's thesis. Bauinger postulates that the non-axisymmetric contour in the measurement setup creates a local restriction with disturbances at the hub and the shroud. Due to lower speeds at hub and shroud the Mach number increases throughout the channel. The axisymmetric simulation shows a significant increase in Mach number especially for the forward-facing step, whereas for the backward facing step the Mach number decreases. All shifted simulations show a slightly reduced Mach number in the near-hub region compared to the basic setup.

The static temperatures can be seen in Figure 9.6c. It can be noted that there is a reduction of static temperature for the shifted setups in the near-hub region and an increase in static temperature at 10% channel height. The backward-facing step static temperature slightly increases throughout the channel and the forward-facing step shows a decreased static temperature. The total temperatures behave similarly to the static temperatures, but they show better coincidence with the basic setup. The differences indicate differences in the power conversion.

The yaw angles are visible in Figure 9.6f. Measurements and simulations differ in the lower channel half. The simulations present lower angles than the measurements in this region and this difference amounts up to 10 degrees. The sifted simulation and shifted measurement present lower angles than their basic simulations. This difference amounts to approximately 2 degrees. Below 10% channel height the simulated shifted setups present an increased yaw angle. All simulations show 2 local maxima and one local minimum with different relative positions.

The pitch angles are visible in Figure 9.6e. The measurements show no change for the shifted setup except for a slight increase in the near-hub region, which can also be seen at the simulations. The measurements differ from the simulations in the near-shroud region and at mid channel. In the near-shroud region, the measured angles increase compared to the simulated results. At mid channel the difference between measurements and simulations is about 5 degrees.

Isentropic efficiency, visible in Figure 9.6, shows an increase in efficiency in the near-hub region for the shifted setups and a decrease in efficiency at 10% channel height.

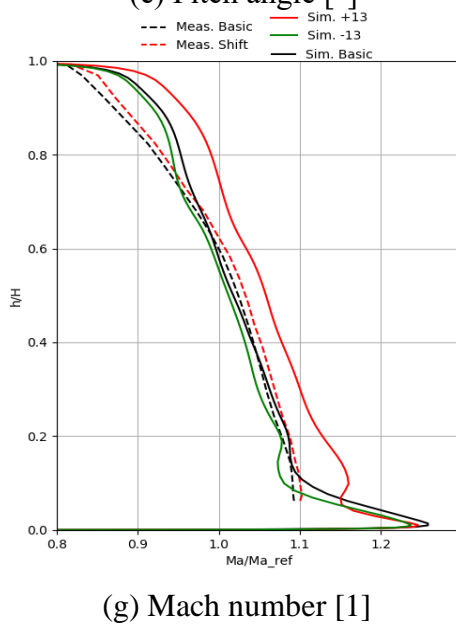
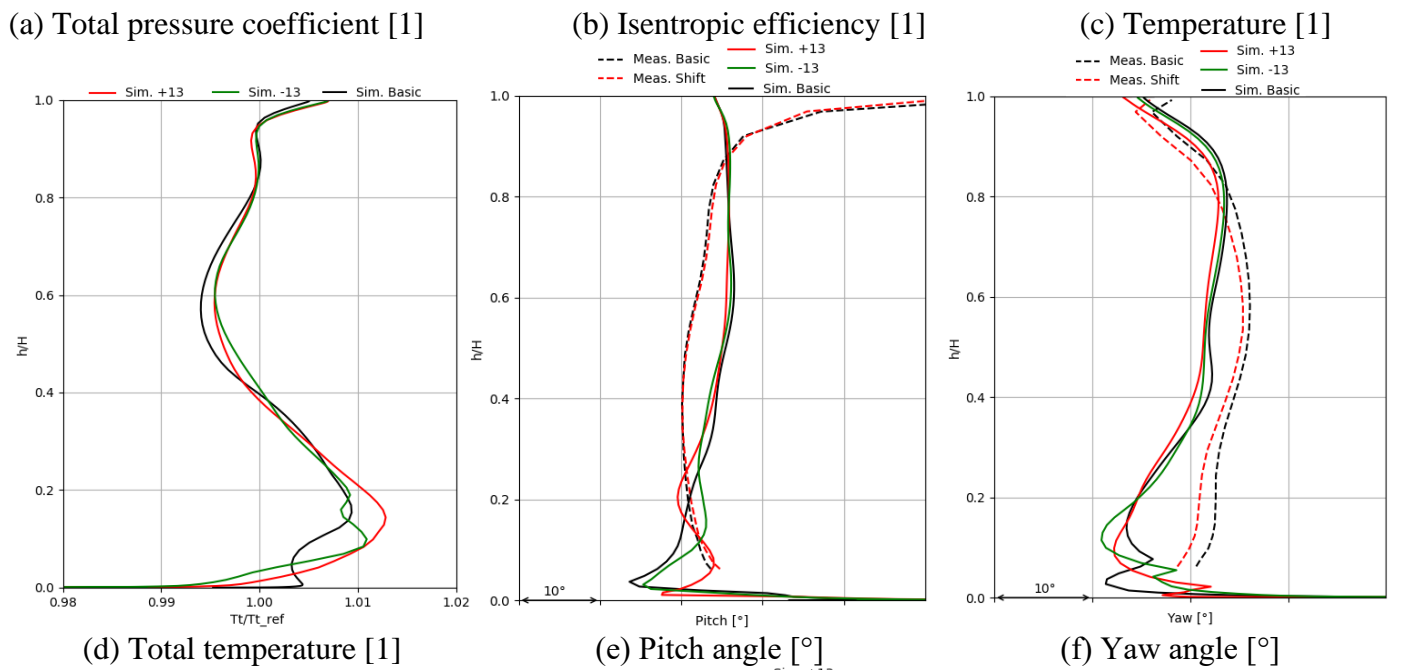
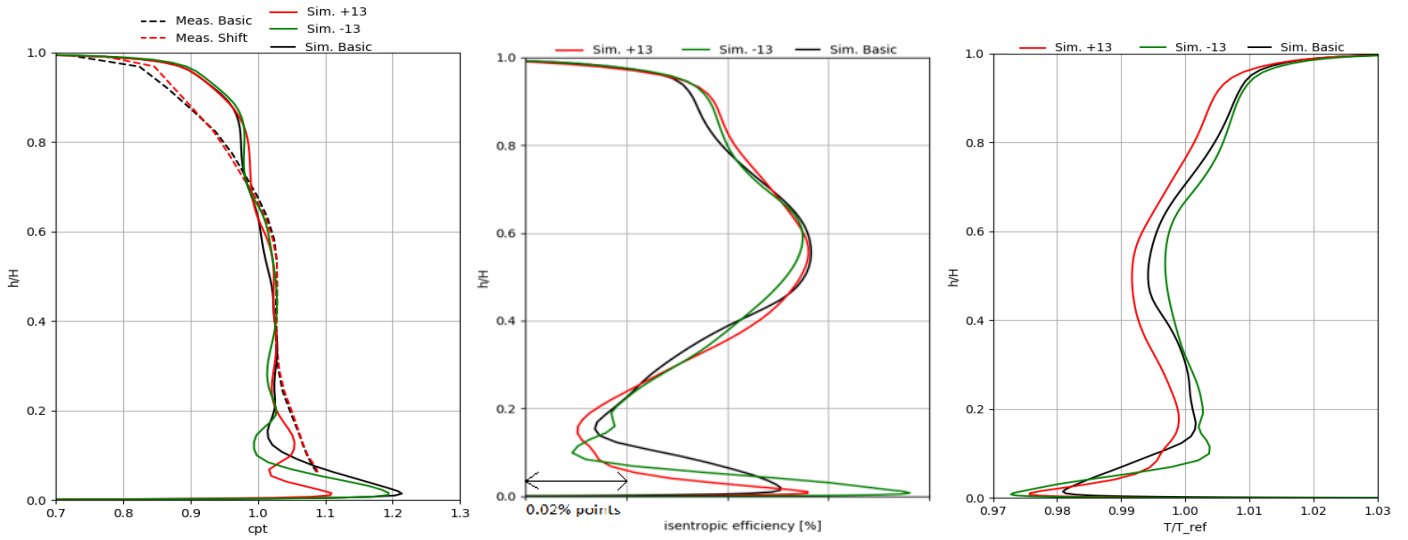


Figure 9.6: Mass and area averaged plots for maximum step heights in plane E

9.4.2 Comparison of the backward-facing step simulations in Plane E

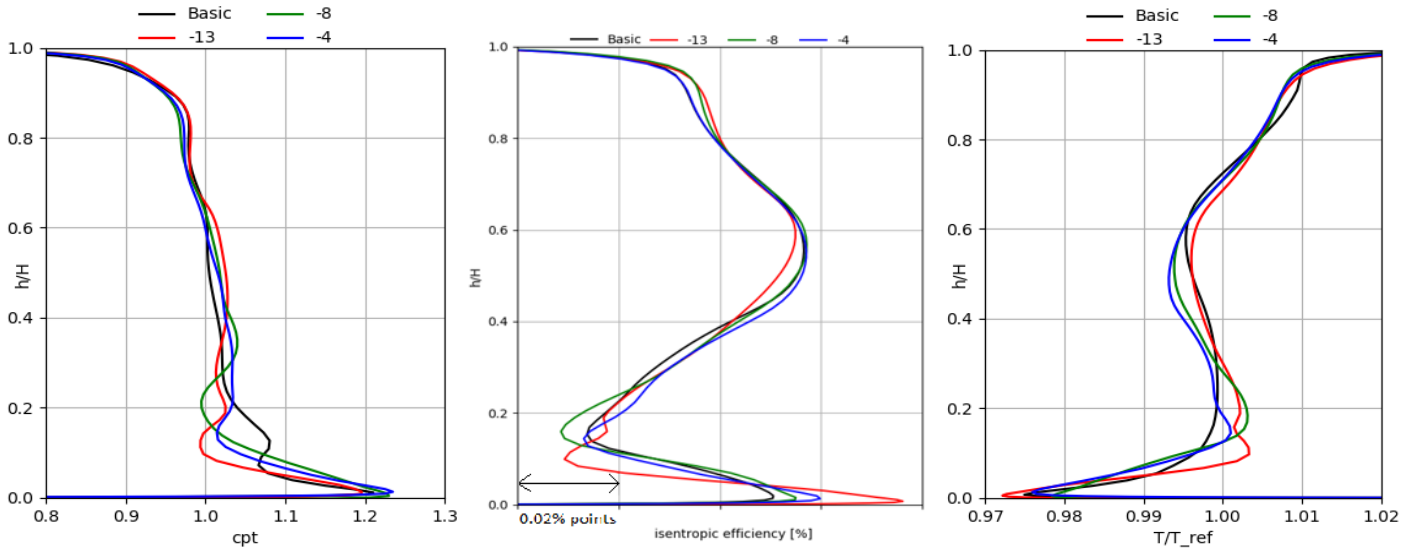
The simulation results for the backward-facing step in plane E show noticeable differences among each other but no obvious trends.

As for the Mach numbers in Figure 9.7g it can only be concluded that there is a reduction in Mach number from 10-20% channel height. This coincides with the total pressure coefficient which can be seen in Figure 9.7a showing a similar reduction at that relative channel height.

The static temperatures illustrated in Figure 9.7c increase for the shifted setup at 10-20% relative channel height and decrease from 40-50% relative channel height. The total temperatures in Figure 9.7d show the same characteristic as the static temperature with a noticeable decrease at 40-50% relative channel height. The near-hub region at 10-20% channel shows no trends.

As for the pitch angles and the yaw angles visible in Figure 9.7e and Figure 9.7f quantitative differences can be concluded but trends are not visible. Pitch and yaw angles experience a decrease from the hub to 10% relative channel height. Yaw angles increase from 10-40% channel height up to 4 degrees compared to the basic setup.

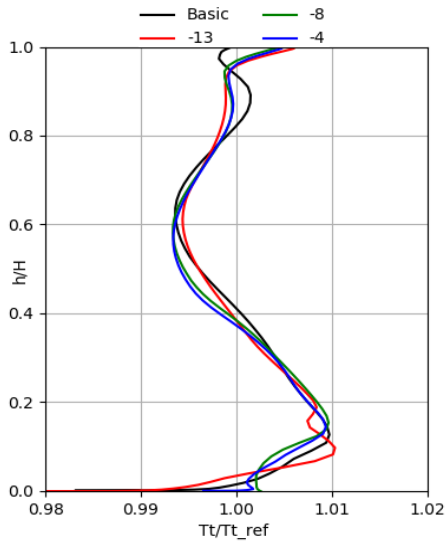
Isentropic efficiency, seen in Figure 9.7b, shows an increase in the near hub region and a decrease at 15% relative channel height.



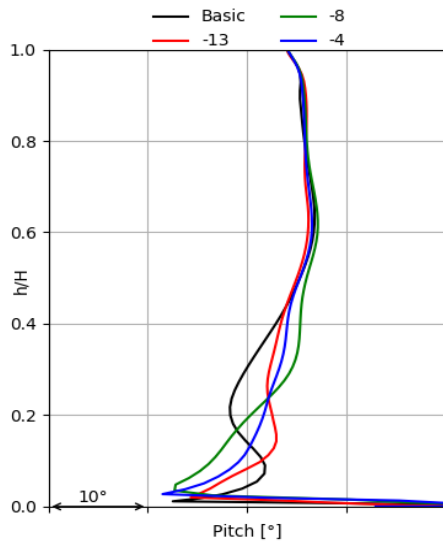
(a) Total pressure coefficient [1]

(b) Isentropic efficiency [1]

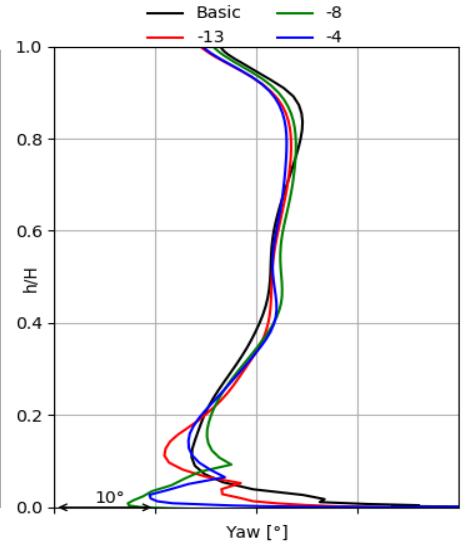
(c) Temperature [1]



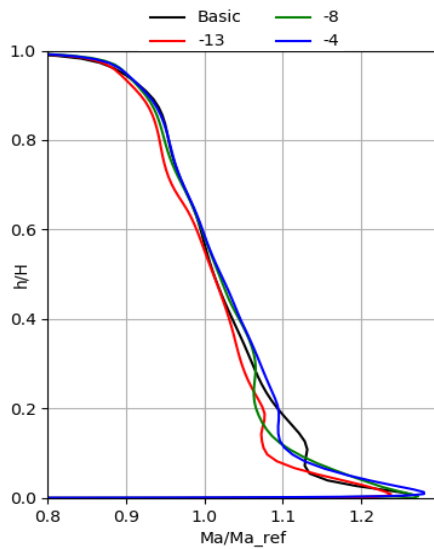
(d) Total temperature [1]



(e) Pitch angle [°]



(f) Yaw angle [°]



(g) Mach number [1]

Figure 9.7: Mass and area averaged plots for backward-facing step in plane E

9.4.3 Comparison of the forward-facing step simulations in plane E

The radial plots for the forward-facing steps in plane E show more consistency compared to the backward-facing step.

Mach numbers visible in Figure 9.8g show an initial decrease in Mach number at the near hub region and a constant increase from 10% channel height to the shroud for increasing step height.

The total pressure coefficient also shows a decrease from 0-10% channel height and an increase from 10-20% channel height. From 20-100% channel height the total pressure coefficient of the shifted simulations coincides with the basic setup.

The temperatures visible in Figure 9.8c and Figure 9.8d show a decrease in the near-hub region and increases at 10% channel height. The static temperatures then show a constant decrease for the rest of the channel height while the total temperatures mostly coincide with the basic setup. Clear trends are visible for the static temperatures.

Figure 9.8b shows the isentropic efficiencies and they suggest an increase in the near hub region. From 5-25% channel height a decrease in efficiency is noticeable and for the remaining channel they mostly coincide with slight trends, except above 80% channel height an increase in efficiency is again visible.

The pitch angle visible in Figure 9.8e shows a decrease from the hub to 5% channel height. From 5-15% channel height the pitch angle increases up to 10 degrees. Up to 80% channel height a pitch angle decrease of around 1.5 degrees is visible.

The yaw angle visible in Figure 9.8f shows similarities between the shifted and basic setup. All simulations show two local maxima and one local minimum in the near-hub region. These maxima and minima are shifted to the hub for the shifted setup. Consequently, the yaw angles increase up to 10 degrees at 5% channel height. For the rest of the channel a constant decrease of yaw angle of around 1-2 degrees is visible except for a coinciding region at 20% channel height. At 10% channel height the decrease amounts to 5 degrees.

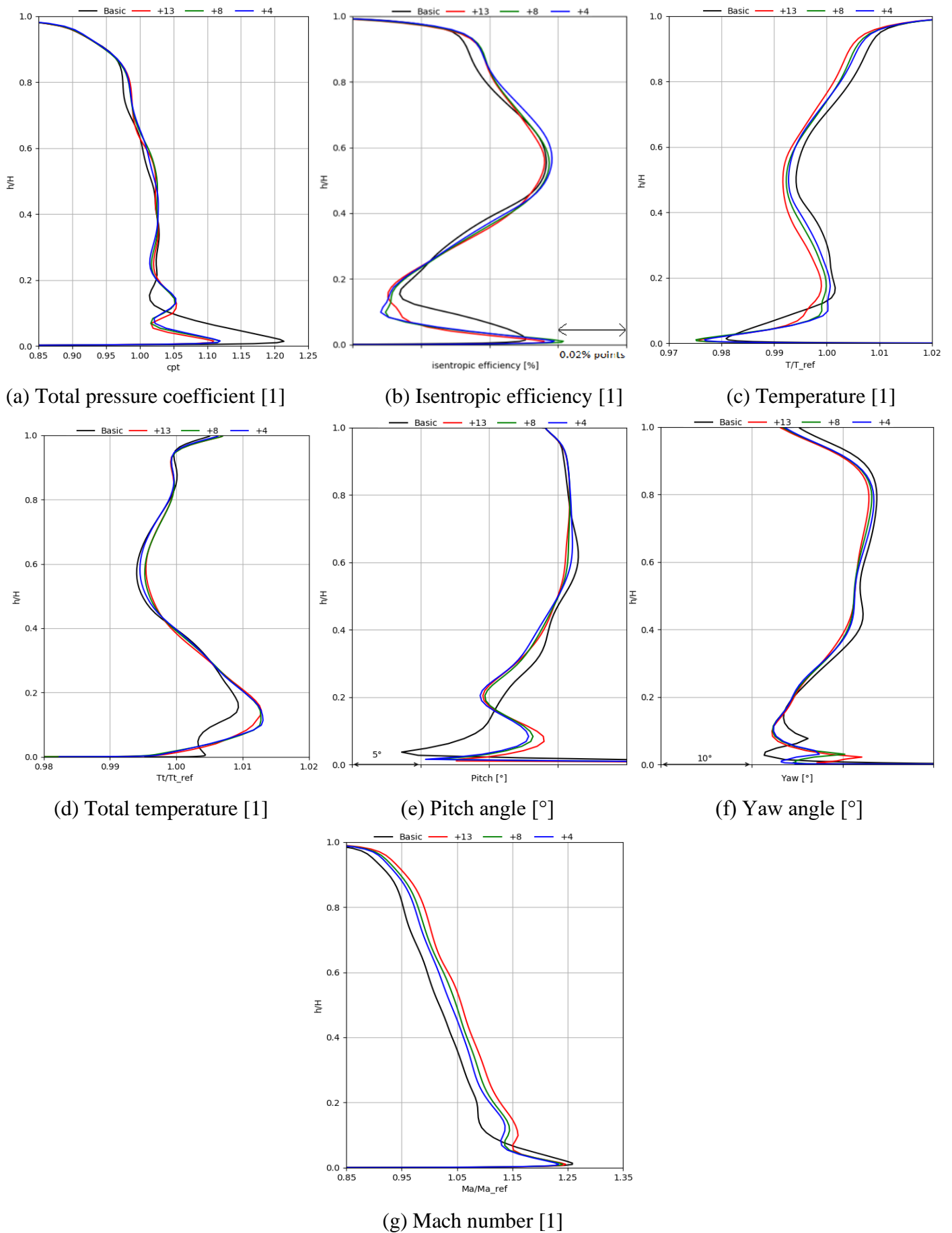


Figure 9.8: Mass and area averaged plots for forward-facing step in plane E

9.5 Separation zones

In this chapter the shape and size of the separation zones before and after the step will be discussed. The contour plots in this chapter were done at the second cell of the hub.

9.5.1 Shape and secondary vortices

In Figure 9.9 the separation zones are visible in blue for all forward-facing steps. With increasing step height, the separation length increases. The 1.3mm forward-facing step visible in Figure 9.9a precedes a separation zone which covers the channel circumferentially entirely. Within the separation zone reattachment occurs in three different locations of different size, one main large reattachment zone and two smaller ones. The reattachment is the result of a vortex which counterrotates to the main separation vortex. This can be seen more clearly in Figure 9.15. In this figure the vortex responsible for the separation can be seen in red. The second vortex in blue is created to counter the main vortex and is responsible for the smaller reattachment zone. Lastly this second vortex (blue) will wrap itself around the main vortex (red). The 0.8 and 0.4 mm forward-facing step visible in Figure 9.9b and Figure 9.9c present zones downstream which are free of separation. The separation zone size is smaller for smaller step sizes. The secondary vortices responsible for the reattachment, visible in Figure 9.15 in blue, are not visible for the 0.4 mm forward-facing step.

The separation zones in front of the forward-facing steps are visible in Figure 9.11 as blue zones and in Figure 9.14 as green iso-surfaces. Figure 9.11 shows contour plots at the second cell from the hub with negative streamwise velocity in blue. The white zones are the O-blocks surrounding the blade and are blanked. The size of the separation zones increases with bigger step heights. All forward-facing steps have a reattached zone close to the step which is a result of a small vortex which counterrotates to the main vortex causing the separation. This main vortex is visible in Figure 9.12 and in Figure 9.14. It splits up around 50% pitch into the blue and the red vortex. The red vortex travels towards the pressure side of the blade and the blue one to the suction side. The area on the red side where they collide is free is separation.

The separation zones for the backward-facing step are visible in Figure 9.10 as blue zones and in Figure 9.13 as streamtraces. The 1.3mm step has a full separation zone with no interruptions circumferentially whereas the 0.8 and 0.4 mm steps have zones without separation. All contour

plots for all step heights show zones with reattached flow close to the step. This zone is caused by vortices rotating in opposite direction to the main separation vortex. Figure 9.16 shows the streamtraces behind the 1.3 mm backward-facing step. The main vortex responsible for the separation is visible in red. A vortex rotating in the same direction is visible in black and a cross section projection of this vortex is visible in Figure 9.13b. The vortex responsible for the reattachment is visible in blue in Figure 9.16.

9.5.2 Length of separation zone

Table 9.4: Length of separation bubbles

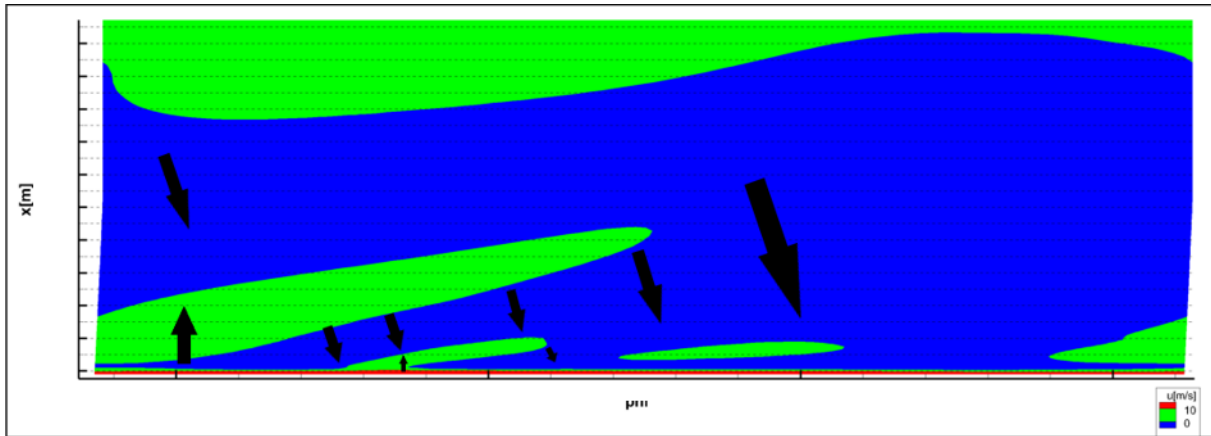
Step size	Estimated average separation length downstream [mm]	Maximum separation length [mm]	Average separation length to step height l/h [-]
+1.3mm	9mm	10mm	6.9
+0.8mm	5mm	5.5mm	6.2
+0.4mm	2mm	2.5mm	5
-1.3mm	6mm	6.5mm	4.6
-0.8mm	3mm	3.5mm	3.7
-0.4mm	2mm	2.5mm	5

The dimensionless separation length (average separation length to step height) of the separation zone for the forward-facing step is larger than the one found by similar researches. In chapter 6.1 works are mentioned where separation lengths of around 4 were found compared to 5-6.9 in separation length in this work. But there are substantial differences between the different setups which make a comparison difficult. Previous experiments had setups with parallel hub and shroud contours with decreasing effect on the dimensionless separation length. Furthermore, the steps in other works was several times larger ranging from 30 mm to 50 mm. The expansion ratio of the simulations in this work is close to 1 which decreases separation lengths compared to expansion ratios mentioned in chapter 6.1

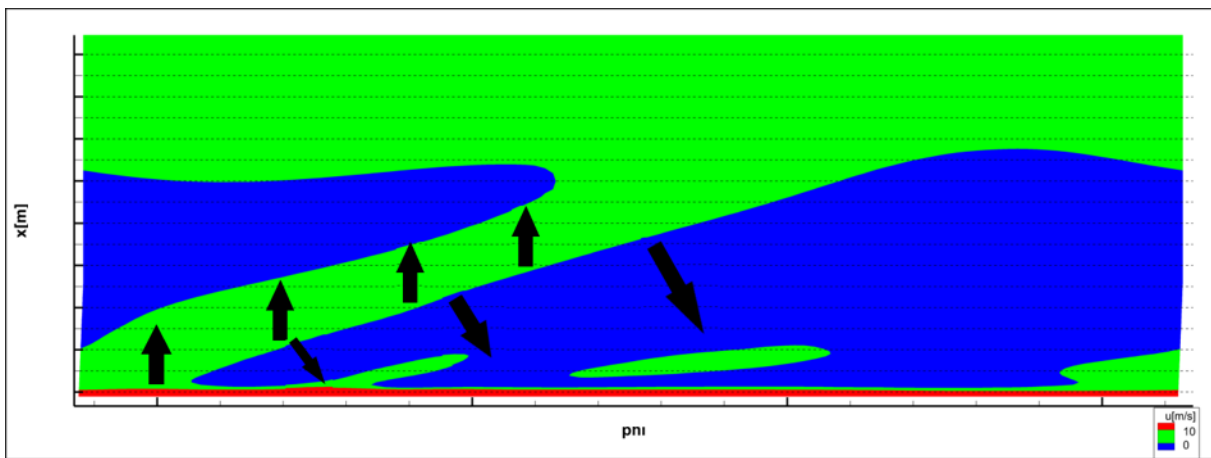
The recirculation area preceding the forward-facing step visible in Figure 9.11 has its centre at a distance to the step of about 0.5 times the step height, which is similar to the value mentioned in chapter 6. The length of the separation zone is approximately 2.5 mm for the 1.3mm forward facing step resulting in a dimensional length of 1.9. For the 0.8mm forward-facing step the separation zone of 1.5 mm results also in a dimensionless separation length of 1.9. For the 0.4 mm step a dimensionless separation length of 1.4 is obtained.

The length of the separation bubble for the backward facing step visible in Figure 9.10 was mostly shorter than the average value found in other papers as mentioned in chapter 6.2. The dimensionless separation length ranged from 3.7 to 5 in these simulations compared to 7 for similar experiments found. It was found that the 0.4 mm-backward-facing steps the dimensionless separation length is the highest with 5 which is similar to the one of the forward-facing step of the same height. It must be mentioned that the expansion ratio is close to 1 for these simulations and 1.5 or beyond for most other research papers and experiments found.

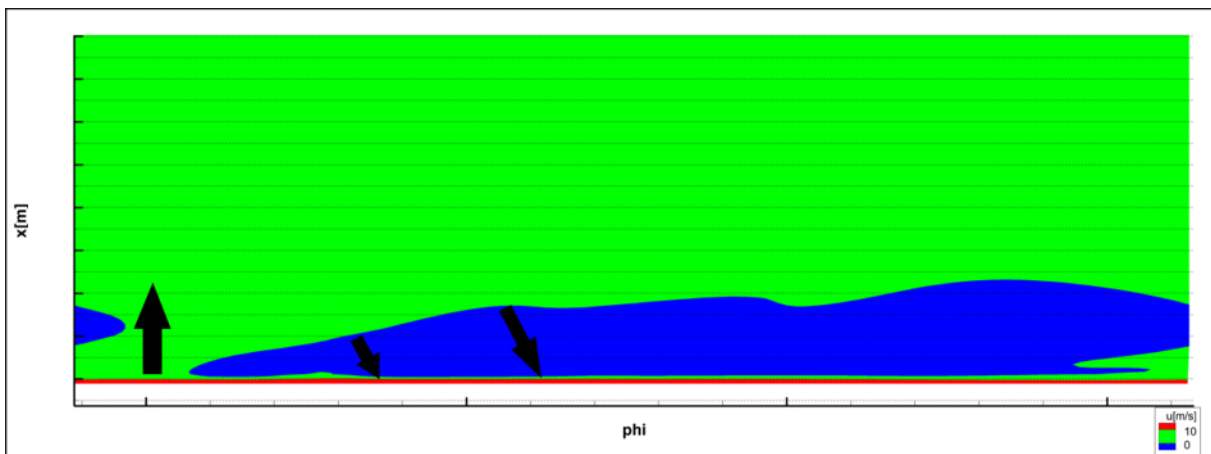
In the appendix Figures A.8 and A.9 show contour plots of negative streamwise velocity on the second cell from the hub. Negative values are displayed in blue. Furthermore, these plots contain isobars of static pressure. Recirculation mainly occurs in low static pressure zones, mainly behind the suction side of the rotor blades, where the highest velocities occur.



(a) 1.3mm forward-facing step

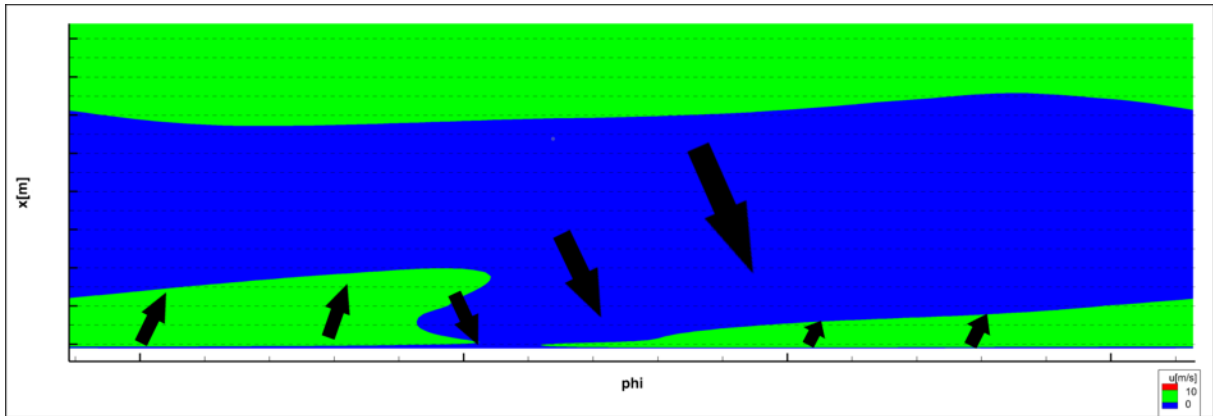


(b) 0.8mm forward-facing step

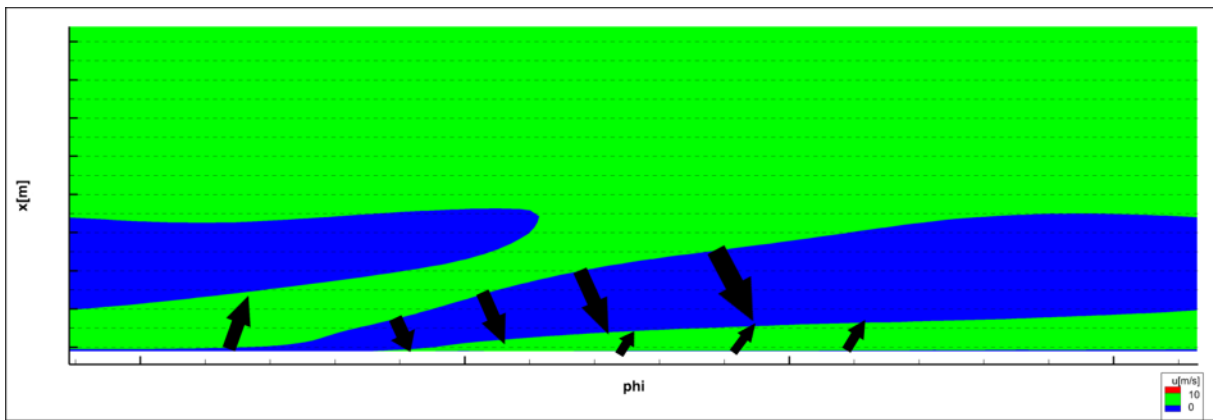


(c) 0.4mm forward-facing step

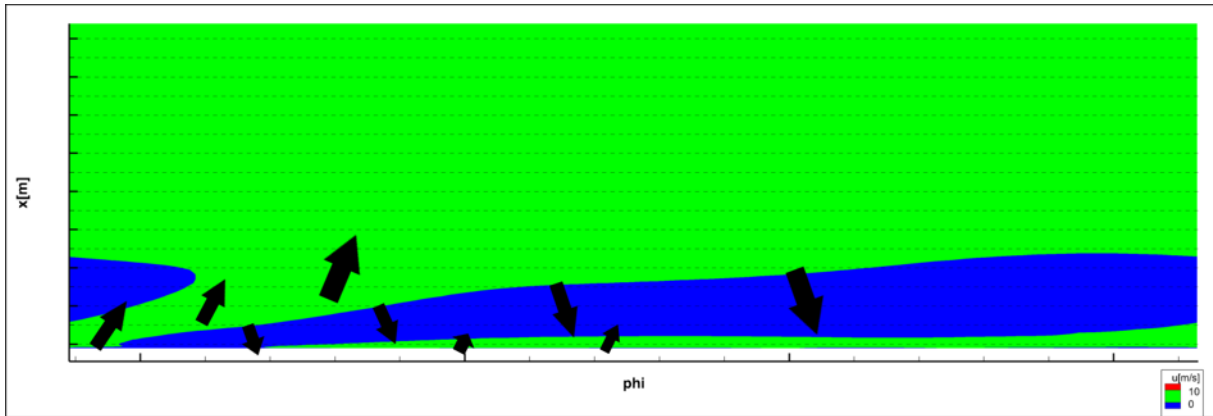
Figure 9.9: Axial velocity contour plot of the recirculation bubble after the forward-facing step at the second cell from the hub. Blue are zones affected by back-flows and the arrows indicate the approximate flow direction in that plane at that position.



(a) 1.3mm backward-facing step

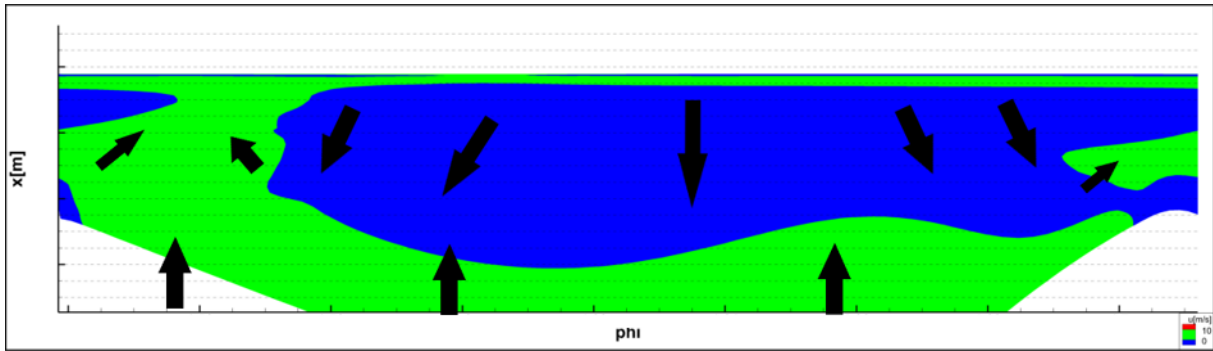


(b) 0.8mm backward-facing step

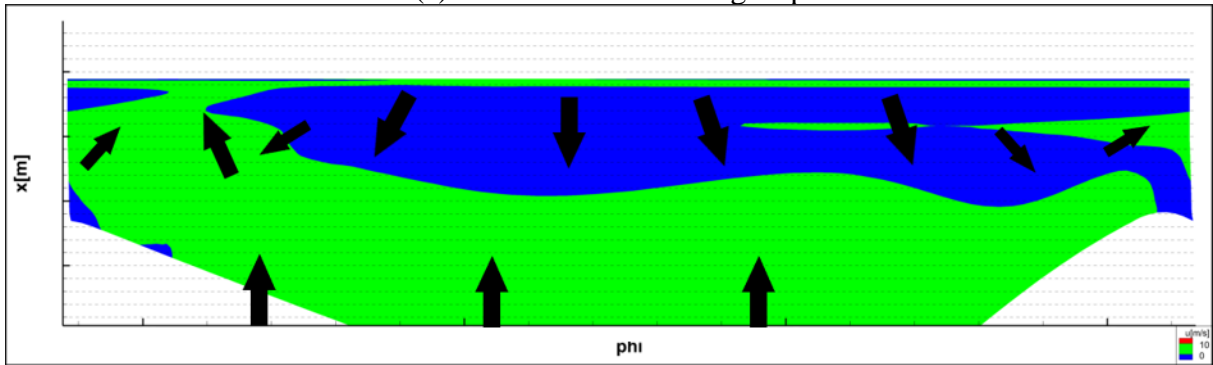


(c) 0.4mm backward-facing step

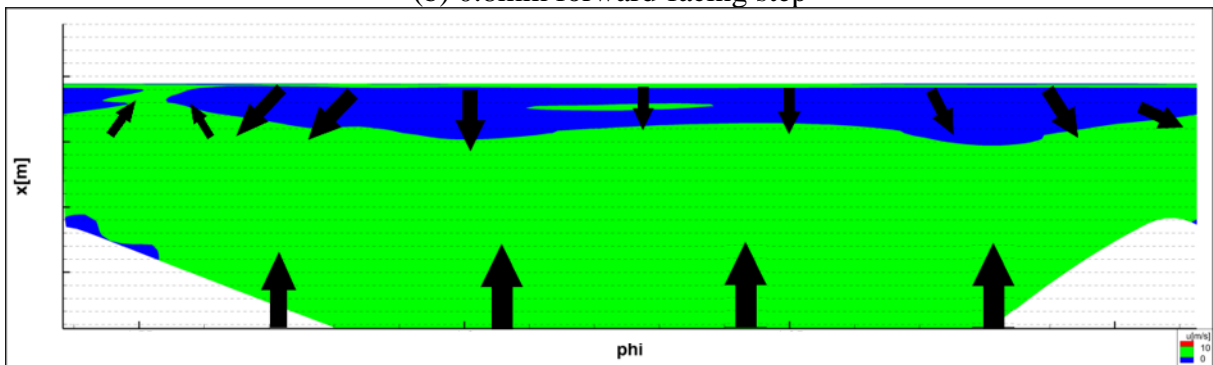
Figure 9.10: Axial velocity contour plot of the recirculation zone after the backward-facing step at the second cell from the hub. Blue are zones affected by back-flows and the arrows indicate the approximate flow direction in that plane at that position.



(a) 1.3mm forward-facing step



(b) 0.8mm forward-facing step

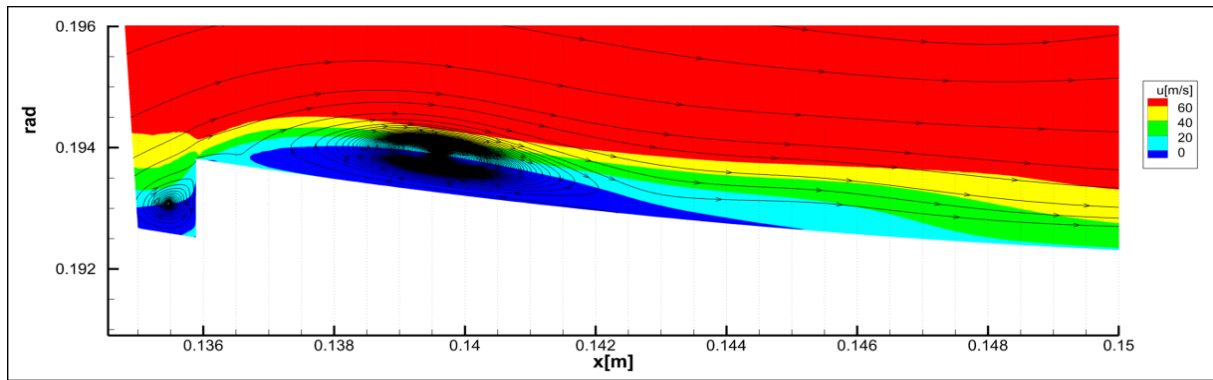


(c) 0.4mm forward-facing step

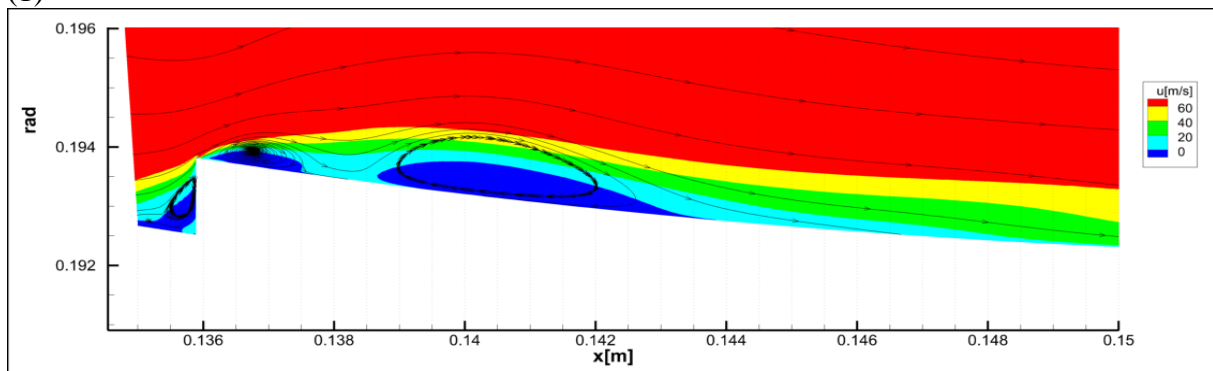
Figure 9.11: Axial velocity contour plot of the recirculation zone preceding the forward-facing step at the second cell from the hub. Blue are zones affected by back-flows and the arrows indicate the approximate flow direction in that plane at that position.

9.5.3 Axial contour plots of separation bubble

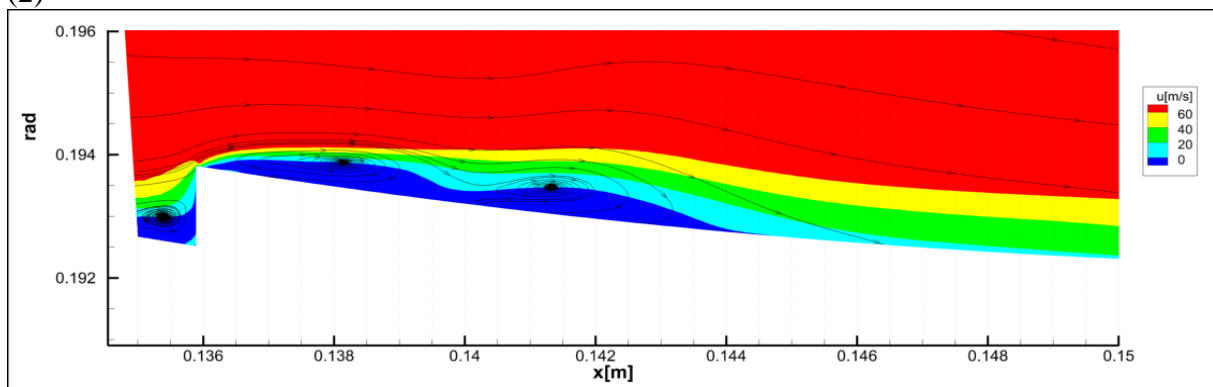
In Figure 9.12 and Figure 9.13 cross sections of the recirculation zone are visible with streamtraces projected into each plane. Secondary vortex cores apart from the main vortex are visible in both setups. It can be noted that at step heights of 0.4 mm no secondary vortex cores are visible anymore. Plots of the remaining cross sections are visible in the appendix in Figure A.4 to Figure A.7.



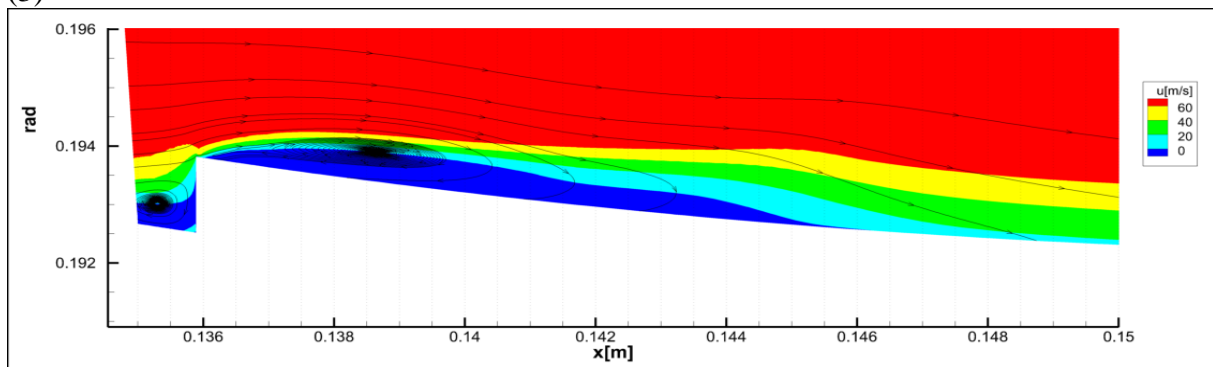
(1)



(2)

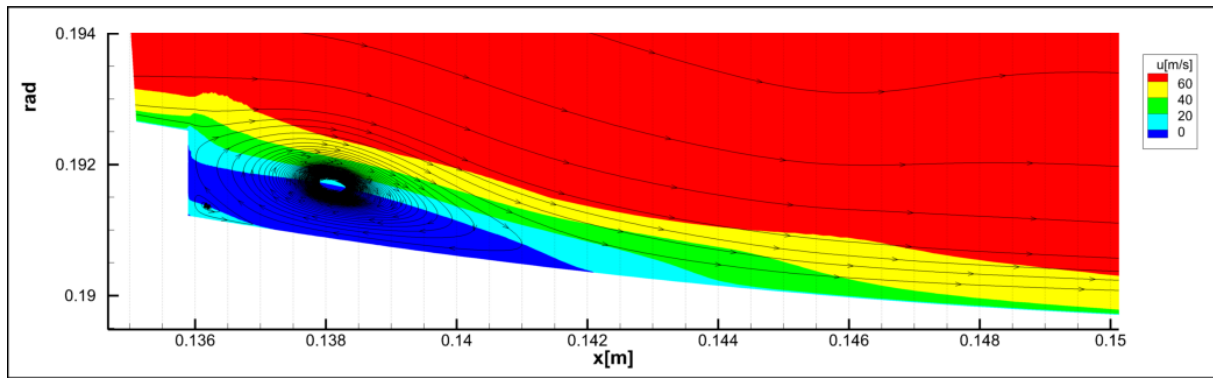


(3)

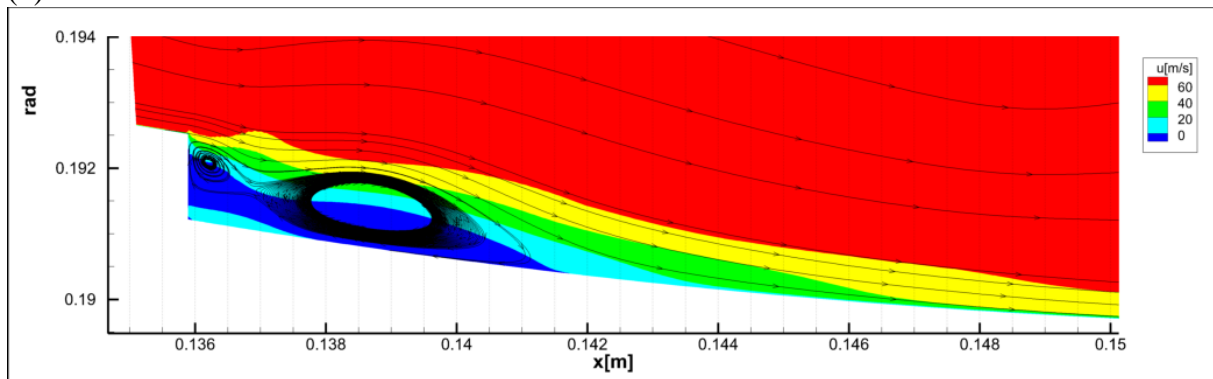


(4)

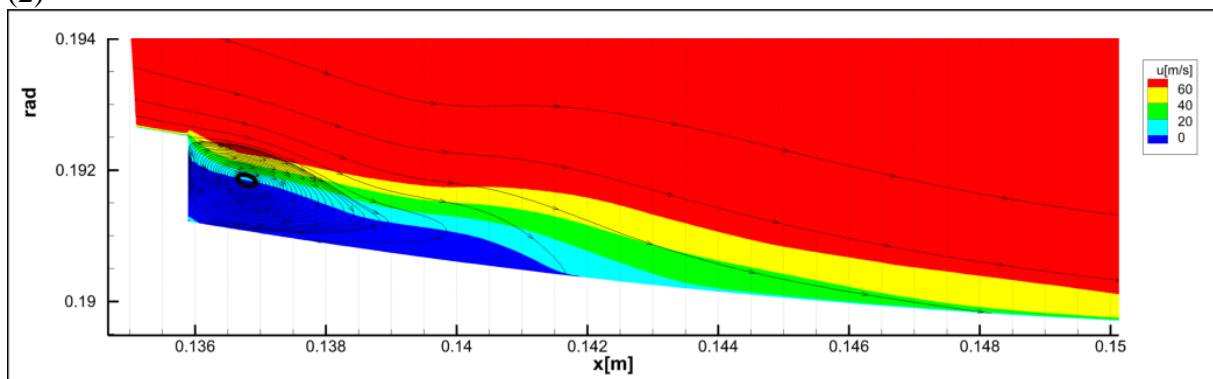
Figure 9.12: Axial cross section of the recirculation flows projected at different circumferential positions of the 1.3mm forward-facing step. Blue means negative axial velocity.



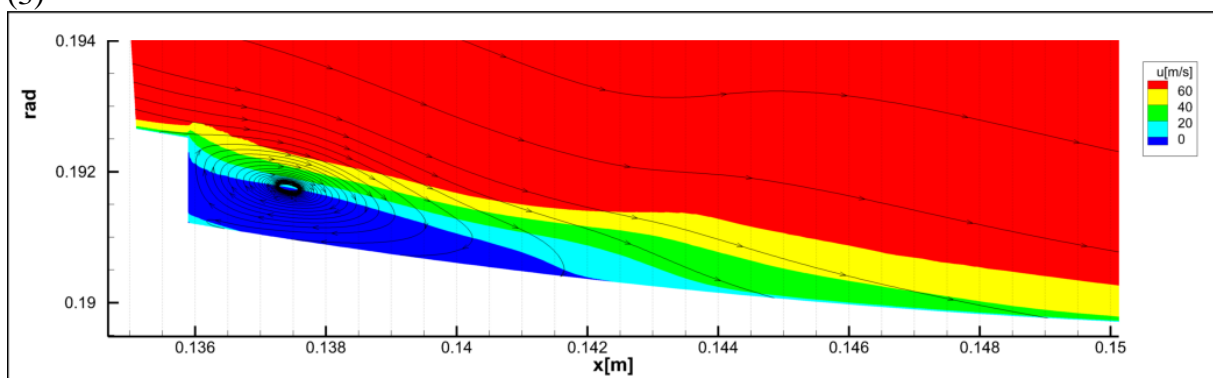
(1)



(2)



(3)



(4)

Figure 9.13: Axial cross section of the recirculation flows projected at different circumferential positions of the 1.3mm backward-facing step. Blue means negative axial velocity.

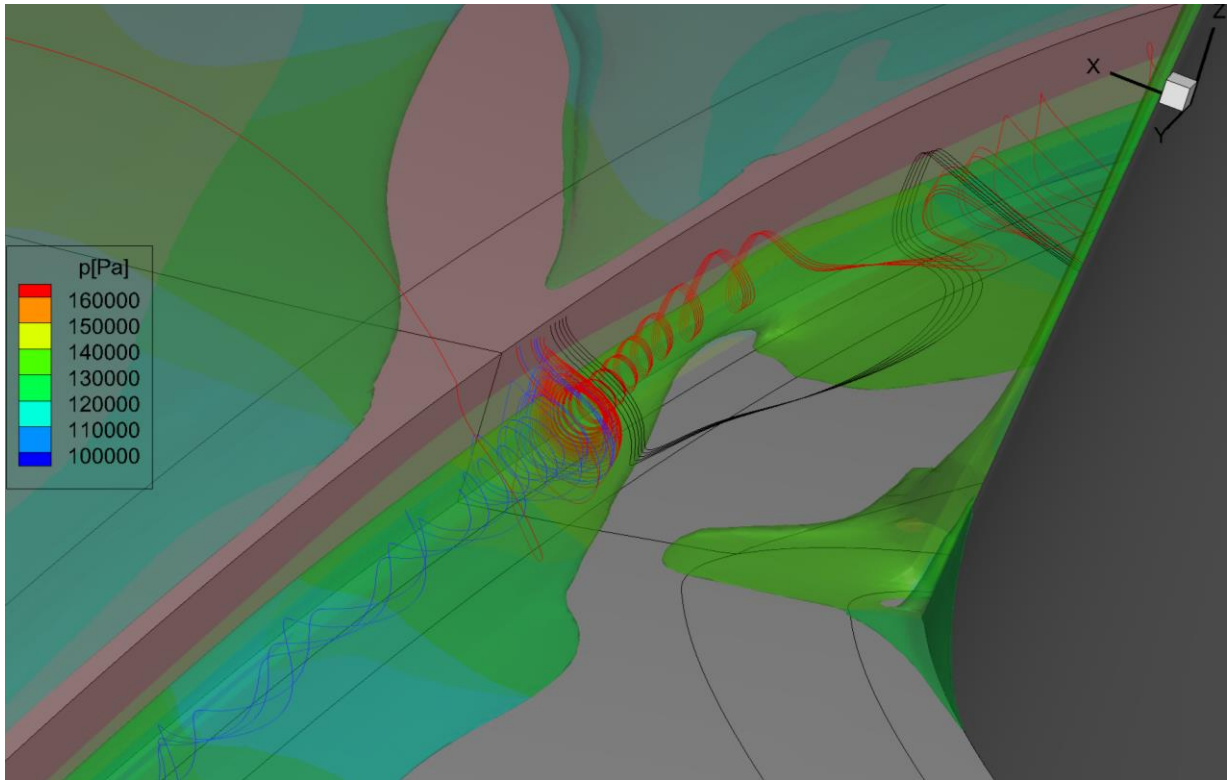


Figure 9.14: Streamtraces in front of the forward-facing step of 1.3 mm and iso-surfaces representing separation zones with negative axial velocity

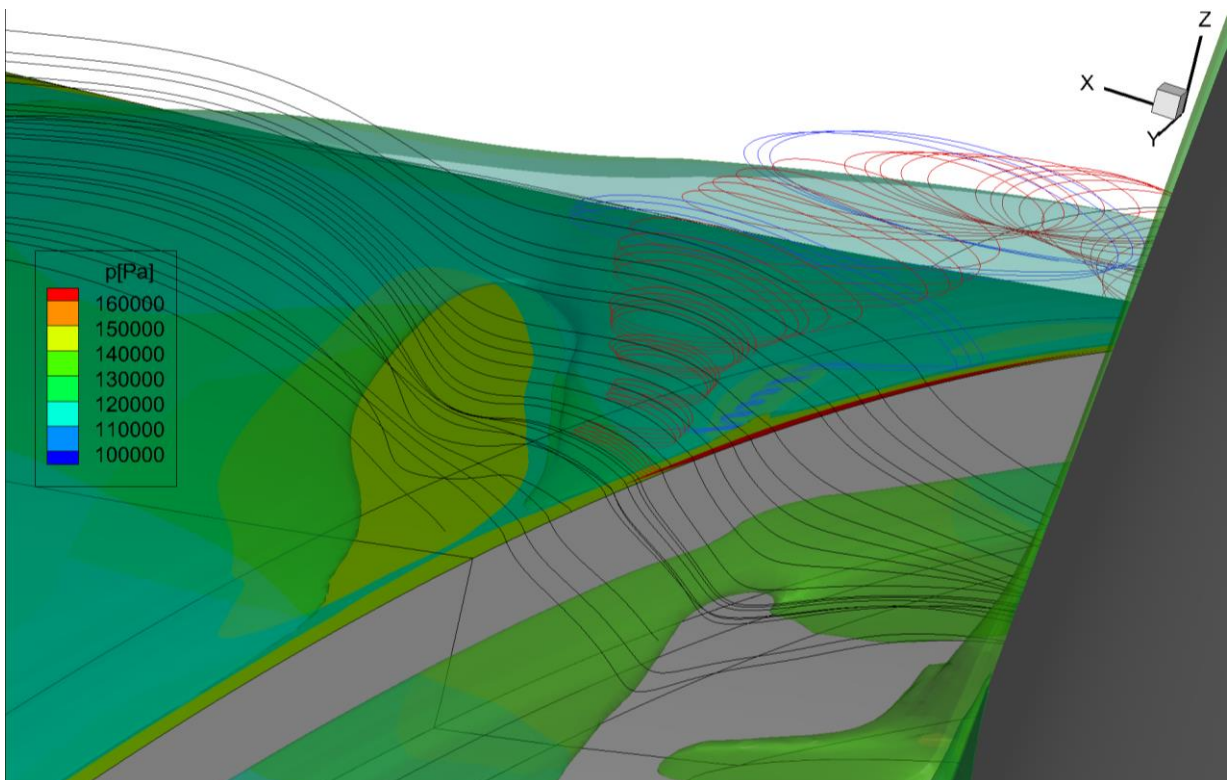


Figure 9.15: Streamtraces after the forward-facing step of 1.3 mm and iso-surfaces representing separation zones with negative streamwise velocity

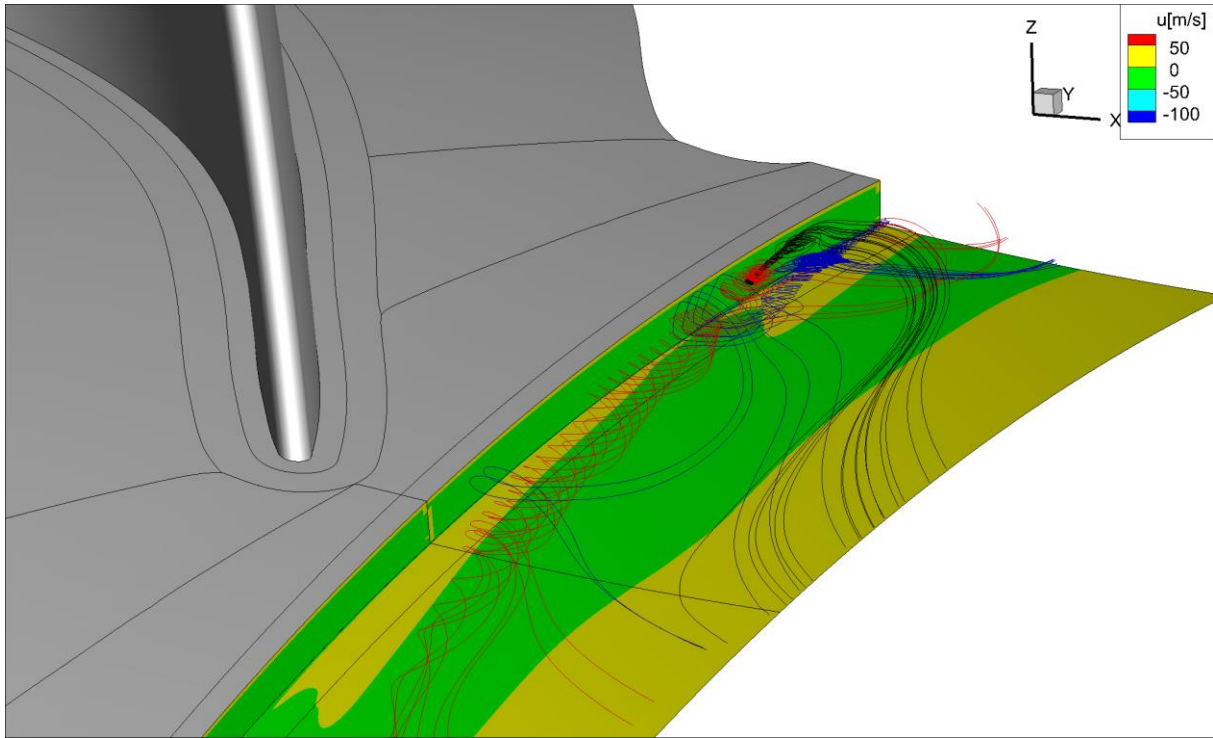
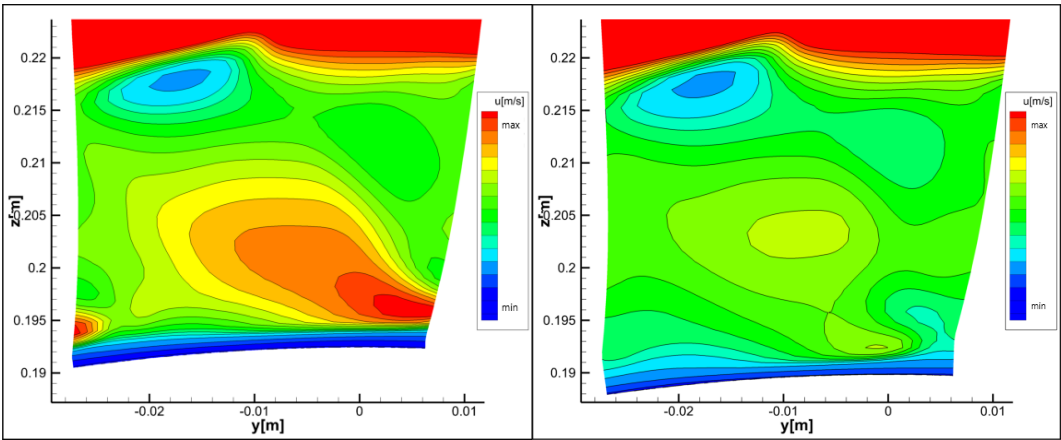


Figure 9.16: Streamtraces in front of the backward-facing step of 1.3 mm and contour plot of negative streamwise velocity on the second cell from the hub

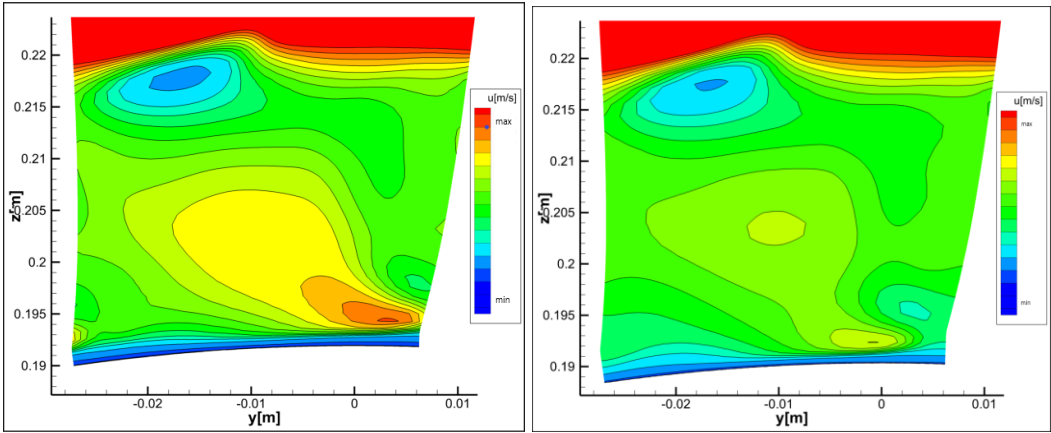
9.6 Further examination of plane C

Figure 9.17 show axial velocity contour plots for the lower channel part in plane C. It is noticeable that the velocity field remains largely unchanged above 50% channel height. The higher-velocity area in the bottom right corner experiences a significant increase with the forward-facing step. Both 0.4 mm steps have a similar low velocity area close to the hub. With increasing step height this low velocity area becomes bigger for the forward-facing step. Overall the biggest changes can be seen for the forward-facing step.



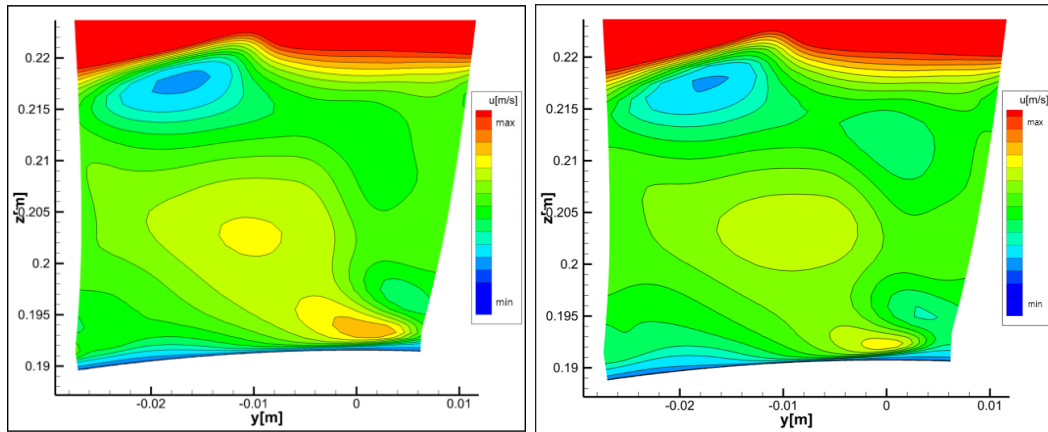
(a) 1.3mm forward-facing step

(b) 1.3mm backward-facing step



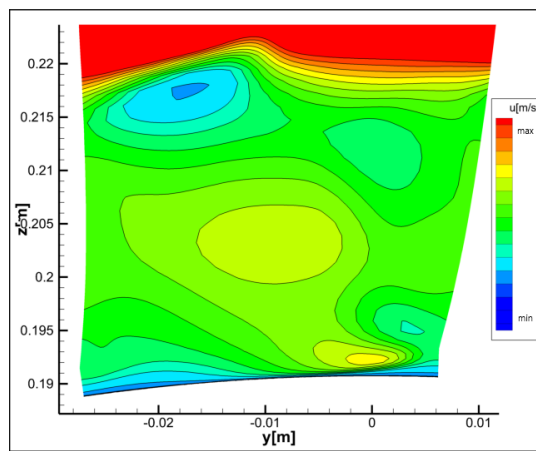
(c) 0.8mm forward-facing step

(d) 0.8mm backward-facing step



(e) 0.4mm forward-facing step

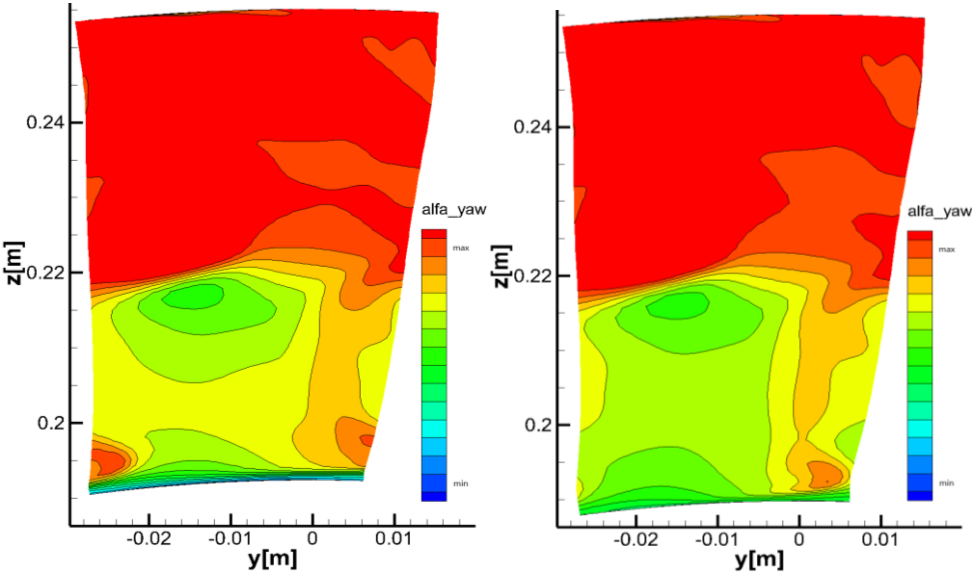
(f) 0.4mm backward-facing step



(g) basic setup

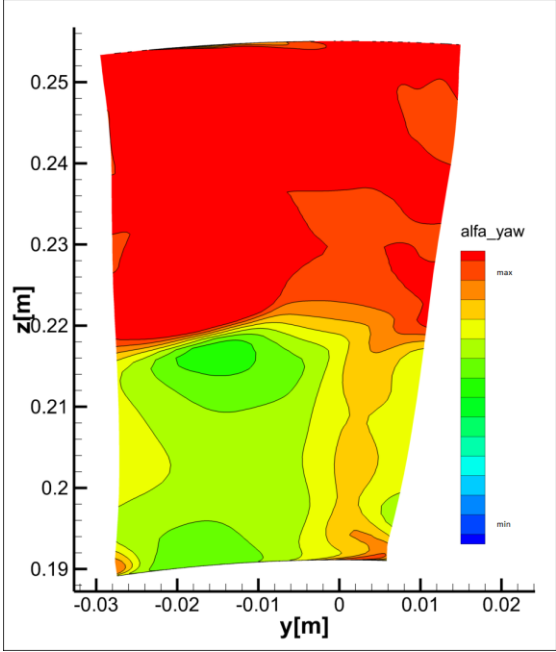
Figure 9.17: Velocity contour plots for the lower channel half in plane C

Figure 9.18 shows the yaw angle in plane C for the 1.3 mm forward-facing step, the 1.3 mm backward-facing step and the basic setup. The yaw angles were affected most by the steps as seen in chapter 9.3. The separation zone caused by the step in the flow path prevents the flow to be correctly guided. This affects the flow up to 15% channel height and subsequently influences the flow onto the MTF. In the following detailed contour plots of the yaw angle in plane C1 and plane C are shown.



(a) 1.3mm forward-facing step

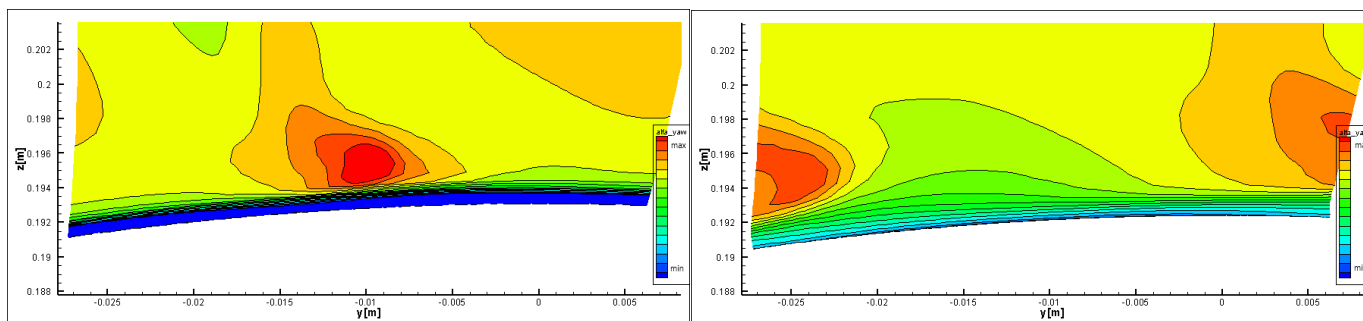
(b) 1.3mm backward-facing step



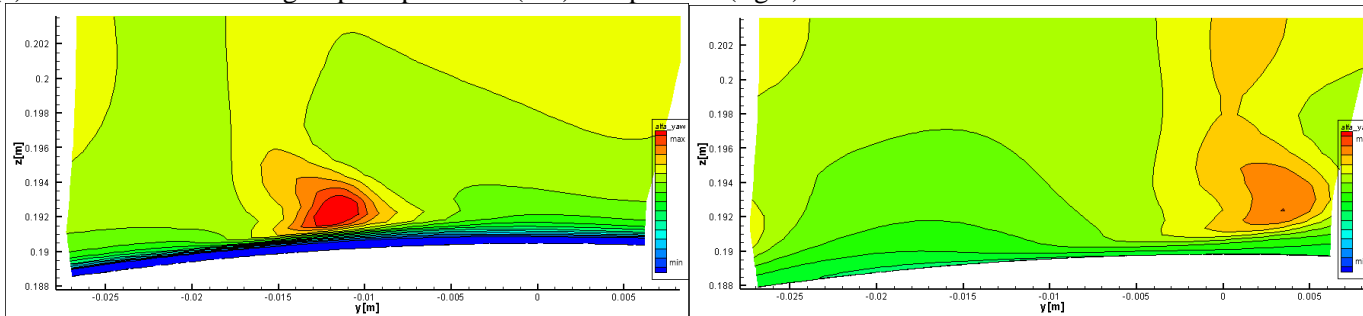
(c) basic setup

Figure 9.18: Yaw angle in plane C for maximum step heights and basic setup

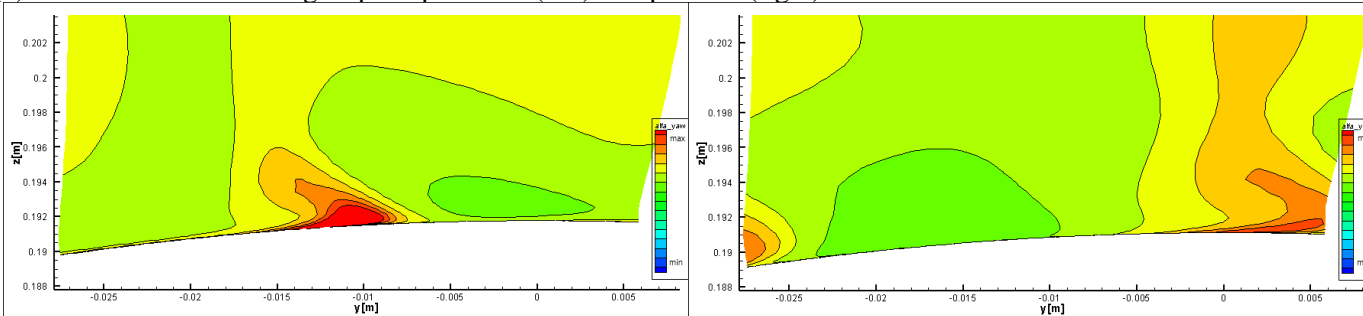
In Figure 9.19 detailed plots of the yaw angles in plane C1(left) and plane C(right) close to the hub can be seen. The higher yaw angles in the hot spot coincide with higher streamwise vorticity and higher axial velocity behind the trailing edge of the rotor. The red zone visible in Figure 9.19 stems from the corner vortex at the trailing edge of the rotor. The zone of high yaw angle increases with the step and especially for the forward-facing step the yaw angle distribution differs remarkably from the base case, also in the more downstream plane C.



(a) 1.3mm forward-facing step for plane C1 (left) and plane C (right)



(b) 1.3mm backward facing step for plane C1 (left) and plane C (right)

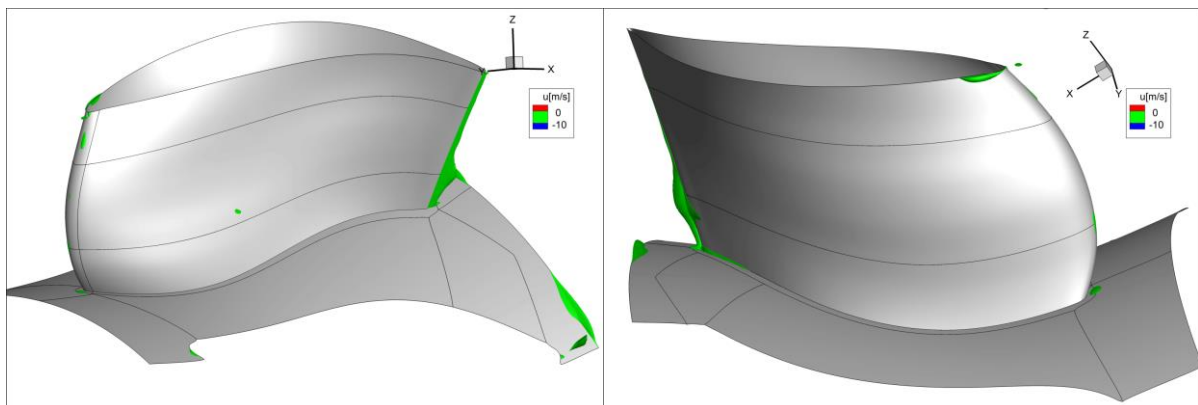


(c) BASIC setup for plane C1 (left) and plane C (right)

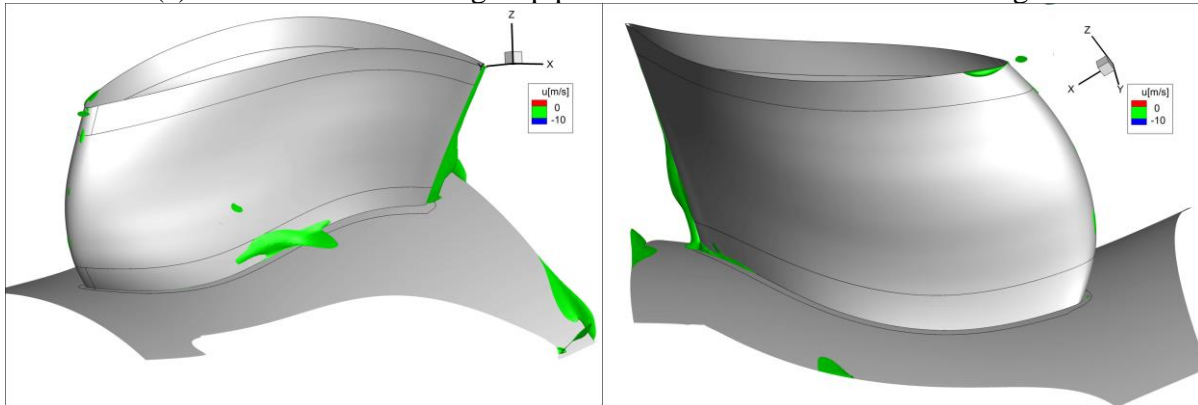
Figure 9.19: Detailed view of the yaw angles in plane C1 and plane C

9.7 Further examinations

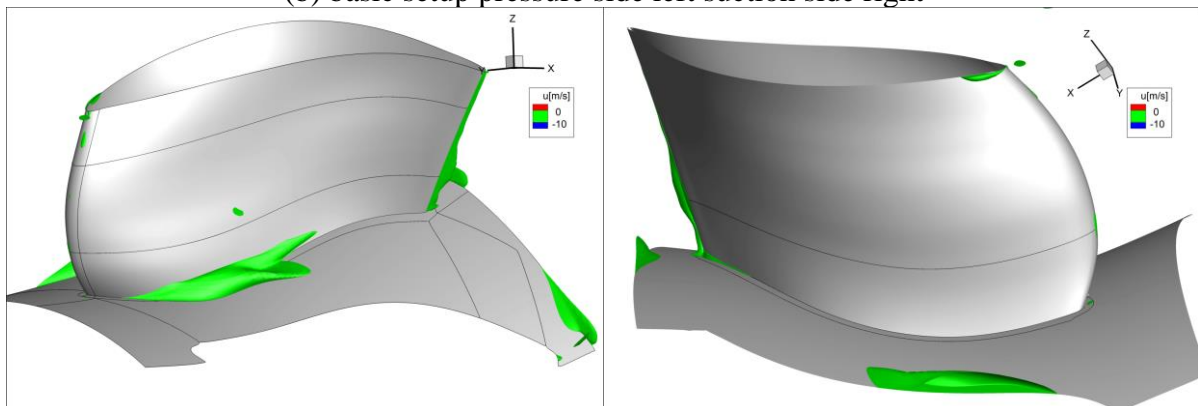
A possible explanation for the variations in yaw and pitch angles for the backward-facing step in plane E was found in the flow through the MTF. It was discovered that a separation zone at the pressure side of the MTF increases with the height of the backward-facing step, whereas the separation is reduced for the forward-facing step compared to the base case (see Figure 9.20). This increased separation could be the explanation to the inconsistency of the radial mass averaged plots for plane E. A cause of the separation zones could be the different inflow angles to the MTF struts or the change in Mach number at the hub region.



(a) 1.3mm forward-facing step pressure side left and suction side right



(b) basic setup pressure side left suction side right



(a) 1.3mm backward-facing step pressure side left and suction side right

Figure 9.20: Illustration of separation zones with iso-surface of zero axial velocity

This increased separation could be the explanation to the inconsistency of the radial mass averaged plots for plane E. A cause of the separation zones could be the different inflow angles to the MTF struts or the change in Mach number at the hub region. The separation areas are visible in Figure 9.20: Illustration of separation zones with iso-surface of zero axial velocity as iso surfaces in green. It is clearly visible that size of the separation area is getting bigger for the backward-facing step and smaller for the forward-facing step. Examinations of the other step heights confirmed this trend.

10. Conclusions

In this work the influence of forward-facing or backward-facing steps in the inner casing of an aeroengine turbine was investigated numerically the step is located between the HP rotor and the succeeding MTF. The simulations show that there is or can be a loss of efficiency due to the disturbances caused by the step in the channel. The efficiency loss is small. It is interesting that a backward-facing step of small magnitude, up to around 0.8 mm has a greater or similar effect on the total pressure loss than a forward-facing step of the same height. The differences are truly small and must be interpreted carefully. Small variations in mass flow of already 0,01 percent can affect the results. The difference in yaw angles caused by the step has already been mentioned by Bauinger and were confirmed in this work. The change in Mach number and in the yaw angles at the hub affect the MTF flow, especially the separation zones at the MTF strut pressure side.

In order to get more insight and to draw a more conclusive result, a transient simulation should be made. The mixing-plane interface from the HP rotor to the strut smear out the influence of the steps in circumferential direction. A step on the outer casing could not be simulated since it causes separation zones which extend further than the already downstream-shifted interface. This far stretched separation region at the shroud is most likely aggravated by the shortened and thus more aggressive duct for weight reasons. Therefore, in times where aeroengines should be built lighter this could potentially affect a turbines efficiency negatively.

11. Appendix

11.1 Prospect

Due to the ratio of the different pitches a total circumferential section of 90° would be needed for an unsteady simulation which would result in a cell amount of roughly 70 million. In order to reduce the required computational power and time needed, the MTF was resized maintaining the ratio between pitch and chord length thus allowing a smaller circumferential section. This was done by transforming the Cartesian coordinates of the different blade cuts into polar coordinates, then multiplying the streamwise X Coordinate and the polar coordinate angle with the factor which resulted from the pitch reduction from 22.5° to 15° . Since the blade cuts were not of constant radius the reduction of the axial component resulted in a distortion of the blade, visible in Figure A.1 as the green line. Subsequently, the reduced axial component was shifted along the axis in order to align the blade leading edge at approximately the same axial position, visible in Figure A.1 as the blue line. The shifted profile was then projected radially on the original section (red line). The resulting blade profiles can be seen in Figure A.2 and Figure A.3

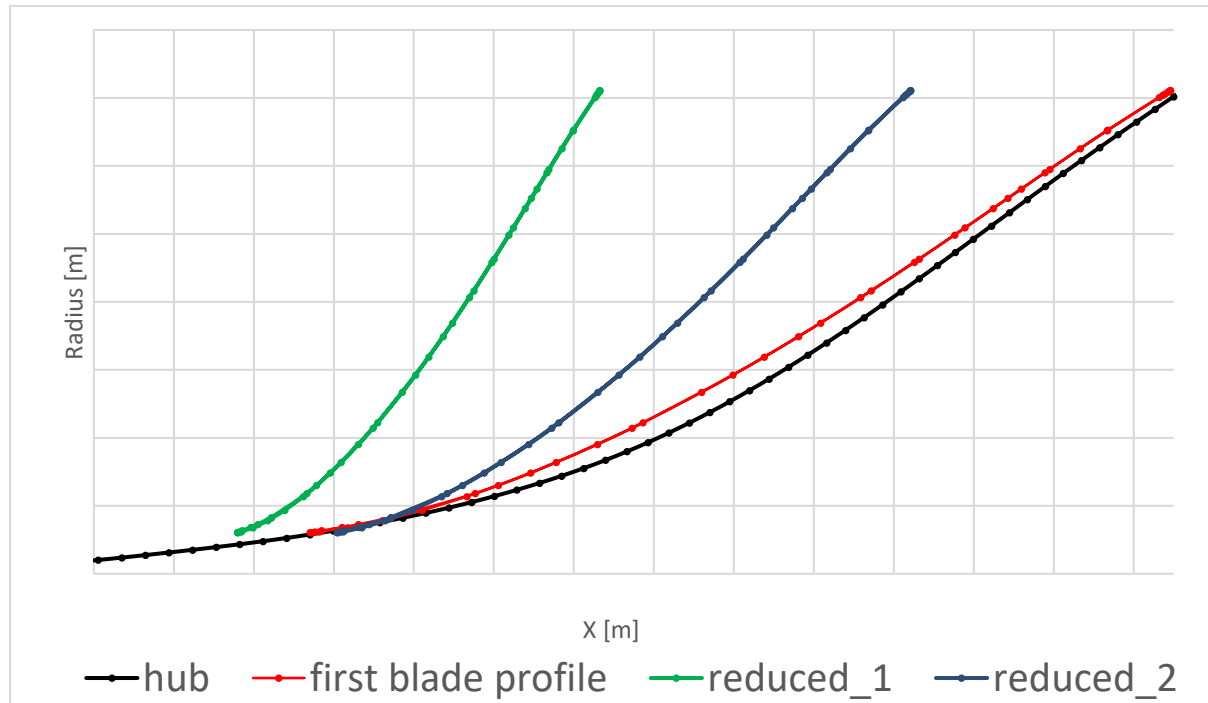


Figure A.1: Scheme of reduction process

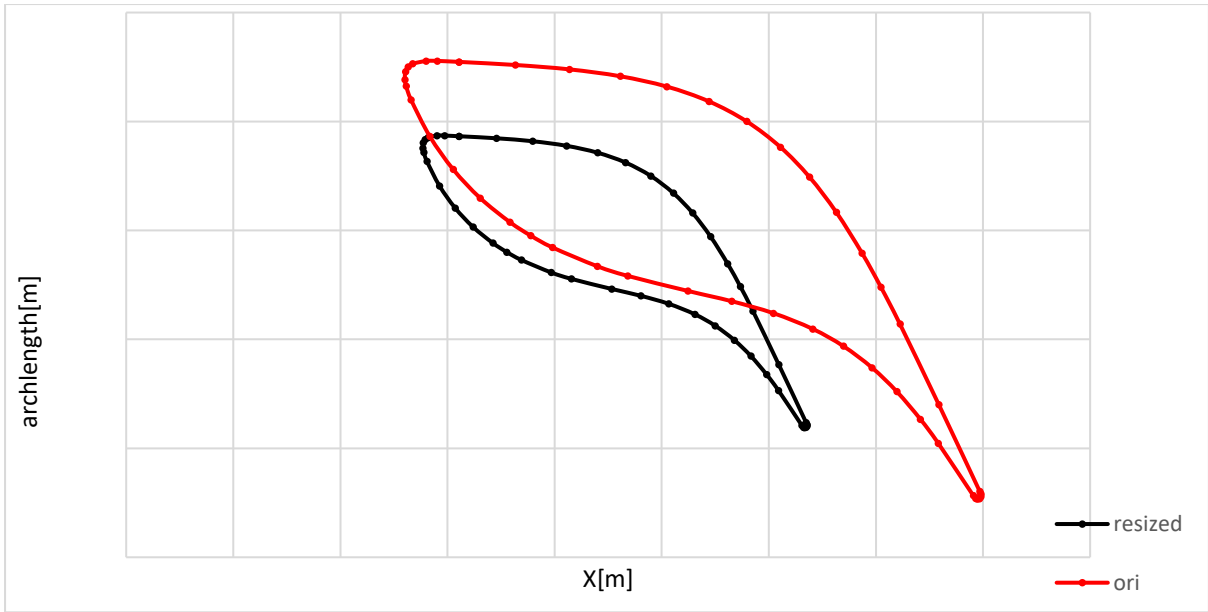


Figure A.2: Resized blade

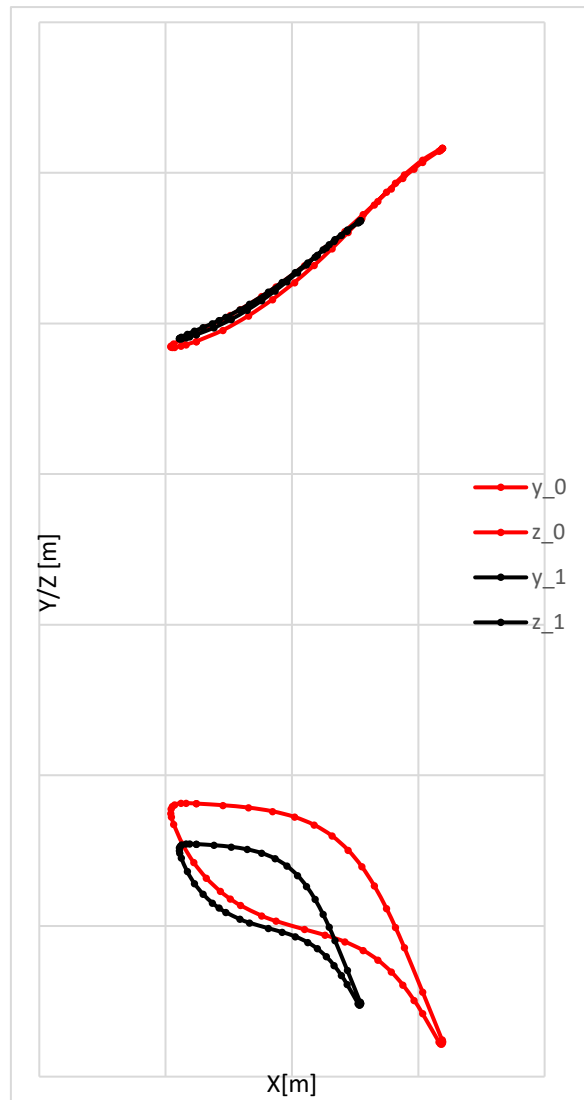


Figure A.3: Y and Z projection of resized blade

11.2 Abbreviations and acronyms

(T)MTF	(Turning) Mid Turbine Frame
TTTF	Transonic Test Turbine Facility
BFS	Backward-facing step
FFS	Forward-facing step
RANS	Reynolds-averaged Navier-Stokes-Equations
DNS	Direct numerical simulation
LES	Large eddy simulation
+13	1.3mm forward-facing step
+8	0.8mm forward-facing step
+4	0.4mm forward-facing step
-13	1.3mm backward-facing step
-8	0.8mm backward-facing step
-4	0.4mm backward-facing step

11.3 Nomenclature

\vec{v}	Velocity vector
ρ	Density
τ	Stress tensor
Q	Internal heat sources
e	Total internal energy per volume unit
t	Time
T	Temperature
k	Turbulent kinetic energy
p	static pressure
p_t	total pressure
μ	Dynamic viscosity
μ_t	Eddy viscosity
δ_{ij}	Kronecker delta
ε	Dissipation
ω	Specific dissipation
ν	Kinematic viscosity
κ	Isentropic coefficient
c_{pt}	Total pressure coefficient
y^+	Dimensionless wall distance
C_μ	Constant
$\bar{\phi}$	Time mean value

11.4 List of figures

Figure 4.1: Cartesian grid around an elliptic object [5]	9
Figure 4.2: Quadtree Octree grid around an air foil [5]	10
Figure 4.3: Body fitted grid around the first stator in the simulation	10
Figure 4.4: Unstructured Grid around an air foil [5]	11
Figure 4.5: Representation of skewness factor [6]	12
Figure 5.1: Simple model of secondary flows in blade row [7]	13
Figure 5.2: Secondary flows according to Sharma and Butler [8]	14
Figure 5.3: Secondary flows according to Olson, Goldstein and Eckert [7]	15
Figure 5.4: Secondary flows at rotor tip [9]	16
Figure 6.1: Flow phenomena at forward-facing step [10]	17
Figure 6.2: Flow at backward-facing step [12]	18
Figure 7.1: Compressor Setup [15]	19
Figure 7.2: Axial cross section of test rig [16]	20
Figure 7.3: Scheme of lateral shift [16]	22
Figure 7.4: Axial cross section of measurement planes [16]	23
Figure 8.1: AiGrids GUI	24
Figure 8.2: AiGridLinars	25
Figure 8.3 Convergence example	33
Figure 8.4: Mesh of the backward-facing step	35
Figure 8.5: Entire calculation domain	36
Figure 8.6: Axial cross section of measurement planes	38
Figure 8.7: Detailed axial cross section of measurement planes	39
Figure 8.8: Axial evaluation planes behind the rotor	39
Figure 9.1: Total pressure loss in [%] compared to plane C1	44
Figure 9.2: Total pressure loss in [%] compared to Plane C1 and relative to basic setup	44
Figure 9.3: Mass and area averaged plots for maximum step heights in plane C	47
Figure 9.4: Mass and area averaged plots for the backward facing step in plane C	49
Figure 9.5: Mass and area averaged plots for forward-facing step in plane C	51
Figure 9.6: Mass and area averaged plots for maximum step heights in plane E	54
Figure 9.7: Mass and area averaged plots for backward-facing step in plane E	56
Figure 9.8: Mass and area averaged plots for forward-facing step in plane E	58
Figure 9.9: Axial velocity contour plot of the recirculation bubble after the forward-facing step at the second cell from the hub. Blue are zones affected by back-flows and the arrows indicate the approximate flow direction in that plane at that position.	62
Figure 9.10: Axial velocity contour plot of the recirculation zone after the backward-facing step at the second cell from the hub. Blue are zones affected by back-flows and the arrows indicate the approximate flow direction in that plane at that position.	63
Figure 9.11: Axial velocity contour plot of the recirculation zone preceding the forward-facing step at the second cell from the hub. Blue are zones affected by back-flows and the arrows indicate the approximate flow direction in that plane at that position.	64
Figure 9.12: Axial cross section of the recirculation flows projected at different circumferential positions of the 1.3mm forward-facing step. Blue means negative axial velocity.	66
Figure 9.13: Axial cross section of the recirculation flows projected at different circumferential positions of the 1.3mm backward-facing step. Blue means negative axial velocity.	67
Figure 9.14: Streamtraces in front of the forward-facing step of 1.3 mm and iso-surfaces representing separation zones with negative axial velocity	68
Figure 9.15: Streamtraces after the forward-facing step of 1.3 mm and iso-surfaces representing separation zones with negative streamwise velocity	68
Figure 9.16: Streamtraces in front of the backward-facing step of 1.3 mm and contour plot of negative streamwise velocity on the second cell from the hub	69
Figure 9.17: Velocity contour plots for the lower channel half in plane C	71
Figure 9.18: Yaw angle in plane C for maximum step heights and basic setup	72
Figure 9.19: Detailed view of the yaw angles in plane C1 and plane C	73
Figure 9.20: Illustration of separation zones with iso-surface of zero axial velocity	74

11.5 List of tables

Table 7.1: Test rig blade parameters [16]	Error! Bookmark not defined.
Table 8.1: Linars settings.....	32
Table 8.2: Variation of shear stresses summarized for each block after 500 iterations for the basic simulation..	34
Table 8.3: Boundary conditions for the basic setup.....	37
Table 9.1: Differences in pressure ratio and mass flows for the simulations.....	41
Table 9.2: Total pressure losses compared to plane C1.....	42
Table 9.3: Isentropic efficiency in relation to plane A, total pressures and total temperatures.	43
Table 9.4: Length of separation bubbles.....	60

11.6 Figures

The following figures show additional result of the flow around the step.

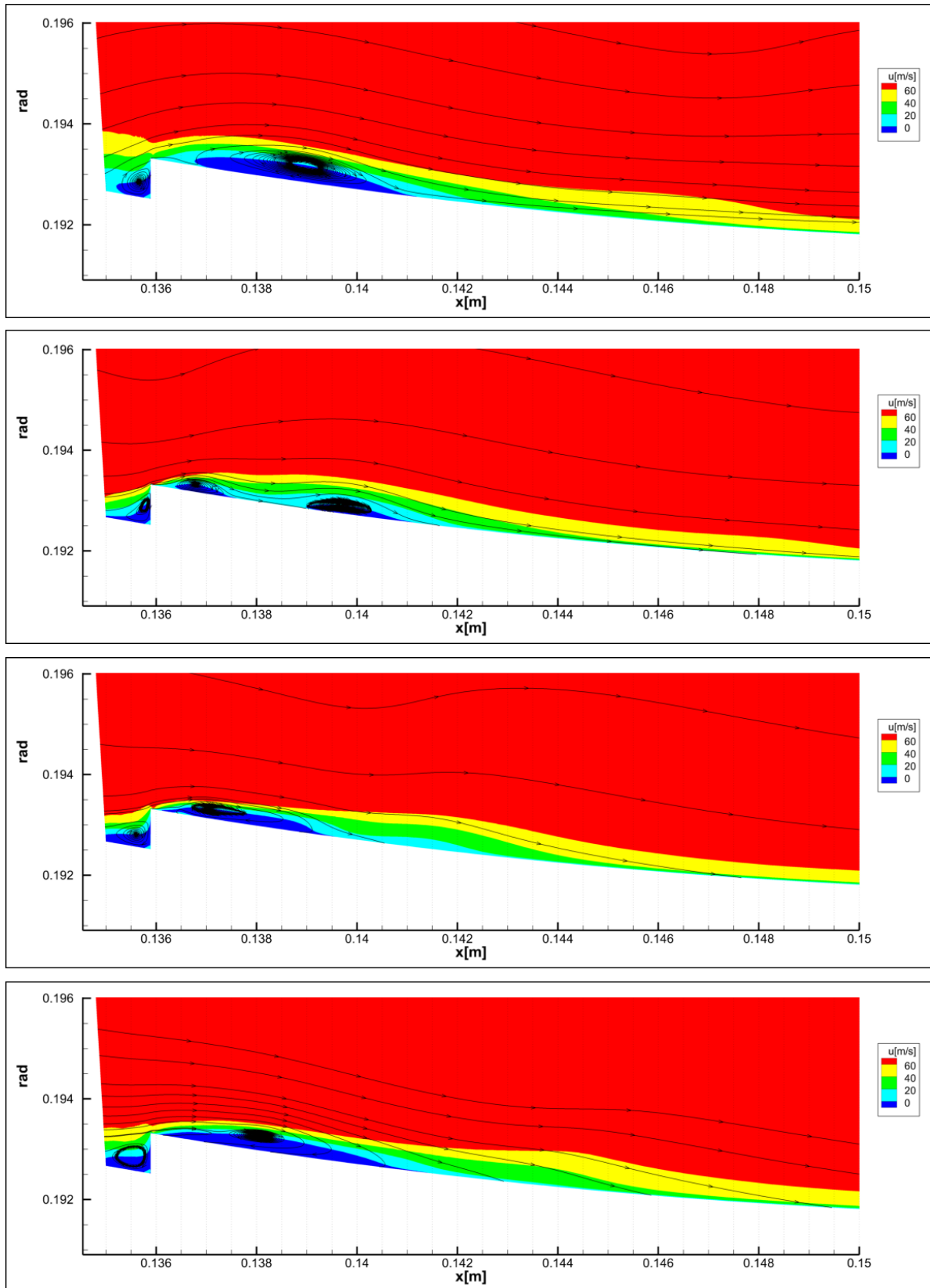


Figure A.4: Axial cross section of the recirculation flows projected at different circumferential positions of the 0.8mm forward-facing step

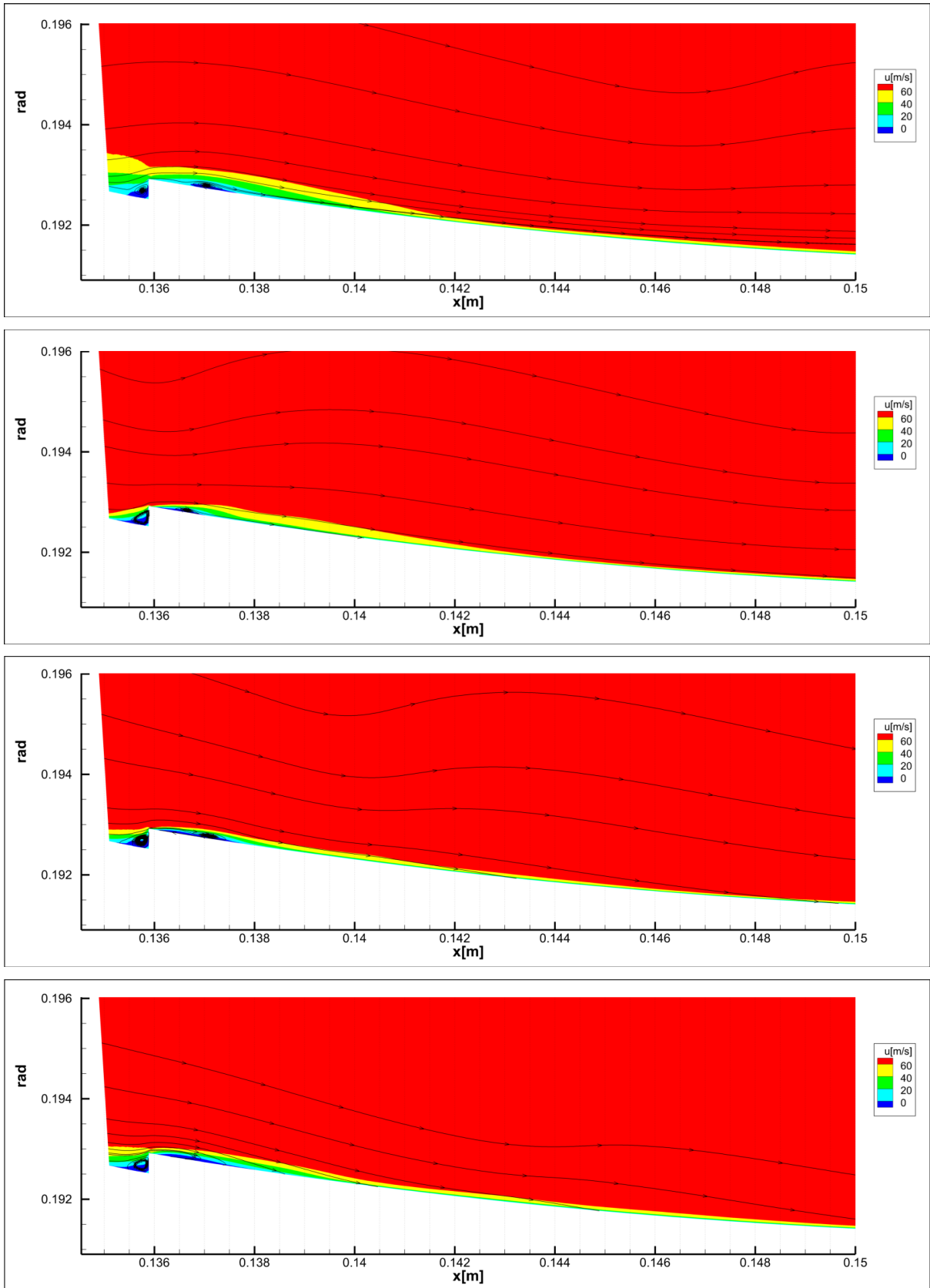


Figure A.5: Axial cross section of the recirculation flows projected at different circumferential positions of the 0.4mm forward-facing step

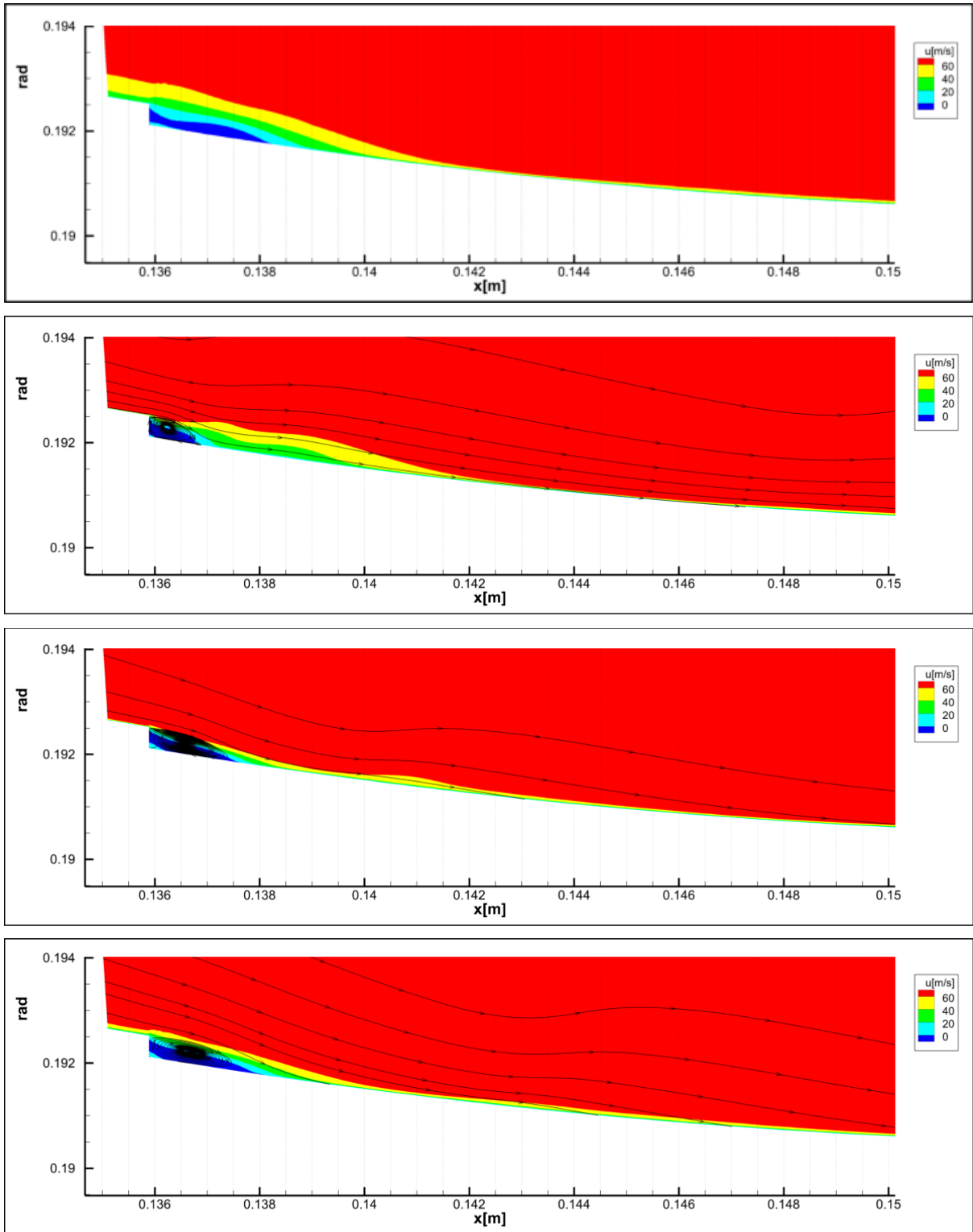


Figure A.6: Axial cross section of the recirculation flows projected at different circumferential positions of the 0.4mm backward-facing step

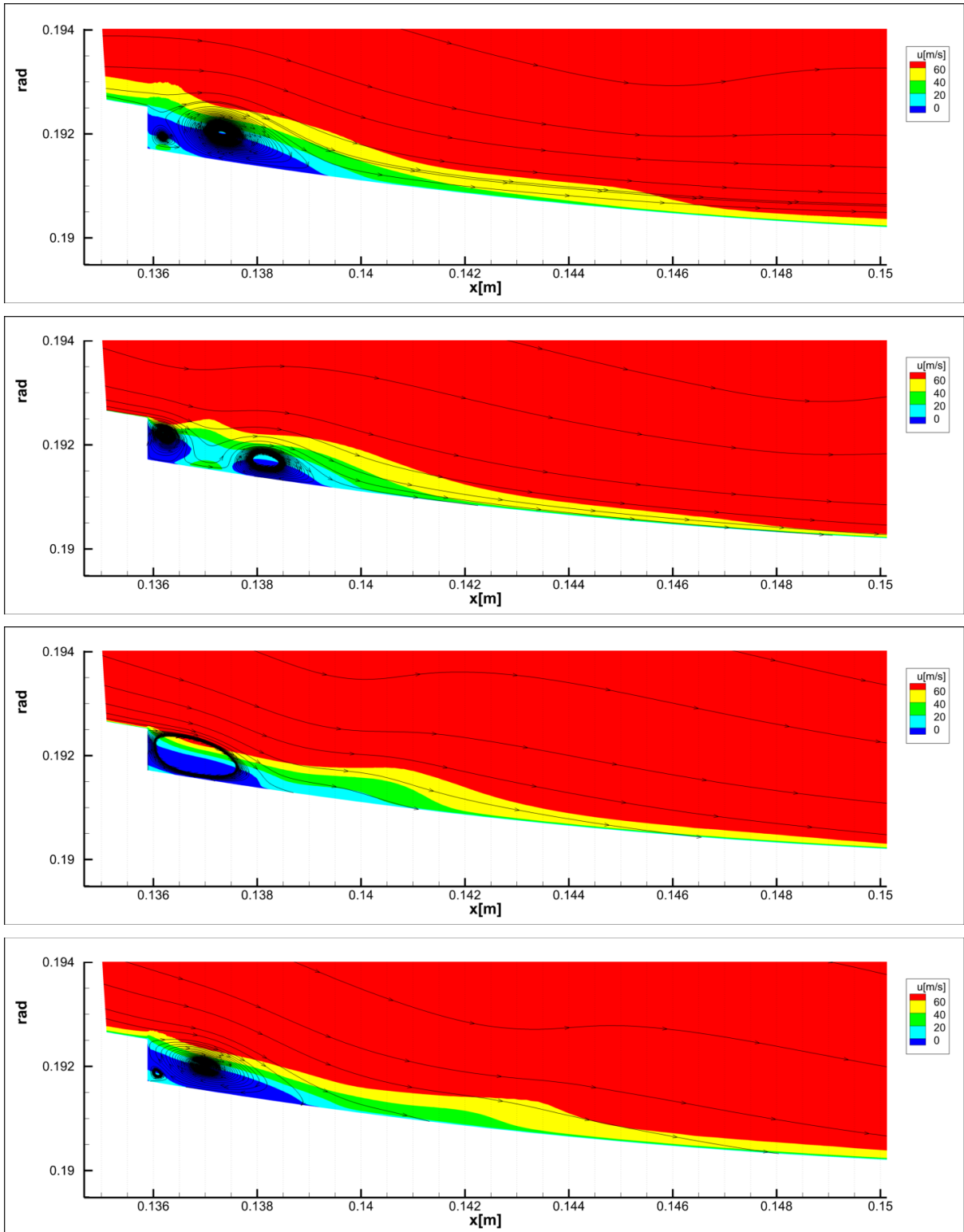


Figure A.7 Axial cross section of the recirculation flows projected at different circumferential positions of the 0.8mm backward-facing step

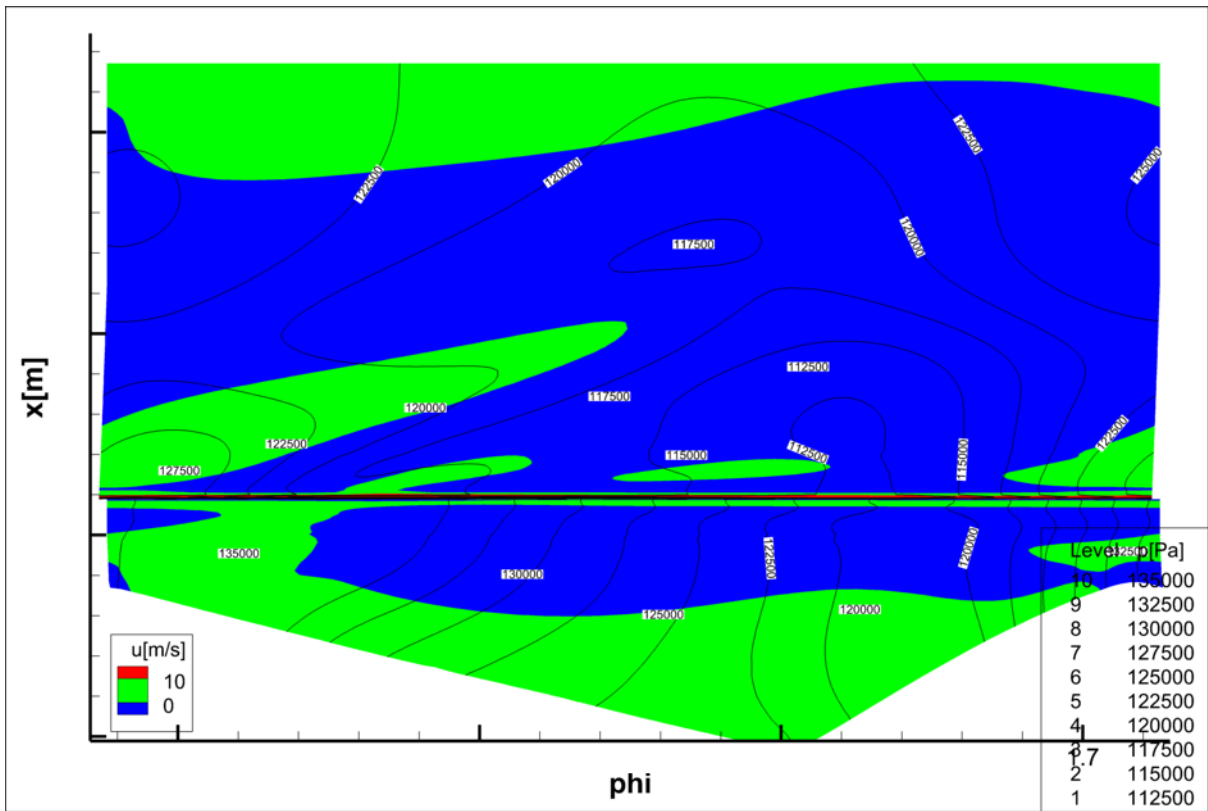


Figure: A.8: Recirculation bubble for the 1.3 mm forward facing step with pressure lines

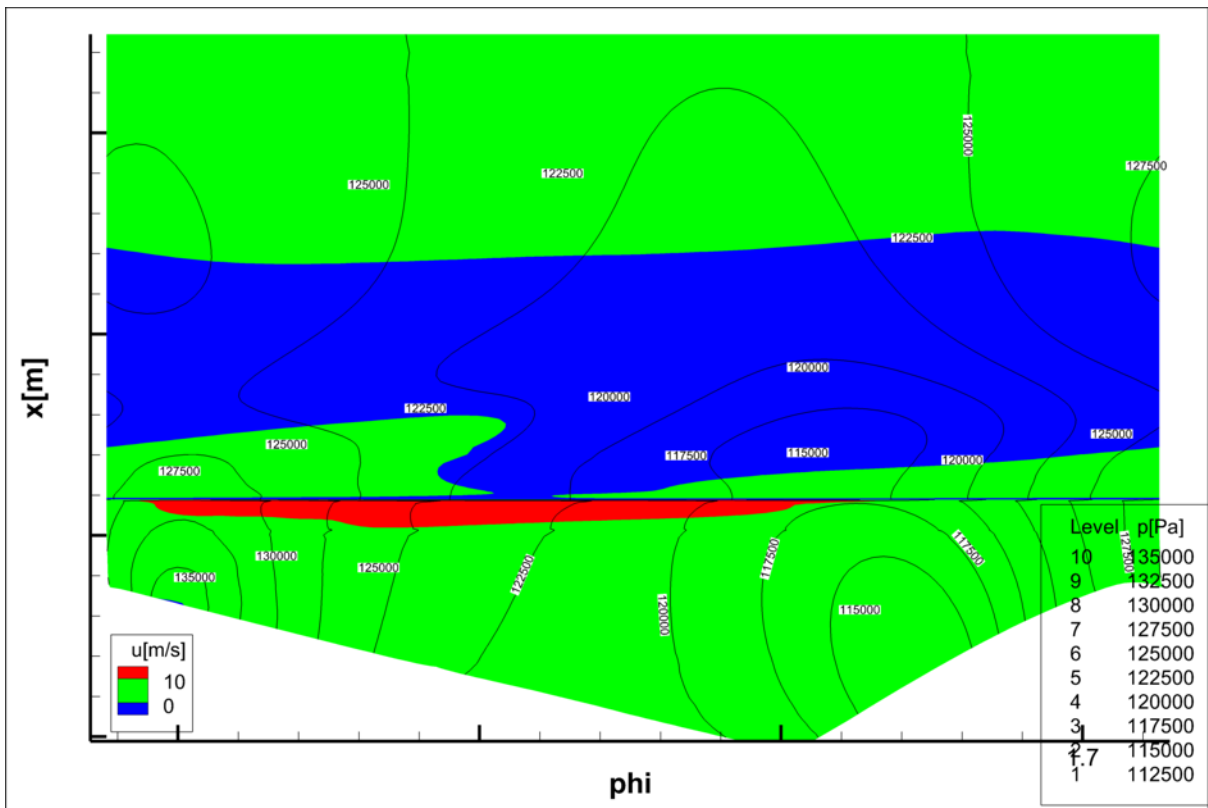


Figure: A.9: Recirculation bubble for the 1.3 mm backward facing step with pressure lines

12. Works Cited

- [1] W. Sanz, "*Computational Fluid Dynamics*," Graz University of Technology, 2016.
- [2] H. Oertel, "*Prandtl-Führer durch die Strömungslehre Grundlagen und Phänomene*," Karlsruhe: Springer, 2012.
- [3] J. H. Ferziger, "*M. Peric and Ferziger, Computational Methods for Fluid Dynamics*," Heidelberg: Springer, 1999.
- [4] W. Sanz and C. Hochenauer, "*Numerische Verfahren in der Energietechnik*," Graz University of Technology, 2017.
- [5] S. Lecheler, "*Numerische Strömungsberechnung*," München: Springer, 2014.
- [6] "<https://www.sharcnet.ca/>" 10 5 2019. [Online]. Available: https://www.sharcnet.ca/Software/Ansys/17.0/en-us/help/wb_msh/msh_skewness.html. [Accessed 10 05 2019].
- [7] L. Langston, "*Secondary Flows in Axial Turbines - A Review*," Storrs, 2006.
- [8] O. Sharma and T. Butler, "Predictions of Endwall Losses and Secondary Flows in Axial Flow Turbine Cascades," *Journal of Turbomachinery*, vol. 109, no. 2, pp. 229-236, 1987.
- [9] W. Neil, K. Harvey and Ramsden, "A Computational study of a Novel Turbine Rotor Partial Shroud," *Journal of Turbomachinery*, pp. 123-126, 2001.
- [10] J. V. Moriniere, "*Wall pressure fluctuations and topology in separated flows over a forward facing step*," Springer, 2006.
- [11] C. Scheit, A. Esmaili and S. Becker, "Direct numerical simulation of flow over a forward-facing step," *international Journal of Heat and Fluid Flow*, p. 10, 2013.
- [12] S. Darmawan, "Backward-facing step geometry for flow analysis a review of non-dimensional parameters," *Jornal of Academic Faculty Development*, pp. 1-11, 2016.
- [13] X. T. Guannan, L. C. Liu, A. Keisuke and N. Taku, "A review of Backward-Facing Step (BFS) flow mechanisms, heat transfer and control," *Thermal Science and Engineering Progress*, vol. 6, pp. 194-216, 2018.
- [14] D. M. Driver and L. H. Seegmiller, "Features of a Reattaching Turbulent Shear Layer in Divergent Channel Flow," *AIAA*, vol. 23, no. 2, pp. 163-171, 1985.
- [15] S. David, "*Numerische Turbulenzuntersuchung an einer Turbinenstufe*," Graz University of Technology, 2017, master thesis.
- [16] S. Bauinger, "*On Aerodynamical and Acoustical Flow Phenomena due to Three-Dimensional Reality Effects*," Graz University of Technology, 2017, PhD thesis.

- [17] M. J. Sherry, D. L. Jacono and J. Sheridan, "Flow separation characterisation of a forward facing step," *Sixth international symposium on turbulence and shear flow phenomena*, 22 june 2009.
